Dissertation

submitted to the

Combined Faculty of Natural Sciences and Mathematics

of the Ruperto Carola University Heidelberg, Germany

for the degree of

Doctor of Natural Sciences

Presented by

M.Sc. Pascal Holzheu

born in: Weimar

Oral examination: 10.02.2020

Computational Modeling of the Vacuolar pH-Homeostasis in *Arabidopsis thaliana*

Zusammenfassung

Das Ziel dieser Arbeit ist die Analyse der vakuolären pH-Homöostase in Wurzelzellen von *Arabidopsis thaliana* mittels rechnerischer Verfahren. Der pH ist ein wichtiger Parameter für eine Reihe zellulärer Prozesse, wie etwa der Kontrolle von Enzymaktivitäten und der Aufrechterhaltung des osmotischen Drucks durch die Schaffung eines Protonengradienten über die vakuoläre Membran hinweg, welcher wiederum für die Homöostase anderer Ionen auf beiden Seiten der Membran verwendet wird. Obwohl viele Prozesse bekannt sind, die wichtig für die Etablierung und Aufrechterhaltung eines sauren vakuolären Lumens sind, haben neuere Experimente zeigen können, dass unser aktuelles Verständnis dieser Prozesse nicht vollständig ist. Um die vakuoläre pH-Homöostase in einer integrativen Weise zu untersuchen, fokussiert sich diese Arbeit auf drei Aspekte.

Im ersten Teil wird eine Übersicht über Ansätze der rechnerischen Systembiologie in *Arabidopsis thaliana* gegeben, um den Stand der Forschung aufzuzeigen und den Rest dieser Arbeit in einen breiteren Kontext zu stellen.

Der zweite Teil konzentriert sich auf Transportreaktionen über Membranen hinweg und auf die Bedeutung der korrekten Skalierung kinetischer Geschwindigkeitsgesetze in mathematischen Modellen mit gewöhnlichen Differenzialgleichungen wie dem, welches im dritten Teil dieser Arbeit beschrieben wird.

Im dritten Teil wird schließlich ein mathematischer Modellierungsansatz verwendet, um experimentelle Daten bezüglich der vakuolären pH-Homöostase zu erklären. Dazu werden drei Hypothesen zu den Mechanismen, die zur vakuolären Ansäuerung beitragen entwickelt: Ein bisher unbekannter direkter Protonenimport, Protonen, die durch Proteindegradation freigesetzt werden und die Umkehr der Richtung eines Protonen-Calcium-Antiporters. Jede dieser Hypothesen wird in einem Model mit gewöhnlichen Differenzialgleichungen implementiert und mittels experimenteller Daten getestet.

Summary

The aim of this work is the analysis of the vacuolar pH homeostasis in *Arabidopsis thaliana* root cells by means of computational modeling. The pH is an important parameter for a range of cellular processes such as the control of enzyme activity and the maintenance of osmotic pressure acting through the establishment of a proton motive force across the vacuolar membrane that in turn is used in the homeostasis of other ions on both sides of the membrane. Although many processes are known to be important for the establishment and maintenance of an acidic vacuolar lumen, recent experimental results have shown that our current understanding of those processes is not complete. To study the vacuolar pH homeostasis in an integrative manner, this work focuses on three different aspects.

In the first part, an overview over computational systems biology approaches in *Arabidopsis thaliana* is given to demonstrate the state of the art and put the rest of the work in a broader context.

The second part then focuses on transmembrane transport reactions and the importance of the correct scaling of the kinetic rate laws of those reactions in mathematical models employing sets of ordinary differential equations, which is of importance for any multi-compartment model such as the one presented in part three of this thesis.

In the third part, a mathematical modeling approach is subsequently used to explain experimental data concerning the vacuolar pH homeostasis. To do so, three hypotheses of the mechanisms contributing to vacuolar acidification are developed: An as of yet unknown direct proton import, protons released by protein degradation and the reversal of a proton-calcium antiporter. Each of those hypotheses is implemented in an ordinary differential equations model and tested for feasibility against the experimental data.

Contents

List of figures

List of tables

Symbols and abbreviations

Abbreviations

ATP Adenosine triphosphate

CAM Crassulacean acid metabolism

COPASI Complex Pathway Simulator

FBA Flux Balance Analysis

FVA Flux Variability Analysis

LSODA Livermore Solver for Ordinary Differential Equations

MCA Metabolic Control Analysis

MVB Multi-vesicular bodies

NFAT Nuclear factor of activated T-cells

NFκB nuclear factor 'kappa-light-chain-enhancer' of activated B-cells

ODE Ordinary differential equation

SBGN Systems Biology Graphical Notation

SBML Systems Biology Markup Language

TCA cycle Tricarboxylic acid cycle

TGF-β Transforming growth factor beta

TGN/EE Trans-golgi network/early endosome

Physical/chemical units

A Ampère

C (= A*s) Coulomb

K Kelvin

L Liter

m Meter

M Molar

s Second

V Volt

Constants

F Faraday's constant; 96 485 000 μC/mmol

R Universal gas constant; 8314.5 μJ/mmol/K

T Temperature, here: standard room temperature T = 293K

z ionic valence, if not specified z = 1

Variables and symbols

[.] Concentration

[.]$_{cyt}$ Concentration in cytosol

[.]$_{nuc}$ Concentration in nucleus

[.]$_{vac}$ Concentration in vacuole

A Area

E Equilibrium potential

J Mass flux

V Volume

I - General introduction

There have been many attempts to define systems biology, most of which include a definition of systems biology's objectives as the integration of several layers of biological knowledge into a bigger picture [1][2][3]. By doing so, systems biology can help us to discover gaps in our knowledge and to understand complex biological systems to a greater extend. A system in this context can be seen as set of entities, between which there is some sort of interaction, in the case of biology this could be the set of animals in an ecosystem with predator-prey interactions, or a set of molecules in a cell that can react with one another. The interactions of the different components of a system can be analyzed in many ways, both experimentally and computationally. In fact, experimentation and computation often go hand in hand, as computational approaches need to be tested against the real world situation and often can only be applied in the first place after experimental knowledge was obtained. The results of computational systems biology on the other hand can be used to guide further experimentation (figure 1). Overall, this repeated cycle of experimental data generation, model building and prediction as well as joint hypothesis development and refinement can lead to a better understanding of complex biological phenomena on all levels. It is also a great example of the power of interdisciplinary research and communication, as only through the collaboration of researchers with different expertises this cycle of knowledge generation will actually be fruitful.
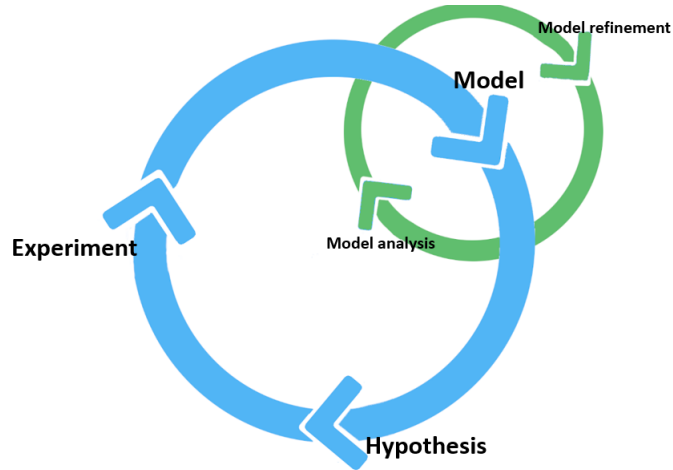
Figure 1: The cycle of knowledge generation in systems biology. Following hypothesis-based experimentation, a model of the system is constructed. Subsequent cycles of model analysis and refinement lead to an improved formulation of the original hypothesis, based on which further experiments are performed. Every round of the cycle will eventually lead to a better understanding of the biological system under investigation.

1.1 Kinetic models in systems biology

In the computational part of systems biology, which this thesis is focused on, a wide range of methods has been established such as network analysis based on graph algorithms [4] or genome scale modeling approaches [5]. One of the most common approaches in the quest to understand complex biological systems is however kinetic modelling [6], in which a set of ordinary differential equations is formulated, each describing the temporal development of the concentration of a molecular species dependent on a set of parameters and the time-dependent concentration of other molecular species. In general, a set of ODEs can be expressed as:

$$\frac{dS_i}{dt} = f(S_i(t), p) \quad , \tag{1}$$

where S_i is the vector of substance concentrations and p a vector of kinetic parameters. To arrive at a specific formulation for an ODE of a given component, one needs to consider all velocities leading to the production or degradation of

the component:

$$\nu = \nu_f - \nu_r \quad , \tag{2}$$

which in the simple case of a reversible mass-action-governed reaction such as

$$S \longleftrightarrow P$$

would read

$$\nu = k_f * S - k_r * P \tag{3}$$

with equilibrium constant

$$K_{eq} = \frac{k_f}{k_r} = \frac{P}{S} \quad . \tag{4}$$

Here, S and P denote the substrate and product concentrations and k_f, k_r the kinetic constants of the forward and reverse reaction. In many cases, more complex terms are used for the formulation of reaction velocities, e.g. describing saturating rate laws as often caused by enzymatic catalysis like Michaelis-Menten or involving inhibitors and activators [7]. For the modeller, there are many decisions to be taken in the construction of the ODE system, such as which molecular species is important for the understanding of the system and which is not and can therefore be omitted in the modelling process. An example for this are the multiple phosphorylation steps of receptors in response to a stimulus. One can include each phospho-state explicitly in the model, which comes at the price of computational cost and subsequently can extend the time needed for model parametrization and analysis steps. On the other hand, one might decide to model only a single phospho-state if one assumes that the dynamics of the overall system is not altered significantly by this simplification. Another point to consider by the modeller is the level of detail of the chemical kinetics expressions for a reaction. Reactions can be assumed to follow simple mass-action kinetics as in the example above, which are straight forward and add only a single kinetic parameter to the system. However, possibly important regulatory interactions or saturation kinetics are not taken into account

in this case. A detailed physico-chemical kinetic expression can on the other hand be taken, usually increasing the number of parameters, many of which are often not exactly known. This in turn can, if no additional simplifications are applied, once again increases the computational cost. Finding a middle ground between computational cost and enough detail to describe the system under investigation sufficiently well is therefore one of the central tasks for the modeller.

The aforementioned parameters of the ODE system can be known from previous studies or measured by experiments. In many cases however, not all parameter values have been determined or are even experimentally accessible, so they must be inferred through other means. The typical procedure to do this is through so called parameter estimation, in which experimentally measured variables (e.g. concentrations of molecular species) of the system under given circumstances are used to infer the most likely values of the parameters. A method to assess a model's performance is the method of least squares, in which the squared distance of some values of the model's output functions and the experimentally measured values is calculated and, through numerical procedures (such as the particle swarm algorithm or a genetic algorithm), minimized [8]. In this process, the ODE system's parameters are successively adjusted by the computer based on a range of possible criteria, until a sufficiently good fit is reached. In some cases, the parameters can be determined well, in other cases, there is a range of equally likely parameter values and value combinations obtained. In this case, one speaks of non-identifiable parameters. If the reason for the non-identifiabilities resides in the structure of the model, in which the value of a parameter depends on the value of a set of other parameters (structural non-identifiability), one can try to simplify the model by explicitly intruducing the dependence [9]. If a lack of experimental data leads to some parameters being non-identifiable, one speaks of practial non-identifiability. In this case, the existing model can be analysed to determine experiments that could help resolving the non-identifiabilities. If one can not avoid non-identifiabilities, a set of similarly likely model parametrizations is obtained and all are subsequently

4

analyzed. The results of the anayses can then be investigated, whether certain common properties are present for all parametrizations or if the values or value combinations of certain parameters determine can be grouped to determine the specific aspects of the model's behavior.

Among the standard model analysis routines are metabolic control analysis (MCA), in which one analyzes how the control of the different enzymes involved in a pathway over the concentrations and fluxes of metabolites is distributed. Furthermore, calculating the sensitivities of a range of variables to changes in parameters can give further insight into the specific effect a given parameter has. In the biological context, this can help to identify for example steps of a pathway that are promising targets for drug interferences.

Overall, systems biology has often been described as an iterative cycle of experimentation, modeling and prediction, as shown in figure 1. Throughout this cycle, one hopes to arrive at a successively better understanding of the system under investigation. In the following chapters, I will provide a more in depth look at computational approaches in systems biology and how they have been applied to problems in *A. thaliana* biology (chapter II), and describe specific challenges and their overcoming of kinetic modeling when multiple compartments are involved (chapter III). Finally, a kinetic modeling approach to a concrete problem in *A. thaliana* cell biology concerning the vacuolar pH homeostasis will be presented (chapter IV).

I - Computational systems biology of Arabidopsis thaliana

2.1 Introduction

By the submission of this thesis, the following chapter has been accepted for publication in the journal of Cellular and Molecular Life Sciences (CMLS) as a review under the same title. The review has been written by myself with the support of Ursula Kummer and has been modified slightly for this thesis. Systems biology is a field employing both quantitative experimental techniques such as quantitative time-course measurements of molecular species, high-throughput techniques like mass-spectrometry based proteomics, high-throughput RNA-sequencing or live cell imaging [10] as well as a variety of computaional modeling approaches. The data resulting from the experiments are analysed and used to build, validate and test the computational models with the goal of elucidating the properties of the respective biological systems. These techniques form an iterative cycle, in which experimental results can feed into a mathematical model that can be used to identify the best approaches for further experimentation, which in turn contribute to the refinement of the model, leading successively to a better understanding of the system under investigation [11]. Multiple systems biology studies have been published with respect to human cells or tissues, as well for animal model or microbial systems. Plant systems have been very underrepresented in this community for many years. This is largely due to the fact that experiments like live cell imaging and the measurement of intracellular components is harder to achieve than with other organisms. Also, the plant biologist community in general is much smaller than e.g. the biomedical community [12]. However, the model organism *Arabidopsis thaliana*, for which a wide variety of information on its genome, proteome and many of its biochemical pathways has been published, has been

more of a target for computational systems biology. Therefore, especially over the last decade, the number of systems biology studies on *Arabidopsis thaliana* has steadily increased [13][14].

A. thaliana has been described as a valuable experimental system for genetic analyses as early as 1943 by Laibach *et al.* [15] due to the unchanged number of heterochromatic bodies seen in both inter- and metaphase, which had rarely been observed in plants at that time. Following multiple fundamental studies [16][17][18], the first international symposium for the plant was held in 1965, organized by Gerhard Röbbelen. After it had been shown that *A. thaliana*'s genome is comparatively small with few repetitive elements by Pruitt *et al.* [19], the employment of the plant as a model organism gained traction, leading to the sequencing of its entire genome between the years 1990 and 2000 by an international consortium [20], in parallel to the human genome project [21], thus becoming the first plant to have its whole genome sequenced. In the years since then, our understanding of a multitude of aspects of *A. thaliana*'s biology has been deepened by many studies and it has finally also become a target of systems biology approaches. Some of these studies employing two of the major computational modeling approaches, genome scale models and kinetic models using ordinary differential equations, will be reviewed in the following.

Not included in this chapter are, to mention two major classes, stochastic modeling and partial differential equation (PDE) based models. Stochastic modeling approaches are employed especially in situations, where low total numbers of molecules can lead to significant stochastic effects. Specifically gene regulatory networks are frequently modeled using this approach in other organisms. So far, stochastic modeling has only very sparsely been used in plant cell biology. Partial differential equation based models that describe the development of a molecular species not only over time like ODE-based modeling, but also have a spatial component have also been omitted in this chapter, as compared to ODEs, PDEs have only sparsely been applied in general as their computa-

tional complexity is higher and analysis techniques for them are comparably sparse. In plants, PDE usage is mostly limited to cell-fate and morphological studies, describing processes on a higher scale than the processes I focus on here.

2.2 Kinetic models

Kinetic models employing ordinary differential equations (ODEs) are the class of models most widely used to describe cellular processes like metabolic and signalling pathways [22]. In these models, the change over time of the concentration of a molecular species is described by a sum of reaction velocities for each reaction the species takes part in. The reaction velocity is determined by the kinetic rate law governing the respective reaction, including a set of kinetic parameters, some of which are known or can be measured directly, others have to be inferred. To estimate the values of as yet unknown parameters, the resulting system of ODEs can subsequently be fitted to experimental data [23]. Not every time, all parameters can be identified unambiguously in this manner, leading to a set of model parametrizations that can be compared to one another, enabling researchers to determine common properties of all parametrizations or parameter-specific differences.

In only extremely simple cases, an analytical solution to the set of ODEs can be calculated leading to time-courses of all modeled molecular species. However, in most cases typically occuring in systems biology, an analytical solution can not be found, requiring a simulation of the time-courses by means of numerical integration. Further analyses of the model such as steady-state analysis can determine the concentration levels the system stably approaches over time, while bifurcation analysis explores the stability of a steady-state and the occurance of oscillations of a molecule's concentration [24]. Other techniques such as metabolic control analysis (MCA) [25] are employed to gain an understanding of the system beyond the directly observable and experimentally

accessible facts, such as the control certain reactions have over a target function and to predict the responses to system perturbations. A good model is able to reproduce the experimentally observed data, predict system responses to perturbations and experimental results not used for fitting as well as provide insights into system structures and properties one could not have achieved otherwise.

2.2.1 Kinetic models of metabolic pathways

The photosynthetic carbon reduction cycle (Calvin-cycle), in which CO2 gets incorporated into carbohydrates by using the energy harvested during photosynthesis, was among the first pathways in plants for which metabolic kinetic modeling was applied [26]. Being the defining features of photoautotrophs, most current efforts in kinetic modelling of the metabolism in *A. thaliana* are still focused on the various aspects of photosynthesis and photorespiration, together with their associated pathway of carbon fixation [27]. In a study by Matuszynska *et al.* [28] in 2016, an ODE model of non-photochemical quenching was employed to demonstrate that both the accumulation of the accessory pigment zeaxanthin and the protonation of the photosynthetic antenna complex are responsible for providing the plant with a short-term light memory, through which damage by light overexposion can be avoided.

Using the energy gained through the light reactions of photosynthesis, the Calvin-cycle's first reaction is governed by RuBisCO, which attaches CO2 to a five-carbon acceptor molecule to form two three-carbon products. Through multiple further steps, larger carbohydrates such as the eventual storage compound starch and the transportable sucrose are formed. To explore the regulatory principles behind the degradation and re-synthesis of starch, a model of the cycling of sucrose through glucose and sugar phosphates in leaf cells by Henkel *et al.* [29] was constructed. Fitting the model to experimental data, the resulting parameters were analysed using principle component analysis, with which further experiments could be suggested to increase the identifiabilies of

a set of parameters. As a result of their modeling efforts, it could be suggested that the enzyme hexokinase bears most of the control over the flux, with sucrose degradation by invertases only contributing to a minor extend.

Besides carbon, oxygen and hydrogen, several other elements are necessary for the plant's survival. Among them is sulfur, a crucial component of the amino acids cystine, cyteine and methionine as well as of vitamins and coenzymes such as biotin and panthotetic acid [30]. A chronic lack of surfur generally leads to a yellowing of leaves, and later inevitably to the death of the plant [31]. It is therefore clear, that the assimilation of sulfur from the environment is an important task for any plant. Despite a rich knowledge about the sulfur assimilation pathway, a conclusive picture of the rate-limiting steps has not been constructed until recently. In a study by Feldman-Salit *et al.*, an ODE model was constructed to tackle that problem in 2019 [32]. After fitting their model to published data and creating a model ensemble to account for parameter uncertainties, the group used MCA to show that the control over the sulfur assimilation pathway was dynamically distributed, depending on environmental conditions, where under sulfur starvation, adenosine-5'-phosphosulfate reductase carries most of the control. Under standard lab conditions, control is shared with sulfite reductase.

Another nutrient, iron, plays an important function especially in redox reaction governing enzymes, such as cytochromes. Under iron starvation conditions, many eudicots such as *A. thaliana* acidify their roots' environment, increase iron reductase activity and iron transport across their root membranes [33]. A model describing the regulatory interactions of iron-deficiency associated genes and their transcriptional response induced by iron starvation was created by Koryachko *et al.* [34]. Fitting the model to the results of gene expression measurements and mRNA decay rate, they subsequently balanced the model's complexity with the available data. With the help of their model, the team was able to correctly predict the protein expression changes resulting from double mutants of iron deficiency response regulator genes, as well as account for a significant difference in mRNA decay rates between low and high iron supply

conditions.

An interesting example of kinetic modeling of metabolic pathways is provided by Nägele *et al.* [35], demonstrating the power of such models to explain strain-to-strain differences. They contructed a kinetic model of the central carbon metabolism in *A. thaliana*, fitting it to experimentally obtained, subcellular compartment-specific concentration values of carbohydrates and enzymatic rates. Using their model, the group could show that increases in both vacuolar and cytosolic sucrose levels are responsible for a higher cold tolerance in certain *Arabidopsis* accessions found in northern climates.

Besides the primary energy metabolism, metabolism of the various secondary plant compounds became a promising target for modeling approaches. The diversity of plant secondary compounds is unparalleled in other organisms, with a number of 200,000 different chemical species being estimated to exist, all with their unique pathways and functions [36]. Many of these compunds have been proven to be useful for both agricultural and medicinal uses [37][38]. With a better understanding of their pathways, biotechnological modifications can be designed to increase the production of these compounds by the plant and help us utilize them more efficiently.

An example for kinetic modeling in secondary compund metabolism is provided by Knoke *et al.* [39]. The group looked into the metabolism of aliphatic glucosinolates, a class of major defense compound of *A. thaliana* derived from methionine. The chain length of those compounds are determined by three isoforms of multifunctional enzymes, methylthioalkymalate synthases (MAM). To understand the specific role of each in the determination of glucosinolate chain lengths, they measured much of the data on the pathway's enzyme kinetics from wildtype strains or strains deficient in one of the isoforms. The experimentally indeterminable parameters of their ODE model of the pathway were fitted to data on glucosinolate chain lengths in those strains. Simulation of the model provided insight into the differential roles of two multifunctional enzymes of the pathway, MAM1 and MAM3, which can hardly be separated

experimentally, showing that an elevated expression of MAM3 is necessary in MAM1 knockout lines to produce the observed glucosinolate profile.

By using large amounts of experimental data on flavonoid profiles and RNA levels, Olsen *et al.* constructed and fitted a kinetic model of the *Arabidopsis* flavonoid pathway, which is known to be differentially regulated by several environmental stressors. Formulating an explicit temperature dependence of kinetic constants by scaling them exponentially to the temperature using the Arrhenius equation, the team's ODE model predicts the last steps of the pathway to be especially sensitive to temperature to account for the experimentally determined flavonoid concentrations under different nitrogen supply and temperature regimes [40].

Kinetic models of metabolism		
Focus	Main findings	Reference
Non-photochemical quenching	A short term light memory is provided by zeaxanthin and protonation of antenna complex	Matuszynska *et al.* (2016)[28]
Sucrose metabolism	Hexokinase excerts most control over sucrose cycling flux	Henkel *et al.* (2011)[29]
Sulfur assimilation	Control over the pathway is dynamically distributed, based on sulfur availability	Feldman-Salit *et al.* (2019)[32]
Iron metabolism	Iron defficiency response regulator gene mRNAs exhibit different decay rates under low and high iron supply conditions	Koryachko *et al.* (2019)[34]
Central carbon metabolism	Intracellular sucrose concentrations are responsible for strain-to-strain differences in cold acclimatisation	Nägele *et al.* (2013)[35]
Aliphatic glucosinolates metabolism	Differential role of MAM1 and MAM3 in glucosinolate chain length determination	Knoke *et al.* (2009)[39]
Flavonoid pathway	Last steps of the pathway are especially sensitive to temperature	Olsen *et al.* (2009)[40]

Table 1: Overview over the kinetic models of metabolism discussed in the text, showing the main focus as well as a selection of main conclusions drawn from each model.

2.2.2 Kinetic models of signalling pathways

Signalling events play a central role in most processes in the plant, from embryogenesis to responses to both biotic and abiotic stressors. Among the best studied long-distance signalling molecules in plants are plant hormones such as auxins and cytokinins that, upon binding to cellular receptors, can trigger signalling cascades leading, for example, to altered gene expression [41]. Similar to kinetic models of metabolism, ODEs are used in most of the computational modeling studies of signalling pathways. While mass-flow is the subject of interest in metabolism, signalling is concerned with information flow. The basic approaches of kinetic model construction are the same for metabolic and signalling pathways, but since many signalling pathways share structures such as the transfer of information from the extracellular space to the inside of the cell and the nucleus as well as frequent covalent modifications of pathway compounds, a separate discussion of these models seems appropriate [42].

Cytokinin and auxin are known to be, amongst other functions, the key hormones in root development and control of lateral root formation in *A. thaliana* [43]. Their signalling pathways are branched and intertwined with one another [44], where for example the local accumulation of auxin leads to the initialization of lateral root primordia and promotes cell division, whereas cytokinin's action is opposed to that by promoting differentiation. Here, kinetic modeling can provide help in elucidating their specific function and the relevant interactions. Such is the case in a study by Muraro *et al.* [45], who investigated the role of SHY2, a protein responsible for the balancing of auxin's and cytokinin's role in meristem size determination as well as the response of auxin response genes on cytokinin's presence. Modeling the concentration changes of 25 metabolites of the pathways and with the help of bifurcation analysis, it was shown that the interaction between the two hormone induced pathways can cause periodic root branching and can lead to tissue-specific oscillatory gene expression.

14

Auxin also plays a role in pattern formation during shoot development. By employing an ODE based modeling approach in which the transcriptional output was modeled as a function of the combination of the concentration of auxin and its perception by the cell, Vernoux *et al.* could predict spacial differences in auxin sensitivities being one of the determining factors in shoot apex patterning [46]. One of the underlying causes for this was predicted to be the differential expression of auxin response factors (ARFs), transcription factors acting in auxin signalling, in different regions of the plant as well as the ability of a cell to buffer the pathway's response based on the ratio of ARF activators to repressors. The model's predictions were subsequently verified in experiments, where the group could show that a reporter gene was inhibited differentially by auxin in different meristematic zones.

Due to their sessile and photoautotrophic nature, plants are heavily influenced by circadian rythms. A founding factor in the establishment of a circadian response system in *Arabidopsis* is the transcriptional regulator TOC1. An interaction of TOC1 signalling with the plant hormone abscisic acid (ABA) is known during abiotic stress, though the exact dynamics of these circuits are not well understood. Pokhilko *et al.* were able to construct a model of the TOC1 pathway, exploring its connection with the signalling pathway induced by abscisic acid. With their model, they could describe the experimentally observed molecular profile and timing events of the clock [47], in which an increase of ABA leads to a lengthened free-running period of the circadian clock. Furthermore, including ABA regulated stomatal closure in the model, the influence of TOC1 on its closure and opening could be inferred. By doing so, a better insight could be gained of the control TOC1 has as an environmental sensor over the circadian processes in the plant.

Kinetic models of signalling pathways		
Focus	Main findings	Reference
Cytokinin and auxin crosstalk	Interaction of auxin and cytokinin pathways can lead to tissue specific oscillatory gene expression	Muraro *et al.* (2011)[45]
Auxin signalling	Shoot apex patterning is produced by differential auxin inhibition of downstream genes in different meristematic zones	Vernoux *et al.* (2011)[46]
Circadian clock	TOC1 as a environmental sensor for circadian processes	Pokhilko *et al.* (2013)[47]

Table 2: Overview over the kinetic models of signalling pathways discussed in the text, showing the main focus as well as a selection of main conclusions drawn from each model.

2.3 Genome scale metabolic models

Genome scale metabolic models, which model mass-flow through an organism's reactions based on genome annotations, have been generated for a variety of organisms and cell types in the past few years. They can be constructed in the absence of detailed information on the kinetic mechanisms of the biochemical reactions involved in the mass-flow. In these models, the stoichiometric matrix which contains the stoichiometry with respect to metabolites for each of the reaction in a metabolic network is used to compute potential flux distributions [48]. The stoichiometric information is established by the annotation of the genome of a sequenced organism. The annotation allows to derive a draft stoichiometric model of the metabolism by linking known genes to protein functions, in this case enzymatic activities. Analysing if this draft stoichiometic model allows the system to run into a steady state and produce e.g. biomass,

can be used to identify and fill in gaps. This gap filling process already comes with knowledge gain since often previously not annotated functions can be found due to the need for the system to be able to carry out the respective activity [49].

Using additional contrains, e.g. experimentally determined fluxes and directionalities of reactions, an optimality criterion is defined. This is often the maximization of biomass. Subsequently, using so-called flux balance analysis (FBA) optimal (with respect to the chosen criterion) flux distributions can be computed. Additional analyses like flux variability analysis (FVA) allow to estimate uncertainties in these fluxes [50].

By now, *A. thaliana* is the plant organism for which most of the genome scale metabolic reconstructions have been done. The first ones to do so were Poolman *et al.* in 2009, who constructed a model containing 1,253 metaboilites and 1,406 reactions. By removing metabolites involved in only one reaction and the respective reaction as such, they could reduce the model significantly to 855 reactions. They showed, among other findings, that their model can describe the production of the main biomass components in experimentally observed proportions and that a realistic ATP demand can be inferred. Comparing this model to genome scale metabolic reconstructions of other organisms, they found that a similar percentage of all available reactions, namely around 15%, were needed to achieve the production of those main biomass components [51]. In a similar effort, Dal'Molin *et al.* created AraGEM, a comprehensive literature-based whole genome reconstruction, which is comprised of 1,748 metabolites, 1,567 unique reactions and 5,253 gene-enzyme reaction-association entries. In addition to the production of biomass as done in the Poolman model, AraGEM considers the localization of reactions in organelles and it also includes autotrophic metabolism, a central feature of plants. The classical photorespiratory cycle could be well predicted using this model, as well as the specific redox metabolism in both photosysnthetic and non-photosynthetic plant cells. Interestingly, the model predicted 75 reactions necessary for primary metabolism for

which genes have not yet been identified, an example of the predictive potential of genome scale models. [52].

Models such as these can be used in further studies to analyze the global effects of gene knock-outs or changes in gene expression. For example, Williams *et al.* [53] used a genome scale metabolic model, building on the one by Poolman, to predict the fluxes through different pathways of *A. thaliana*'s central carbon metabolism, as well as the alteration of the flux distribution by temperature and hyperosmotic stress which they showed could alter both biomass distribution, glucose consumption rate and gene expression patterns. By using steady-state metabolic flux analysis, an experimental method measuring the redistribution of stable isotopes such as the carbon isotope ^{13}C, the group were able to estimate the flux distribution in *Arabidopsis* not only under standard conditions, but also under stress conditions. Comparing the experimentally determined fluxes with the fluxes predicted by the accordingly constrained genome scale model, they showed that the model accurately could predict the shift from the flux through phosphoenolpyruvat carboxylase towards TCA cycle under increased temperature and hyperosmotic stress conditions, providing an example of a fruitful integration of experimental and computational systems biology.

Plant metabolism is tightly coupled with the availability of light energy, where storage compounds are synthesized during the day and became available for further use during the night. To take into account the circadian rhythm also in a genome scale model for *A. thaliana*, Cheung *et al.* constructed a model of leaf metabolism, taking sucrose and several amino acids as output [54]. The team achieved the incorporation of the day/night-cycle by simultaneous simulation of the specific metabolic fluxes occuring during the day, with photon influx enabled, and the zero photon-flux night in a single optimization problem. Constraints to the optimization problem were taken from literature, describing ratios of sucrose to amino acids export and nitrate import, as well as carbon conversion efficiencies. Using FBA, the team could show that by inclusion of the circadian rhythm, the pattern of fluxes during the day observed experimentally could be described better than without its inclusion. This also enabled

them to compare C_3 with CAM metabolism. They found no likely energetic benefits of CAM over C_3 metabolism.

Expanding on the model by Cheung *et al.*, Shaw *et al.* constructed a large-scale genome scale model consisting of 10,664 metabolites and 11,320 reactions, where each original reaction was duplicated to represent separate modules for leaf and root to investigate the partitioning of resources within root and leaf cells [55]. The authors especially focused on nitrogen metabolism in the plant, using a modified version of FBA, dynamic FBA (dFBA), which allows changes of flux distributions over time to be modeled [56]. With this, the effects of environmental perturbations could be closely investigated, for example by assuming a sudden biomass loss, simulating herbivory. The team showed that the subsequent biomass recovery was significantly slowed under low nitrogen conditions, as most bioassimilates were utilized for root growth. This result suggests an adaptation of plants to grow roots for more effective nitrogen assimilation under low nitrogen conditions.

An example for the usage of genome scale models in metabolic engineering is the tissue-specific model by Mintz-Oron *et al.* [57], with the help of which genetic manipulations increasing the production of specific metabolic compounds could be designed. In the course of their study, they developed a modeling pipeline which allows for semi-automatic construction of genome scale models with the inclusion of high-throughput data, capable of processing a variety of data sources. Using this pipeline, tissue-specific protein expression data was used to search for a minimal reaction set necessary to reproduce the tissue-specific core proteome, creating a range of metabolic models for different *Arabidopsis* tissues exhibiting tissue-specific metabolic profiles. The value of their approach was demonstrated by their ability to design genetic manipulations to increase the production of vitamin E.

Genome scale models		
Focus	Main findings	Reference
Central carbon metabolism	Realistic ATP consumption can be inferred	Poolman *et al.* (2009)[51]
Central carbon metabolism	Photorespiration cycle and redox metabolism can correctly be deduced	Dal'Molin *et al.* (2010)[52]
Central carbon metabolism	Stress shifts flux from phosphoenolpyruvat carboxylase to TCA cycle	Williams *et al.* (2010)[53]
Central carbon metabolism during circadian rhythm	CAM not likely to yield energetic benefits over C_3 metabolism	Cheung *et al.* (2014)[54]
Organ specific resource partitioning during circadian rhythm	Low nitrogen shifts biomass production from leaf to root	Shaw *et al.* (2018)[55]
Secondary compound production	Genetic manipulations could be designed to increase vitamin E production	Mintz-Oron *et al.* (2012)[57]

Table 3: Overview over the genome scale models discussed in the text, showing the main focus as well as a selection of main conclusions drawn from each model.

2.4 Concluding remarks and perspective

A. thaliana, a model for higher plants, is a suitable organism for a multitude of computational modeling approaches, as its genome got completely sequenced and a wealth of experimental data has been generated over the decades it has been used in molecular biology. Especially during the past decade, a steadily increasing number of systems biological models have been created for the plant, addressing a variety of questions from photosynthesis and central carbon metabolism to signalling pathways in circadian rythms and secondary plant compound production.

Kinetic models, as opposed to genome scale models, necessitate the availability of detailed kinetic information of single reactions to construct a set of ordinary differential equations for the concentrations of the involved molecular species. These models are then employed for both metabolism and signalling to understand aspects of single pathways, smaller metabolic networks, or how the cross-talk between different pathways shapes the overall output. ODE models dealing with the metabolism of *A. thaliana* cover a wide range of processes, from energy and carbon metabolism to the metabolism of a variety of secondary plant compounds, providing knowledge to be exploited for agricultural and medical purposes. In addition, the understanding of plant development and its hormonal control is significantly furthered by kinetic modeling, as one can dissect single components of an otherwise heavily intertwined signalling pathway in silico.

Genome scale metabolic models, consisting of stoichiometric information about a usually large amount of reactions and their associated metabolites based on genome annotations, have been constructed to model mass-flow through the plant. They have proven to be useful in understanding the global metabolic network of the plant, with the help of typical analysis methods such as flux balance analysis. By constantly extending and improving existing models as well as by developing new methods both to collect experimental data and to incorporate features such as tissue specificity, this modeling approach is able

provide more insight into various aspects of the plant's metabolism.

Other modeling techniques such as partial differential equations based modeling can benefit from the development of a wider set of analysis methods as well as an increase in computational power, rendering this approach fruitful for a bigger variety of problems in plant biology, as the usually big cells, multiple, often intricately shaped cellular compartments can require spatial aspects to be taken into account.

Systems biology, a discipline integrating experiments, theory and computation, applied to questions in plant research has already lead to significant insights, as the exemplary studies provided in this chapter have demonstrated. There is no doubt that with a further development of experimental and computational techniques, it will continue to enhance our understanding of plant biology on all levels.

III - Area scaling in kinetic models of biological systems

3.1 Introduction

This chapter is part of a work done in collaboration with Ruth Großeholz from the group of Ursula Kummer, Bioquant, Heidelberg University. Here, I will present a part of this work with some additional explanations and examples. The structure of the text corresponds to a manuscript that, by the date of the submission of this thesis, has been submitted for publication under the title "Impact of explicit area scaling on kinetic models involving multiple compartments". Subchapter 3.3.2b has been directly taken from that manuscript.

An important feature of plant cells, as it is for all eukaryotic cells, is the spatial separation of the various biochemical processes into distinct compartments, such as the ER, the nucleus and the vacuole. By doing so, several cellular parameters such as the oxidative state or the pH can be held seperate and optimized for the respective processes occuring inside one compartment. In plants, vacuoles are responsible for creating the cell's turgor pressure by accumulating ions, which in turn attract water into the cell. Moreover, compartmental membranes can act as scaffolds for other proteins and harbour transporters that facilitate the communication between exterior and interior, as well as they enable a charge separation by selectively transporting ions between both sides. This charge separation can then in turn be utilized for the accumulation of molecules in an organelle. Being of such a central importance for eukaryotes, a better understanding of the tranport processes on all levels is in the interest of researchers in the biological sciences.

As I could lay out in the first two chapters of this work, computational modeling using ordinary differential equations (ODEs) is a tool that has frequently

been used to describe biochemical systems and their dynamical properties [58]. While a good kinetic model has the power to explain and predict many properties of a dynamical system, some existing knowledge of the underlying processes is also required, such as molecular players involved, reaction mechanisms and kinetic parameters. While some parameter values are known from previous studies, others have to be inferred through fitting of the model's parameters to experimental data. To enable modelers to easily exchange and store their models depite the multitude of modeling tools, the Systems Biology Markup Language (SBML) format was developed [59] allowing for the handling and analysis of computational models with different software and platforms. This format is especially suitable, but not restricted to ODEs.

As introduced in chapter I, ODEs express the time derivatives of the change of the concentration of a substance as a function of it's own and other species' concentration and some kinetic parameters. Those enter some expressions for the reaction velocities that determine eventually the production/consumption speed of a molecular species. As expressed in equation (3), A simple reversible mass-action reaction of one substrate S and one product P and their respective forward and backward mass action rate constants k_f and k_r would lead to a formulation of the reaction velocity as

$$\nu = V * (k_f * S - k_r * P)$$

if S, P are given as concentrations of substrate and product, respectively, and V being the volume of the reaction space. Here, ν represents the reaction rate in mol s^{-1}

When considering more than one compartment in kinetic models, those rules do not hold anymore, as the concentrations of the reactants are explicitly contained within the expression for the reaction velocity. That means that if two compartments with different volumes V_1 and V_2 harbour the substrate S and product P, respectively, a decrease of S does not lead to an equally big increase of P. For example, in a 1-to-1 reaction, a 10^{-3}M concentration of S in a 10^{-9}L

compartment means a total of 10^{-12} moles of substrate, and a 10^{-3}M concentration of P in a 10^{-10}L compartment means a total of 10^{-13} moles of product. If now the substrate concentration decreases by 50%, i.e. $0.5*10^{-12}$ moles, the product also increases by $0.5 * 10^{-12}$ moles, meaning a change of $0.5 * 10^{-12}$ moles per 10^{-10}L, equalling a change of the concentration of $0.5*10^{-2}$M. This is not a 50% increase of P, but a 500% increase.

So to account for this, many modelers chose to scale trans-membrane reactions with the volume ratio of the respective compartments. SBML requires another approach, using particle numbers instead of concentrations. That means that the transport reaction rates describe particle fluxes instead of changes in concentrations, through which the above mentioned problems were thought to be avoided. However, also in this case problems could arise if one simply multiplies the reaction rates with the respective volumes of the compartments in which the respective substances reside in, which is done by some software in the field, calculating the particle flux ν as

$$\nu = V_1 * k_f * \frac{nS}{V_1} - V_2 * k_r * \frac{nP}{V_2} \qquad (5)$$

nS, nP being the molar amounts of S and P. However, that means a direct dependence of the rate of a trans-membrane transport process on the volumes of the involved compartments. This is not conceivable, as on the molecular level, a reaction rate can not directly depend on the anticipated volume of the compartment the product resides in. Biologically accurate is the scaling of the transport rate with the number of transporters in the membrane, or in the case of diffusion of lipophilic substances through the membrane, simply with the area of the membrane. That means, to correctly scale the reaction rates, one should take into account the number of transporters in the membrane, which could, in the case of a constant density of transporters, be simplified to the surface area of the membrane. Instead of adjusting the transport reaction rates by scaling with volumes when dealing with changing compartment sizes,

the consideration of surface area changes is advised:

$$\nu = A * (k_f * S - k_r * P) \qquad (6)$$

As will be discussed below, the change of the interface area between two compartments might simply be linearly dependent on the volume changes, as shown in the example below. Volume and surface area could however also exhibit highly non-linear or even a constant relationship, depending on the concrete architecture of the respective compartments. In the case of the plant vacuole for example, which can be idealized as a spheroidal compartment, the volume would read $\frac{4}{3}\pi * r^3$, with the surface reading $4\pi * r^2$. One can see that the difference between the two scaling approaches scales with $\frac{1}{3}$r, i.e. linearly with the radius of the spheroidal compartment. There are many other cases however, where a linear relationship can not simply be assumed, such as the highly folded inner membrane of a mitochondrium, where the surface area can change without a significant change of the volume.

For gaining an understanding about how exactly an output function is affected by the scaling, it can be useful to calculate the sensitivities of the model output regarding the rate of the transport reaction affected by the different scaling formalism, e.g. to see whether these reaction rates are heavily influencing the behavior of the total system and thus it is crucial to calculate those with more care.

In the course of scaling correctly with the active area one can arrive at unusual units of the kinetic parameters, as in this case $m * s^{-1}$ for k_f and k_r, neccessitating the careful assessesment of the meaning of the affected parameters.

The aforementioned problems are not yet handled in the way suggested above in every case, which can lead to confusing or incorrect analyses of modelled systems in some cases. Therefore, I present here a part of the investigation into the implications of not taking into account the surface area at which a transport reaction proceeds. To that goal, I first introduce a simplified toy model to demonstrate the concept. Afterwards, I present exemplarily two published

multi-compartment models without area scaling. I then compare their behavior in diverse physiological circumstances, where volume ratios or the area to volume ratio change. With this I will demonstrate that the correct behavior can be obtained with any modeling approach as long as the parameters are adjusted when dealing with altered cellular/compartmental geometries.

3.2 Methods

The models were selected using the EBI BioModels database [60]. By the time of the submission of this thesis, 825 manually curated models were available on the website. Out of these, only models with at least two compartments with non-arbitrary volumes were selected. This led to a pool of 21 models, out of which two were selected for further analysis: A model describing the calcineurin-dependent NFAT signalling in T-cells by Fisher *et al.* [61] and a TGF-β signaling model by Zi *et al.* [62].

The selected models were analyzed and modified using the modeling software package COPASI, version 4.23 [63]. The time-courses of the relevant species' concentrations were determined deterministically using LSODA as implemented in COPASI. Scaled sensitivities of steady-state concentrations and transient concentration maxima were calculated using COPASI as well.

3.3 Results

3.3.1 Toy model

To introduce the concept of the effects of area-scaling on different model structures, a simple toy model will be introduced, with the understanding of which other, more complex models from the BioModels database will be more easily analyzed. To this end, a simple model of vacuolar transport of a compound X in a plant cell will be used. Vacuoles in plants can occupy a large portion of the cell, with shapes ranging from almost spherical to highly reticulated and

intricately shaped [64]. For the purpose of this study, I take a single trans-membrane reaction between cytosol and vacuole, formulated with mass action kinetics according to the reaction:

$$X_{\text{cyt}} \longleftrightarrow X_{\text{vac}} \quad ,$$
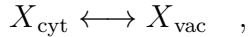
where X_{cyt} and X_{vac} denote the compound X in the cytosol (cyt) and vacuole (vac), respectively. A generic cell and vacuolar size were chosen, with the vacuole comprising 90% of the total volume. The cytosolic volume was assigned a value of $2{,}000\mu m^3$ and the vacuolar volume $18{,}000\mu m^3$. The initial concentration of cytosolic X was chosen to be 1μM, with no initial vacuolar X present, and the transport was chosen to be governed by mass action kinetics with a kinetic rate constant of 0.1.

To demonstrate the different effects of area- vs. volume scaling, two situations were compared: A perfectly spherical vacuole and a reticulated vacuole with, for the sake of this demonstration, twice the surface area of the spherical vacuole and half its original volume. In the spherical version of the vacuole, a volume of $18{,}000\mu m^3$ would mean a surface area of around $3{,}322\mu m^2$. In the hypothetical, reticulated form this would mean a volume of $9{,}000\mu m^3$ and an area of $6{,}644\mu m^2$. Also, in the spherical vacuole version, the kinetic parameter of the area-scaled model is adjusted to deliver the same results. The vacuolar surface was then altered as described above, to compare the resulting time-courses of both versions without further changes of the parameters.

Looking at the time-courses of the reaction in the spherical-vacuole-case, one can see that both volume- and area-scaled versions can reproduce the same behavior (figure 2B). However, when the surface of the vacuole is doubled and the volume of the vacuole is halved with all the other parameters held constant, the volume-scaled model and the area-scaled model produce a different result: The cytosolic concentration of X in the area-scaled version reaches a steady-state in almoost half the time needed for compared with the volume-scaled model, due to a steeper decrease of cytosolic X in the first 10 seconds. The eventual

steady-state in both versions is the same, as surface areas can not influence the thermodynamic properties of the system, with the equilibrium constant being the same, 1, in all cases (figure 2C).

This example demonstrates the potential of differently scaled models to deliver different results in case of changing cellular and compartmental geometries.
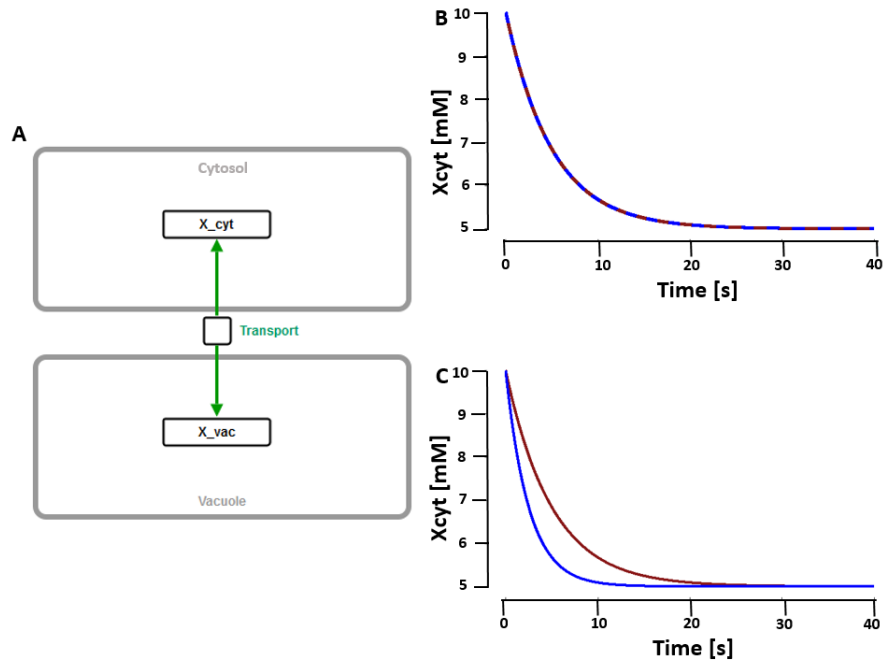
Figure 2: Analysis of the transport of a compound between cytosol and vacuole. A: Model reaction scheme according to the SBGN standard. B: Reproducing the behavior of the original model (red) with the area-scaling model (blue). C: Comparison of the simulations of the volume-scaling model and the area-scaling model under the assumption of doubled vacuolar surface and halved vacuolar volume.

3.3.2 Introducing area-scaling to more complex models

Next, two realistic examples from the BioModels database were analysed. The models were selected as described in the methods section above from the BioModels database. Both the number and size of the compartments included in the models were considered. The vast majority of the models published on BioModels were constructed using only one compartment. Only a small fraction of entries consisted of multi-compartment models with realistic compartment sizes (21 out of 737). Here, I considered the model for cytoplasmo-nuclear shuttling of NFAT in T-cells [61] and a TGF-β model [62].

3.3.2a NFAT signalling in T-cells can be affected by nuclear elongation

The NFAT model by Fisher *et al.* describes the shuttling of dephosphorylated NFAT bound to calcineurin from the cytoplasm into the nucleoplasm and, upon phosphorylation, back into the cytoplasm [61]. NFAT is a transcriptional activator in T-cells, involved in immune and inflammatory responses. The main conclusion drawn from the model was the requirement of higher frequencies of calcium oscillations for NFAT activation compared to NFκB activation. The original model scales all transport reactions with the volume of the compartment the respective molecular species is located in. I changed those reactions to instead scale with the nuclear membrane area, assumed to be spherical. In total, there are seven transport reactions that had to be changed this way (figure 3A). Furthermore, the kinetic parameters of the respective reactions were changed in such a way that the resulting velocities under standard conditions are the same as in the original model by multiplying the original parameter values with the volume of the compartment the molecular species resides in divided by the nuclear membrane area (figure 3B). This leads to the area-scaled model to behave the same way as the original, volume-scaled version of the model.

The model is based on T-cells, which can exhibit an elongated nucleus upon activation [65]. For this study, a constant nuclear and cytoplasmic volume are assumed upon T-cell activation, with different values for the nuclear envelope being investigated. As dephosphorylated, calcineurin bound NFAT is the active transcription factor in this system, the development of its concentration was analyzed as the relevant output function, with which I could compare the effect of the different scaling approaches under the assumption of an elongated nucleus. The volume-scaled model exhibits a slightly slower dynamics and a minimally lower steady state of dephosphorylated, calcineurin-bound NFAT than the area-scaled version when the nuclear surface area is doubled. The difference between the two approaches however are not significant, as those

differences are in the range of 1-2%. This can be explained by looking at the scaled sensitivities of the sensitivites of nuclear NFAT Calcineurin complex (active NFAT) concentration with respect to the different parameters. The kinetic parameters involved in the transport reactions have a rather small impact on active NFAT concentration, therefore a significant effect of their changed value in the case of the area-scaled model is not to be expected, especially when the surface area, entering the kinetic expression linearly, is not changed by large percentages. Hence, a more significant difference in model behavior can be seen with more drastic changes of nuclear surface area, as seen when comparing a one tenth to a ten-fold change of nuclear surface area (figure 3C). This demonstrates that including the area as a scaling factor is not always necessary, especially if the qualitative outcome is more important than the quantitative.

Figure 3: Analysis of the NFAT signaling pathway by Fisher *et al.*. A: Model reaction scheme according to the SBGN standard. B: Reproducing the behavior of the original model (red) with the area-scaling model (blue). C: Comparison of the simulations of the volume-scaling model (red) and the area-scaling model at different nuclear surface values. The blue curves indicate the range of possible outcomes for nuclear areas changed from 10% (lower curve) to 1000% (upper curve) of the original value.

3.3.2b Altered nuclear morphology in cancer cells affects signalling response

I have written this subchapter for the manuscript of "Impact of explicit area scaling on kinetic models involving multiple compartments" as mentioned in the introduction. From there, it has been taken unaltered for this thesis.

The model of Zi *et al.* describes the TGF-β induced Smad2 signaling pathway (figure 4A). The authors constructed the model to investigate the differential effects of variable TGF-β-doses on the intracellular signal dynamics, finding distinct responses of the cell to both sustained and pulsating TGF-β-stimulation. The model reactions include the binding and unbinding of TGF-β to T1R and T2R and their recycling at the plasma membrane, complex formation of R-Smad with Co-Smad and the shuttling of R Smad, Co-Smad and the Smads-complex across the nuclear envelope. Similar to the RanGTP model, the processes of nuclear shuttling were changed from being scaled with the nuclear or cytoplamic volume to being scaled with the nuclear membrane area. The affected parameters were again adjusted to deliver the same output as before. The model was originally constructed using data from HaCaT cells, a human keratinocyte cell line. Skin cancer cells, as many other forms of cancer cells, often exhibit nuclei with irregular shapes as well as being bi- or multinucleated in several cases [66], both facts contributing to a higher surface area to volume ratio, thus posing a potential situation in which the differential behavior of volume- and area-scaled models can be observed.

The possible range of alterations here is large, so for the sake of this study, we analyzed the effect of an increase of both the nuclear and whole cell radius by 50% (figure 4C) and the effect of a 50% increase of the nuclear surface area while keeping all volumes constant (figure 4D). This change affects only the area scaled model as in the volume-scaled version, the nuclear surface is not a parameter considered. Analogously to the example above, the parameters of the area-scaled model were adjusted to replicate the models original behavior

(figure 4B) and we compared the simulations of both the original, volume-scaled model with the area-scaled one (figure 4C and 4D). Furthermore, the scaled sensitivities of the Smads-complex concentrations to the transport reactions were calculated and shown to be sufficiently high, suggesting that a change of the transport rates has a noticable influence on the signalling output. It can be seen that both the steady state value of nuclear Smads-complex and especially its transient are different in both model versions, e.g. the peak concentration of nuclear Smads-complex in the area-scaled model is around 10% lower than in the volume-scaled version when both the cellular and nuclear volumes are increased by 50%, while its peak concentration is around 14% higher when just the nuclear area increased by 50%. Again, the differences are not huge. However, if the models serve a quantitative purpose they are significant enough. This result corroborates that depending on the system under investigation, a careful consideration of the scaling of trans-compartmental rate laws can change the model predictions.
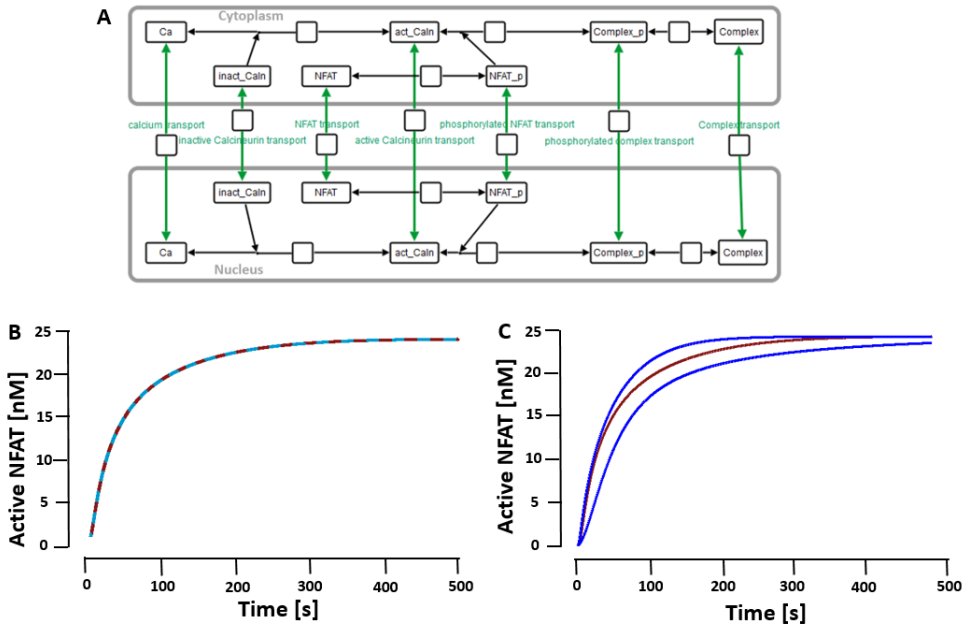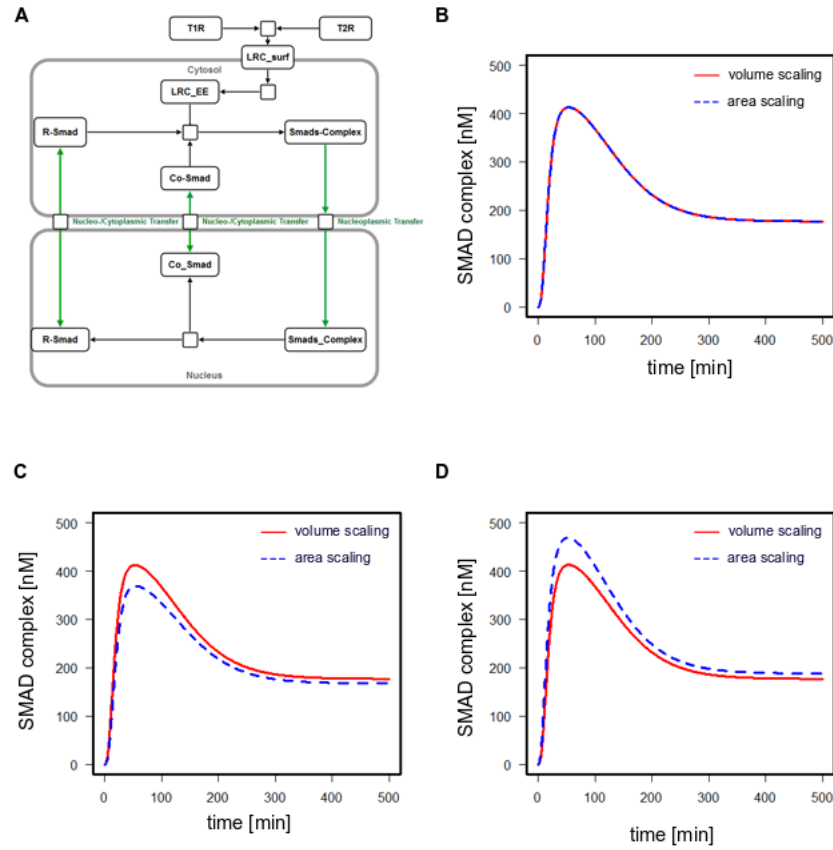
Figure 4: Analysis of the TGF-β induced Smad2 signaling pathway by Zi *et al.*. A: Model reaction scheme according to the SBGN standard. B: Reproducing the behavior of the original model (red) with the area-scaling model (blue). C: Comparison of the simulations of the volume-scaling model and the area-scaling model at both increased cell and nuclear size. D: Comparison of the simulations of the volume-scaling model and the area-scaling model at increased nuclear surface area. Figure taken from the manuscript for "Impact of explicit area scaling on kinetic models involving multiple compartments", Holzheu *et. al*, under revision.

3.4 Discussion

In the continuous search for a better understanding of biological systems, computational approaches such as kinetic modeling have become an important tool, as with a good model, one can analyze systems properties on a different level and even in circumstances, when experimental results are difficult to obtain. A significant part of the modeling process involves the evaluation of assumptions undertaken in the construction of the model, such as which molecular players to include or the level of detail for the kinetic expressions for a reaction. The reaction velocities of enzyme-catalyzed reactions are usually dependent on the amount of enzyme present in the respective compartment, with more enzymes leading to a higher maximal velocity of the reactions they catalyze. The same holds true for transport processes, where the transport velocity is typically scaled with amount of transporters present in the membrane, which can be approximated by the membrane area in case of locally evenly distributed transporters.

This chapter was concerned with the analysis of the effects of different scaling approaches on output functions of a biochemical system with varying sizes and geometries, modeled with ODEs. Models using partial differential equations have been used for the consideration of spacial aspects both on the intracellular and macroscopic level [67] in biological systems [68], with ODE models largely ignoring them. Oftentimes, ODE models are simplified to an extend, where spacial questions are completely ignored and a multi-compartment system is modeled as a single-compartment system, thereby ignoring aspects such as dynamically changing cell and compartment sizes and shapes.

Such is the case with the majority of the curated models on the BioModels database. If no changes in cellular or compartmental geometries and sizes are analyzed, these models are still able to deliver good results and describe experimental data. In fact, if the parameters of the model are chosen well, they do not perform differently from multi-compartment models whatever scaling method is applied. However, if one is interested in changing geometries such

as growing cells or if one wants to transfer the model onto another cell type, the modeling results can become unreliable if the right scaling of the kinetic transport rate laws with a subsequent adaption of the respective parameters is not undertaken.

As shown in this chapter, the effects of the area- vs. volume scaling range from neglectible to relevant, depending on the concrete system. In a model of NFAT signalling in T-cells, a doubling in nuclear membrane area with constant cytoplasmic and nuclear volume did not alter the output function significantly in the area-scaled version compared to the volume-scaled version. In contrast to this, changing the compartment sizes caused a notable difference in the output of the TGF-β signaling model by Zi *et al.*. Not only is the Smad-complex concentration sufficiently sensitive to the transport reactions, but the model architecture also means that the change compartment size has a notable impact on the output function. In more general terms, this means that - depending on how the system is decoded (signal amplitude *versus* signal duration) - the area-scaling model would transmit different information than the volume-scaling model unless the parameters are carefully adjusted.

In conclusion, this analysis demonstrates that including the membrane as scaling factor - or at least carefully adjusting the parameters of multi-compartment reactions - can be necessary to observe the correct model behavior. Nonetheless, the exact impact of not adjusting the model on the simulated behavior depends on the modeled system itself, its geometry and the control that a transport reactions holds over the behavior of the system.

Several software tools automatically scale with the volume in every case, if it is changed. In this chapter, I could show that this should not be done as it can lead to wrong model behaviors. Software like COPASI does instead correctly adjust the particle fluxes according to the impact that a changing volume of a compartment has. With the recently added feature of allowing for the definition of two-dimensional compartments, more models the membrane should be considered as a separate compartment or scaling-factor for reaction velocities.

Mathematical modeling of the vacuolar pH-homeostasis in Arabidopsis thaliana

4.1 Introduction

As sessile organisms, plants had the need to develop a set of adaptations to deal with their changing environmental conditions, such as water, light and nutrient availability. One such adaptation is the central vacuole, a compartment which often is the largest structure in a plant cell, comprising up to 90% of the cellular volume in some cases [69]. Early views did not attribute many functions to this organelle, which was seen as a space mainly filled with water and with little purpose (hence its name from *uacuus*, lat.: empty) [70]. Over time however, more functions of the plant vacuole were discovered, leading to today's view with the recognition of the vacuole as an important structure in plant cells for processes such as the regulation of osmotic pressure and cytosolic ion homeostasis, protein degradation and the storage of nutrients and secondary metabolic compounds. Now, we can discern two subtypes of vacuoles: the lytic vacuoles which are harboring a range of hydrolytic enzymes for protein digestion similar to lysosomes in other organisms, and the protein storage vacuole, keeping various defense and storage proteins inside [71].

To achieve this variety of functionality, the vacuole is in constant communication with other parts of the endomembrane system and the space outside the plasma membrane (the apoplast) through vesicular trafficking as well as with the cytoplasm through direct transport of compounds across the vacuolar membrane, termed the tonoplast, and through tonoplast-intrinsic factors. The tonoplast is host to a variety of transporters and molecules that enable the tethering of vesicles from other compartments [64]. Known vesicular trans-

port processes with the vacuole as the target include two types of clathrin coated vesicles, discerned by their adaptor proteins AP-1 and AP-2 as well as multivesicular bodies, all derived from the Trans-Golgi Network/Early Endosome (TGN/EE), which acts as a central hub in plants in which endocytic and exocytic pathways meet [72]. A direct vesicular communication from the Endoplasmic Reticulum (ER) has been described for young cells, essential for the formation of the vacuole [73]. Vesicular trafficking and fusion are powered by GTP through the action of a range of GTPases [74] [75], which allows for the eventual accumulation of compounds in the vacuole and replenishment of membrane bound proteins in the tonoplast [76] [77]. As for the transport of compounds from cytoplasm into vacuolar lumen, those are transported passively into the vacuole only if a concentration and/or electrostatic gradient is favoring it. Otherwise, energy sources such as ATP and PPi are used to transport some compounds into the vacuole, such as calcium and hydrogen ions/protons [78]. This is called primary active transport. Finally, secondary active transport occurs by utilizing the electrochemical gradient of a compound, channeling out this compound and thereby allowing for the transport of the other compound [79]. The plant vacuole contains many transporters that utilize the electrochemical gradient of protons (also termed proton motive force), with a higher concentration and a positive charge surplus inside the vacuole to pump compounds such as, among others, potassium and calcium ions into the vacuole, thereby making the proton motive force a central feature for the function of the vacuole [80].

It has been understood that two V-ATPases and one V-type PPase are responsible for the establishment of the proton gradient, using chemical energy stored in ATP and pyrophosphate, respectively, to power the pumping of protons from the cytosol into the vacuole [81]. Due to large possible variations in proton concentrations relevant in a range of fields, its value is most often given as its negative base ten logarithm, the pH. Within plant systems, the proton concentration can vary significantly, from less than 10^{-8} in peroxisomes to 10^{-5} in the apoplast. In Arabidopsis, the cytosolic pH typically is found to be held

rather constant at around pH 7.4. On the other hand, in the endomembrane system, the pH drops successively from ER (pH 6.4) to TGN/EE (pH 5.6) with the apoplast having a pH of around 5.0. The vacuolar pH in wild type root cells is typically recorded to fall around a value of 5.8 [82]. This is thought to be achieved by both biochemical and biophysical pH regulatory systems, also called pH stats, such as the buffering function of organic acids and phosphates and plasma membrane resident proton pumps and redox systems [83][84][85].

In a study from 2015, Kriegel *et al.* could show that the vacuolar lumen is still acidified by about 10 fold compared to the cytosol in a triple mutant of both the vacuolar ATPases and the vacuolar PPase. Only when applying concanamycin A to the cells, a drug inhibiting all V-type ATPases, could the vacuolar pH be raised to cytosolic levels. This indicates that the only known V-ATPase outside of the vacuolar membrane, the TGN/EE resident V-ATPase, is responsible for the rest acidification observed in the triple mutant [81].

To achieve this rest acidification of the vacuole, protons must be able to reach the vacuolar lumen through a so far unknown mechanism dependent on either the TGN/EE residident V-ATPase directly, or a secondary dependent process such as TGN/EE acidification, its ion balance or a subsequently potentially inflicted vesicular transport from TGN/EE to vacuole. For a proton gradient across the tonoplast to be stably maintained, energetic considerations must be accounted for, as protons can either be transported across the tonoplast using energy directly as is the case for proton pumps using ATP or PP_i, or indirectly by utilizing another ion's electrochemical gradient, which in turn has to have a proton independent energy source to be established. A third way is the usage of entropic forces, using a virtually irreversible process such as the fusion of vesicular membranes with the tonoplast [86] [87]. Since the TGN/EE has been shown to be among the most acidic organelles in Arabidopsis cells [88], it has been suggested that vesicles from the TGN/EE containing an excess of protons reach the vacuole and thereby contribute to its acidification, with an

inhibition of the TGN/EE acidification leading to a stop of vesicular transport to the vacuole. Another imaginable mechanism is the indirect transport of protons into the vacuole as proteins could reach the vacuole and hydrolyze there, with the subsequently produced amino acids acidifying the vacuole. Finally, a proton/ion antiporter could reverse its direction and inserting protons into the vacuole while releasing the corresponding counterions.

In the following, the different factors in the systems and their contribution to vacuolar pH-homeostasis will be discussed. After that, several hypotheses are postulated and tested with respect to their feasibility and explanatory power of experimental data using mathematical models of the system.

4.1.1 pH-regulation

To get a better picture of the pH homeostasis of the vacuole, a summary of the processes that are known so far to be involved is given here. An overview over those can be found in figure 5. While the cytosolic pH is set at around 7.4, the cellular compartments get an increasingly acidic pH from ER to TGN/EE. This is thought to be the effect of luminal connection of the compartments, with a steady increase of acidification due to proton pumps being located in the membrane of each compartment, in addition to differential pH regulation due to different proton outflux processes and kinetics as well as buffering compounds.

The cellular pH regulation is thought to include both a biochemical and a biophysical component. The biochemical pH stat is due to metabolic processes producing and consuming protons continuously, such as malate derived alcoholic and lactic fermentation processes as well as alternative route glycolysis and alternative pathway respiration [89]. Especially important in this context are enzymes couples that remove and add a carboxylic group from/to a shared metabolite. If those enzymes have, as it is common, a pH-dependend activity optimum, then there can be a point at which the pH-activity-curves of those two enzymes intersect. Lowering the pH from there typically leads to an in-

crease of activity for the decarboxylation step, whereas the oposite is true for an increase of pH, thus returning the pH to the intersection point. A typical example for this is the phosphoenolpyruvate carboxylase/malic enzyme couple [90].
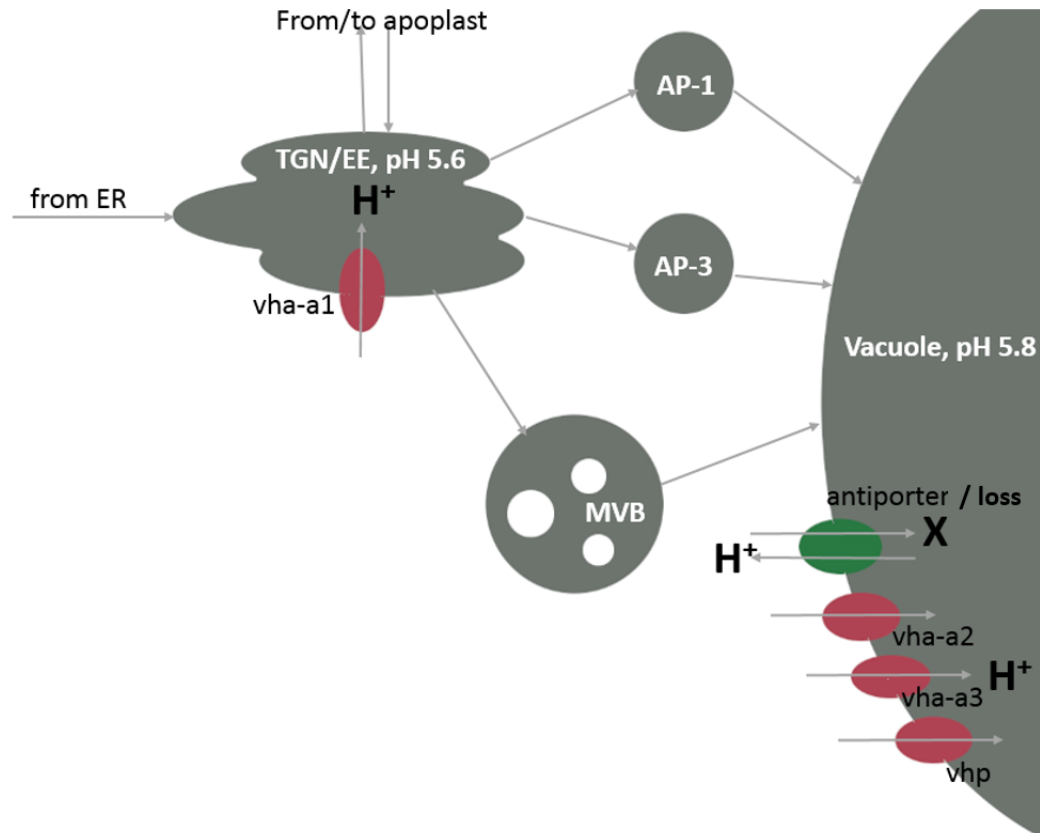
Figure 5: Overview over the processes able to influence the vacuolar pH. Besides the three proton pumps in the vacuolar membrane, the V-ATPases designated by their components (mutants: *vha-a2* and *vha-a3*) and the PPase (*vhp*), a variety of antiporters with diverse stoichiometries and counterions regulate the vacuolar pH directly. Additionally, vesicles from the TGN/EE are thought to contribute to the vacuolar pH, as well as, through an as-of-yet unknown mechanism, the TGN/EE-resident V-ATPase subtype (*vha-a1*).

The biophysical pH stat on the other hand is due to the pumping of protons by pumps or the secondary active outflux of protons through antiporters. Many components of the biophysical pH stat can be regulated by pH itself, thereby ensuring an optimal pH to be maintained across wide conditions [91]

[92]. Whereas the biochemical pH stat is mainly important for cytosolic pH regulation, the biophysical pH stat is heavily involved in all organelles, among them especially the vacuole due to its function for maintainance of the osmotic potential of the cell and nutrient storage. Besides the two pH stats mentioned, buffer systems contribute as well to the apparent proton concentration in a compartment. Buffers are aqueous solutions of weak bases and their conjugated acids or vice versa. By adding a strong acid to such a mixture in equilibrium, this equilibrium is shifted to the side of the protonated form, thus lowering the effectively added concentration of protons. Malate, citrate, phosphate and amino acids are the most prominent buffer components in plants, acting both cytosolically and in vacuoles. Buffer capacity is a typical measure of a compartmental ability to buffer pH changes, defined as

$$\beta = \frac{-dC}{dpH}$$

with C being the concentration of strong acid (or protons themselves) added to the solution.

4.1.2 Ions and their transporters

Different ions have an influence over the vacuolar pH both due to their contribution to the tonoplastic membrane potential and the way of being transported into the vacuole via proton/ion antiporters.

Potassium

As the most abundant inorganic ion with cytosolic concentrations held rather constant at around 75-100mM [93], potassium plays a major role in establishing and maintaining the osmotic potential of the cell. Vacuolar potassium concentrations are more variable, as vacuolar potassium is readily released into the cytoplasm to keep cytoplasmatic concentrations constant, but most reports indicate a range of vacuolar potassium concentrations from 75mM to 250mM in wildtype conditions [94]. The uptake and release into and from the cell is

tightly regulated by a set of transporters from the KT/HAK/KUP, TRK/HKT and the CPA cation proton antiporter families in addition to a range of potassium channels [95]. Inside the cell, the vacuole can take up potassium via a set of NHX potassium/proton antiporters, releasing it into the cytosol via TPK channels. Potassium also has been reported to regulate several enzymes and transporters such as asparaginase [96] and the vacuolar proton pumping PPase [97].

Calcium

Another important cation is calcium, the cytosolic concentration of which is held very low at 10-200 nM under normal conditions [98], but can rise to low millimolar concentrations as a signalling event [99]. This increase is facilitated by the influx of calcium from apoplast, vacuole and ER, all of which are assumed to have a manyfold higher calcium concentration under standard conditions, with vacuolar concentratons found at 1-10mM [100]. The immense concentration difference between cytosol and vacuole is thought to be maintained by both ACA1, a calcium pump powered by the hydrolysis of ATP and a set of calcium/proton antiporters of the CAX family. Calcium channels lead to the release of calcium into the cytosol. Upon receiving a signal such as abiotic stress, the opening probability of the calcium channels increases drastically, leading to a rapid outflux of calcium into the cytoplasm, where downstream effectors such as calmodulin-regulated proteins lead to a change in immediate enzyme activity or the expression of other effector proteins and thereby to the cellular answer to the signal trigger [101]. Calcium is believed to be heavily buffered both in the cytosol and in the vacuole, due to the abundance of calcium binding proteins such as calmodulin. Although direct measurements have been performed for only few cell types, it is believed that for 10-100 calcium ions in the cytosol, only one is present in its free form [102] [103].

To enable the maintenance of high cationic concentrations in the vacuole without the formation of a membrane potential so high that it would counteract

44

the further accumulation of cations, anions need to be present in the vacuole as well. Among the most common ones are organic acids, nitrate and chloride.

Organic acids

A variety of organic acids play an important role in plants. The most prominent ones are amino acids, malic acid and citric acid and their deprotonated forms. Amino acids, as the building blocks of proteins, occupy a central position in a plants metabolism. The production of proteins occurs on ribosomes in the cytosol or at the surface of the ER, whereas the degradation of proteins happens both in the cytosol via the ubiquitin-dependent pathway and in the vacuole through the action of proteases [104]. Under standard conditions, the concentrations of amino acids in both of those compartments is comparable and therefore does not significantly contribute to the membrane potential [105].

Nitrate

Nitrate is an important intermediate form in nitrogen assimilation, where nitrate is taken up into the cell and then stored in vacuole, where it can be released when needed, or reduced to nitrite in the cytosol and quickly further incorporated into amino acids in plastids [106]. The import of nitrate into the vacuole is thought to be governed mostly by CLC proton/nitrate antiporters, whereas the export mechanisms are not well understood as of yet [107]. Cytosolic concentrations have been reported to lie around 4mM, vacuolar ones range from 10mM to 80mM [108].

Chloride

Chloride is transported into the vacuole through proton antiporters of the CLC family and released through a range of anion channels. The role of this ion is thought to be only the dissipation of extreme charge levels, as any electrogentic import of protons into the vacuole would cease if the membrane potential grows too high [109].

4.1.3 Membrane potential

The membrane potential, as mentioned above, is the result of the assymetric distribution of charges on both sides of the vacuolar membrane. This leads to an additional force acting on ions, either supporting or counteracting the concentration gradient across a membrane. The exact value of the membrane potential across the tonoplast has not been determined definively, but is assumed to fall between -20 and -50 mV, averaging at around -35 mV, defining the vacuolar space as outside and the cytosol as inside [110][111][112]. The effect of the membrane potential on transport processes can be described by Ohm's law:

$$I = g * (V_m - E) \qquad (7)$$

with I being the current produced by a given ion, g the conductance, V_m the membrane potential and E the transporter's equilibrium potential. The equilibrium potential of an ion X on the other hand is determined by Nernst's equation:

$$E = \frac{RT}{zF} * ln\frac{[X]_{\text{outside}}}{[X]_{\text{inside}}} \qquad (8)$$

with R, T, F being the universal gas constant, the temperature and Faraday's constant, respectively and z the ion's charge.

Those two expressions demonstrate the dependence of the direction of an ion's movement across a membrane on both its concentration and the electrical gradient between the two respective compartments. No charge driven movement of the ion across the membrane occurs when $E = V_m$, so that only concentration gradients remain as a driving force of the transmembrane movement. To arrive at an expression for the mass flux J of an ion across a membrane, one can simply divide the current by the charge of a single ion and faraday's constant, which is the elementary charge times the number of particles per mole:

$$J = \frac{I}{zF} \qquad (9)$$

Since the membrane potential depends on all charges on both sides of the membrane and those in turn depend dynamically on each other, an exact description of the membrane potential at each time point can hardly be given. Instead, a simplifying assumption that the membrane potential is only dependent on proton concentrations can be taken, motivated by the observation that proton concentrations are of central importance to the membrane potential both due to their presence on both sides of the membrane as well as due to them acting as counterion for the antiport processes observed [113].

4.2 Materials and methods

4.2.1 Computational methods

The model was set up using COPASI version 4.23 build 184 [63] on a Windows 10 PC. Time courses were obtained through deterministic simulation using the LSODA algorithm [114]. Parameters were estimated using the experimental data described below with the use of global and local algorithms. As global algorithms, both the genetic algorithm [115] and the particle swarm [116] algorithm as implemented in COPASI were used. As a local optimizer, the Hooke-Jeeves algorithm was used [117]. The parameter estimation routines were run on a computing cluster 50 times for each global method. In case of particle swarm, the set up was 10,000 generations with a population of 100 parameter sets each and the random number generator turned on. For the genetic algorithm, the set up was 5,000 generations with a population of 200 parameter sets was chosen. The resulting model ensemble was subsequently analyzed using sensitivity analysis and time course simulations. Plots of time courses were generated using the statistical programming language R [118] using the packages "tidyverse" [119] and "ggthemes" [120]. Model schemes were constructed according to the SBGN standards using the software Vanted [121].

4.2.2 Collaborations

The experimental data has been provided by our collaborators from Karin Schumacher's lab at the COS, Heidelberg University. The cellular and vacuolar metrics (4.2.3a) have been measured by Falco Krüger [122]. Anne Kriegel measured the vacuolar pH in proton pump mutants [81]. Melanie Krebs contributed the datasets of the cellular buffer capacity (4.2.3b) and, together with Catharina Larasati, provided the time course data of the vacuolar pH under concanamycin A treatment (4.2.3d). The TGN/EE pH measurements (4.2.3c) and the vacuolar pH measurements in the vesicle trafficking mutants (4.2.3e) have been performed by Stefan Scholl [123] [88]. Here, I will discuss the conclusions one can draw from the experiments and how they will be used in the modeling process.

4.2.3 Experimental data

4.2.3a Cellular and vacuolar geometries

The cellular and vacuolar volumes and surface areas in root tissue were measured using the fluorescent dye BCECF-AM, which specifically accumulates in lytic vacuoles, to understand their developmental differences. Plasma membranes were stained with FM4-64. Subsequent detection of the stain was achieved with Confocal Laser Scanning Microscopy (CLSM). By recording subsequent images along the Z-axis, 3D information of the cells and vacuoles was obtained through surface rendering. For the study presented here, only the data from the elongation zone was taken, as the rest of the experimental data was obtained from the root elongation zone as well. For comparison and possible model adaptation to different zones, the other data is shown here, too (table 4).

Developmental zone	Cellular volume	Vacuolar volume	Vacuolar surface
Meristematic zone	$1260\mu\mathrm{m}^3$	$179\mu\mathrm{m}^3$	$591\mu\mathrm{m}^2$
Elongation zone	$3080\mu\mathrm{m}^3$	$654\mu\mathrm{m}^3$	$1537\mu\mathrm{m}^2$
Differentiation zone	$16740\mu\mathrm{m}^3$	$14700\mu\mathrm{m}^3$	$4874\mu\mathrm{m}^2$

Table 4: An overview over the measured surface areas and volumes of the whole cell and the vacuole in different developmental zones of the root. Krüger (2017) [122].

For the model, the vacuolar volume and surface were taken as shown in the data. The cytosolic volume was obtained by subtracting the vacuolar volume from the cytoplasmic volume. This leads to a potentially slight overestimation of the cytosolic volume, as the nucleus and other compartments are not taken into account. Since cytosolic concentrations of a number of molecular species included in the model will be fixed, this is assumed to be of little relevance for the model's performance. An exception to this are the calcium ions, for which the implications will be discussed in section 4.5.

4.2.3b Buffer capacity

The potential to buffer pH changes in the cell is easily described by the buffer capacity. This indicates the amount of protons needed for the decrease of the pH of one unit. In an unbuffered system, a 10-fold increase of protons leads to a drop of the pH by one unit. If buffers are present, some of the added protons will not be present in their free form and therefore not contribute to a change of pH, as described in section 4.1.1.

Here, the buffer capacity of the whole cell lysate has been measured through titration. Since in mature cells like the ones taken here for the measurement, vacuoles represent the major compartment in the cell, the result is taken as an approximation of the vacuolar buffer capacities (figure 6).
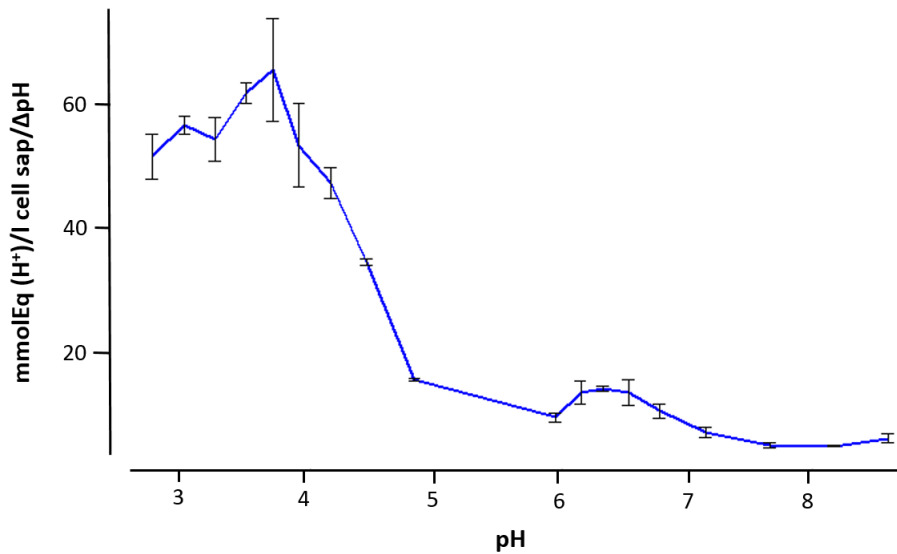
Figure 6: The pH region relevant for the modeling process described later is from approximately pH 5.5 to pH 7.4. In this region, the buffer capacity is approximately constant at slightly below 20 mmolEq(H^+)/l cell sap/ΔpH. This means an increase of around 20 mmol per liter of protons leads to an decrease of the pH by a single unit. Krebs and Schumacher (unpublished).

4.2.3c TGN/EE

To obtain the following pH values, pH in the TGN/EE was measured using a ratiometric approach with a genetically encoded biosensor, pHusion, which consists of a tandem concatenation of enhanced green fluorescent protein and monomeric red fluorescent protein [124]. Those are coupled to a protein specifically located to the membrane of the organelle of interest. In the case of the TGN/EE, this was the C-terminus of SYP61. Subsequent measurement of fluorescence intensities was done using CLSM.

The wildtype plant (Col-0) exhibits the cytosolic pH of 7.4, whereas the TGN/EE exhibits a more acidic pH of 5.6.

Additionally, the pH inside the TGN/EE has been measured with more spacial resolution to obtain an idea of the differential proton concentration within this organelle (figure 7). Here, no absolute pH values could be given for each subcompartmental region, but one can assume the largest and smallest single

values measured for the TGN/EE to represent the pH values in the most alcalic and acidic regions of the organelle, respectively.
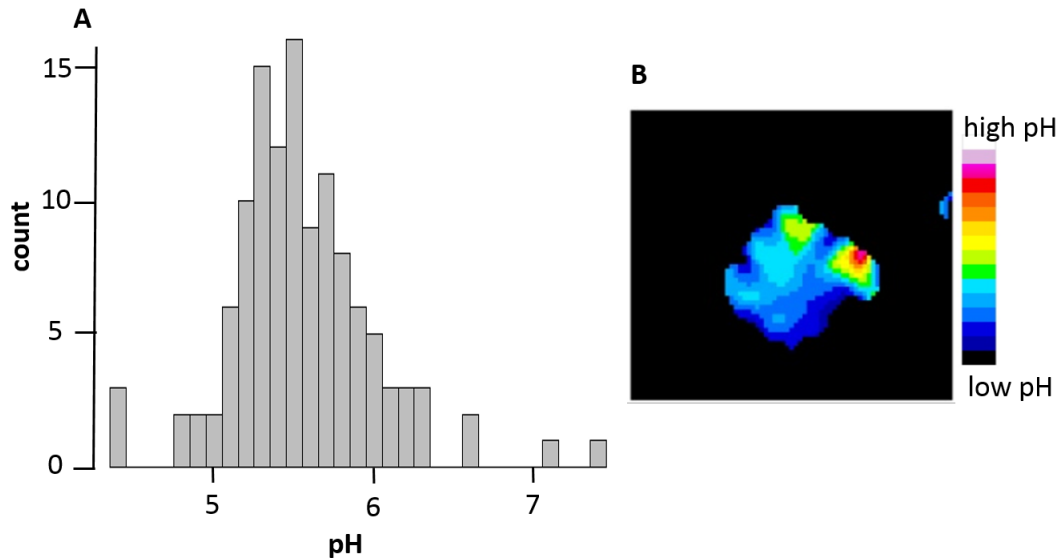
Figure 7: Overview over the pH in the TGN/EE. The distribution of pH values measured in a single TGN/EE (A). The TGN/EE exhibits a pH gradient internally (B). Data provided by Scholl (2018) [123]

4.2.3d Proton pump mutants and concanamycin A treatment

As shown by Anne Kriegel *et al.* [81] using the pH dependent vacuolar dye BCECF-AM and CLSM, a knock-out of both vacuolar V-ATPases does lead to an increase of the vacuolar pH to a value of around 6.4, still notably more acidic than the cytosolic pH of 7.4. It could be ruled out that the rest acidification is due to the contribution of the vacuolar PPase, as in triple mutants, the vacuolar pH is still to be found at around 6.5.

Concanamycin A is a specific inhibitor of the V-ATPases, thereby inhibiting a significant proportion of vacuolar acidification (*vha-a2* and *vha-a3*) as well as the only known acidifying factor of the TGN/EE (*vha-a1*). Only upon treatment of the cells with concanamycin A, the vacuolar pH reaches cytosolic levels in the triple mutant, demonstrating the TGN/EE-resident V-ATPase to

be responsible for the vacuolar rest acidification through an as of yet unknown mechanism (figure 8).
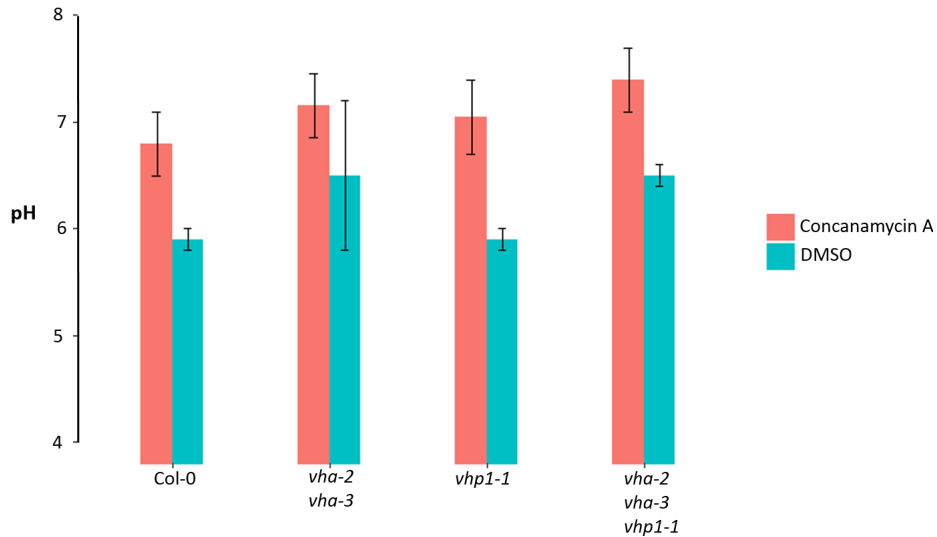
Figure 8: The vacuolar pH under different conditions. In the wildtype situation (Col-0), the vacuolar pH is measured at around pH 5.8. both double mutants of the V-ATPase subtypes vha-a2 and vha-a3 and triple mutants of the V-ATPases and the PPase vhp1-1 are still acidified compared to the cytosolic situation. Only the addition of concanamycin A equalizes the vacuolar pH with the pH in the cytosol. Kriegel et al. (2015) [81]

To get an idea of the dynamics of the system, time course data for the vacuolar pH under concanamycin A treatment was obtained as well (figure 9). The time course data shows a fast alkalization of the vacuole in the beginning, with a significantly flatter curve for pH values above around 6.8. The final pH of 7.4 was not reached during the timeframe of the measurement. It has to be noted here, that the time course does not represent a simple exponential decay of the vacuolar proton concentration, as would be assumed if a simple (mass action) proton loss is responsible for the outflux of protons. The significantly slower outflux of protons as soon as a pH of around 6.8 is reached can thus be explained with a more complex kinetic system: either an at least two component loss system, in which a fast component is inhibited when the pH has risen beyond a certain threshold, or an additional proton influx component, that gets activated in the same high-pH region. Since for the typical components of the proton

52

loss, the antiporters described in section 4.1.3, no such regulation is known, the additional influx component will be given special attention in section 4.4.5.
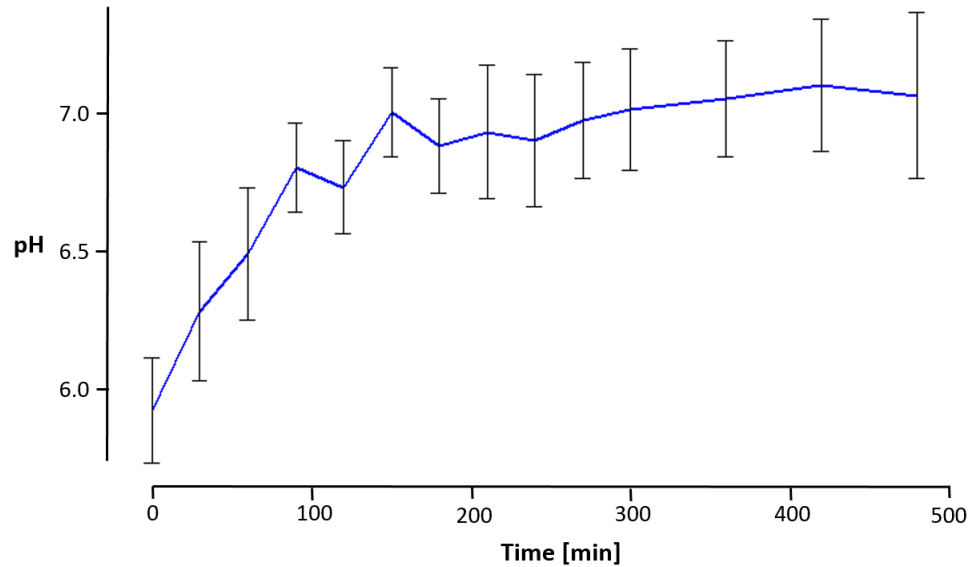
Figure 9: Time course of the vacuolar pH under addition of $5000\mu L$ concanamycin A. Following a rapid alkalization up to a pH of around 6.8 to 7.0, the pH adjusts only very slowly to cytosolic levels, which are not reached before 500 min of concanamycin A treatment. Lasarati, Krebs, Schumacher (unpublished).

4.2.3e Vesicles

To get an idea of the nature of the contribution of the TGN/EE to the vacuolar acidification, knock-out lines of the three known vesicular pathways from TGN/EE to vacuole were generated and the vacuolar pH was measured. BCECF-AM and CLSM was used to measure the vacuolar pH. The results show no effect of the knock-out of multivesicular bodies (MVBs), a slight increase of vacuolar pH in AP-3 KO lines to 6.0 and a slight decrease of vacuolar pH in AP-1 KO lines to 5.6 (figure 10).
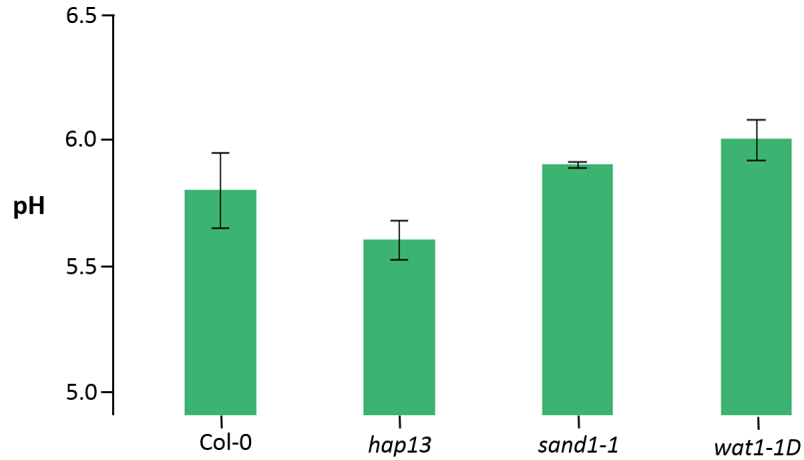
Figure 10: Effects of vesicular trafficking mutants on the vacuolar pH. Inhibiting MVBs (sand1-1) does not alter the vacuolar pH, whereas the inhibition of AP-1 (hap13) lowers the vacuolar pH to 5.6 and AP-3 (wat1-1D) inhibition leads to an increase of the vacuolar pH to 6.0. Scholl (2018) [123]

If the observed effect indeed is significant, the data can be explained in several ways. The acidification seen in the AP-1 KO line could mean that AP-1 transports an alkalyzing factor such as one of the antiporters in the system, a lack of which would then lead to a higher vacuolar proton concentration in steady state. Reversely, AP-3 could transport acidifying factors such as proton pumps, protons themselves or proton-releasing factors that would explain the lower vacuolar proton concentration in the KO lines. Furthermore, not both of these explanations have to be true at the same time, as the absence of one of the vesicle types could lead to an increase transport of the other and thereby have the oposite effect to their knockout.

4.3 Results

In this section, I will lay out four hypotheses to describe the observed phenomena of vacuolar rest acidification in vha-a2/vha-a3/vhp1-1 triple mutants and its abolishment upon application of concanamycin A. To do so, different ODE models describing the time dependent concentration of protons in the vacuole

were established and tested using the experimental data introduced above. The hypotheses are:

1. A direct transport of protons via vesicels or through an additional proton pump
2. Protons released by protein degradation
3. A reversal of the calcium/proton antiporter (CAX) direction.

The first decision to take is whether to include the membrane potential explicitly in the models. For the direct proton transport models and the protein degradation model, the membrane potential was not included for two reasons. First, data of ion concentrations is sparse, especially so under the conditions tested here, and therefore an exact dependence of the involved processes including their effect on membrane potential would introduce a high amount of uncertainty in the models, rendering any effort for quantitative prediction fruitless. Second, and more importantly, the first two hypotheses are practically independent of membrane potential, as the majority of the ions involved in proton homeostasis processes are either imported into the vacuole in a non-electrogenic manner (potassium, nitrate, most of the amino acids) or serve purely as a membrane potential dissipator (chloride), which thereby does not help in explaining the energetic requirements to establish the proton gradient observed in the triple mutant.

For the hypothesis involving the reversal of the calcium-proton antiporter on the other hand it is crucial to include the membrane potential, as the antiporter itself is electrogenic and thus critically dependent on the electrochemical potential across the membrane, the implementation of which will be described in detail in chapter 4.3.4.

4.3.1 Core model of vacuolar proton homeostasis

Construction of the model

The cytosolic pH does not change significantly during the experiments performed for this study, due to large biochemical and biophysical pH stats, so it was fixed in the model at a value of 7.4. The known processes involved in vacuolar proton homeostasis are the proton import by the two V-ATPases and the vacuolar PPase as well as a proton loss through a multitude of different antiporters. Since the activities of the two V-ATPases are experimentally not distinguishable under the circumstances described here, a single proton V-ATPase process was modeled employing simple Michaelis-Menten kinetics. The V-ATPase activity is dependent on vacuolar pH only at nonphysiological cytosolic pH values, so no additional regulation of the V-ATPase activity by either side's pH was included [91]. Additionally, the V-PPase was modelled in the same way. As the cytosolic ATP level is assumed constant, only protons enter the reaction.

There are many antiport processes, exchanging protons with a large set of different compounds, each with their own stoichiometry and kinetics. The by far largest pool of ions transported into the vacuole using the proton gradient as an energy source is potassium through the NHX1,2,3 and 4 antiporters. As the membrane potential is not included here, calcium antiporters were not modelled seperately but rather implicitly assumed to be included in the potassium antiport processes, as the cytosolic concentration of calcium is negligible compared to potassium. The antiporter was modeled using convenience kinetics as described in [125]. Thermodynamic constraints require Haldane's relationship to be true [126], onto which the model was restrained so that no accumulation of a compound without the usage of energy can be achieved. Additionally, to enable potassium to exit the vacuolar lumen, the potassium channel TPK1 was modeled using simple mass action kinetics.

In addition to the described in- and effluxes of protons, a buffer system inside

the vacuole was constructed to account for the multitude of molecular compounds capable of buffering the vacuolar sap. To approximate the buffering potential of the vacuole (figure 6) without adding a too high complexity, 4 simple buffers with different pKa values were used to form a stepwise distributed buffer system, employing fast acting mass action kinetics. The pKa values were chosen to be 3, 4, 5 and 6, respectively, similar to previous studies [127] and motivated by the pKa values of the common vacuolar buffers malate, citrate and phosphate. Their pKa values range from approximately 3 of the first citrate deprotonation to approximately 7 of phosphate [128]. The total vacuolar buffer concentration was left open in the range of 20 mM to 40 mM, equally distributed among the four buffers, as their concentrations range in the low millimolar range each [129] [130]. Smaller variations of the buffer capacity in the mM range did not significantly alter the behavior of the model significantly. An overview over the core model is shown in figure 11.
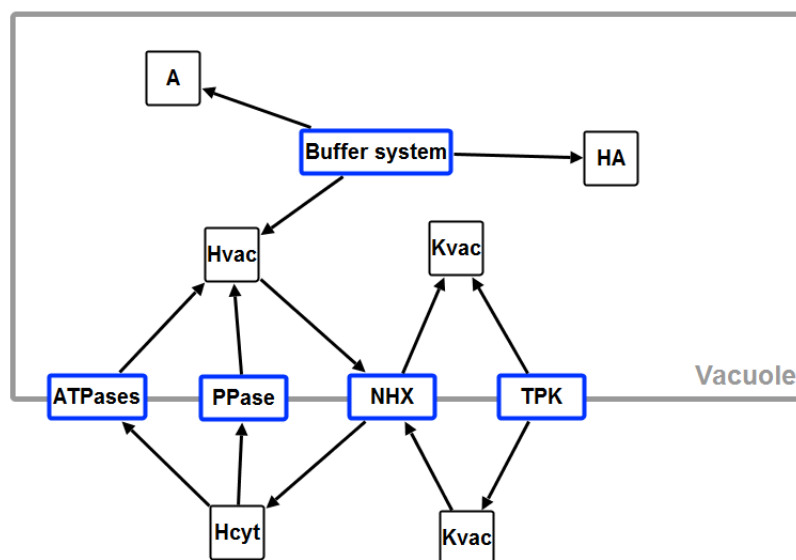
Figure 11: An overview over the core model. Reactions/enzymes are drawn in blue, species in back. The processes governed by the antiporter NHX and the potassium channel TPK can be simplified to a proton loss, ignoring changes in potassium concentrations. H = protons, K = potassium, A = deprotonized buffer component, HA = protonized buffer component.

Overall, the core model's proton fluxes can be summarized as

$$\frac{dH^+(t)}{dt} = -(J_{\text{VHA2/3}} + J_{\text{VHP}} + J_{\text{Buffer}} - J_{\text{antiporter}}) \qquad (10)$$

with J denoting the flux of protons, VHA2/3 as the V-ATPases and VHP as the PPase.

The ODEs for the model can be found in appendix B1.1.

Fitting of the core model's parameters

The buffer system was constructed by assuming 4 different buffer components, each of the same total concentration but different pKa values (3, 4, 5 and 6), as described in the previous paragraph. The parameters for the buffer system were fitted to the data shown in figure 6. The relevant pH range for the conditions presented here are between pH 5.5 and pH 7.5, where the buffer capacity of the cell sap is mostly constant at around 15 mmolEq H^+/l cell sap/ΔpH. Since the vacuole occupies most of the cell volume, this value is directly taken as the buffer capacity for the vacuolar lumen at all relevant pH values.

In the concanamycin A treated cells, it is assumed that all proton import through the V-ATPases into the vacuole comes to a standstill immediately after the application of concanamycin A, which is justified due to the rapid initial release of protons observed. As the loss and the PPase are the only proton translocating systems assumed to be left when concanamycin A is applied, their parameters could be fitted to the time course data, which should then unequivocally describe the ratio of the PPase flux to the loss flux. The time course shows a rather fast decrease of vacuolar proton concentration up till around pH 6.8 followed by a slow increase of pH, not reaching pH 7.4 during the measured time. This cannot be explained by a simple mass-action kinetics for the loss, which would produce a simple exponential decay of the proton

concentration. Since many processes are involved in the proton loss, it is conceivable to assume a regulation of some of the processes involved, such as an inhibition of antiporters by low proton numbers. Since this seems to occur only at a pH of around 6.8 however, this slowdown of the proton outflux is not relevant for describing the rest-acidification at pH 6.5. As shown in figure 12, the data for the efflux of protons through the loss can be described by the model when ignoring the final slowdown of the loss. Of course, a decision must be taken whether the model should describe the initial fast loss or the slow component better. Since the slow component is thought to occur due to some as of yet unknown regulation, the fast component is the more relevant factor to be fitted. As it is the case for all simple production-degradation cases, the degradation (here: loss) part of the process determines the steepness of the curve. Thus, the loss component was the determining factor for this. Due to the uncertainty of the eventual reasons behind the observed time course, a range of fits was taken as suitable for further analysis.
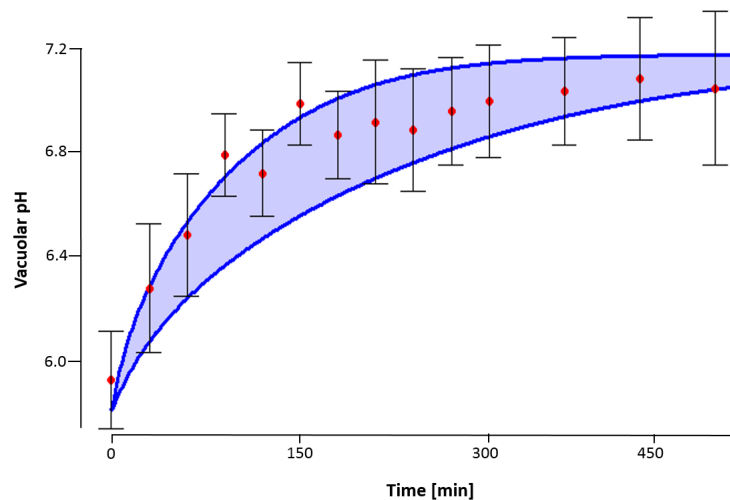
Figure 12: The range of accepted fits of the core model to the data of the vacuolar pH development in concanamycin A treated cells. The model can fit the time course data, with the exception of the eventual slowdown of the proton efflux observed after around 150 min.

The potassium concentrations in the mutants and under concanamycin A treatment are not known, so to reduce model complexity, potassium was eliminated

from the model and the loss kinetics adjusted to follow simple mass action kinetics. This model was examined and compared to the model including potassium. The inclusion of potassium did not alter the outcome of the fit as no exact information about potassium concentrations in the circumstances described here was available. Therefore, for the other models, potassium was not included anymore and the proton loss was handled as governed by mass action kinetics.

4.3.2 Hypothesis 1: Direct transport of protons into the vacuole via pumps or vesicles

4.3.2a Unknown proton pump

Construction of the model

To investigate whether the rest acidification of the vacuole in the *vha2/3* and *vhp1-1* knockout lines can be described by a simple pumping of protons into the vacuole by a proton pump transported via vesicles from the TGN/EE other than the two tonoplast resident V-ATPases or the PPase, it is useful to calculate the number of protons per second needed to maintain the pH difference of approximately 1 pH unit across the tonoplast, between 7.4 in the cytosol and 6.5 in the vacuole. This is dependent on the speed of proton efflux from the vacuole, represented by the loss term in the core model. The core model was therefore extended by an additional term describing the translocation of protons from the cytoplasm into the vacuole governed by Michaelis-Menten-kinetics.

The model was fitted to the triple mutant data, the time course data as well as the wildtype data (Col-0 in figure 8). The parameter space of the V-ATPases was restricted to allow only for realistic pump activities, which have been reported to lie around 60-90 protons per second per ATPase in mung bean and oat [131] [132]. Broader ranges of up to 200 protons per second as maximal rates were accepted. There are an estimated 1000-3000 V-ATPases per μm^2 tonoplast [133] [134]. With the surface measured to be about 1537 μm^2 (table 4), that leads to a total amount of 300,000 - 5,000,000 V-ATPases in the tonoplast, through which one can arrive at a maximal rate of about 3E7 to 1E9 protons being inserted into the vacuole per second through all V-ATPases.

Analysis of the model

Under triple mutant simulating conditions, setting the flux through the V-

ATPases and PPase to zero, the flux through the hypothesized proton pump needed to acidify the vacuole to a pH of 6.4 was calculated and compared to the steady state flux through the V-ATPases under steady state conditions, showing that approximately 16 to 18% of the wildtype flux of VHA-a2/3 is needed to maintain the observed acidification under vha2/3 knockout conditions, if the unknown pump is only active in the triple mutant. If the unknown pump is active in all cases but the concanamycin A treated cells, the unknown pump must exhibit a steady state flux of around 20% of the V-ATPase flux.

As the only other V-ATPase in Arabidopsis that could possibly be inhibited by concanamycin A, VHA-a1 could not neither be detected via fluorescence microscopy in the tonoplast, nor was there any V-ATPase activity detectable in tonoplasts in mutant strains of the two intrinsic tonoplast V-ATPases [135]. By assuming a similar activity as the other V-ATPases, one can therefore savely exclude the possibility of tonoplast resident VHA-a1 being responsible for the observed rest acidificytion in the *vha-a2/3* lines. Proton pumping P-ATPases like the one found at the plasma membrane are also not likely to be responsible for the rest acidification, as Kriegel *et al.* could show that vanadate, a P-ATPase inhibitor, did not significantly alter vacuolar pH in *vha-a2/3* knockout lines [81]. No other proton pump is known in Arabidopsis, and whole proteome studies do not suggest the presence of any as of yet unknown proton pump.
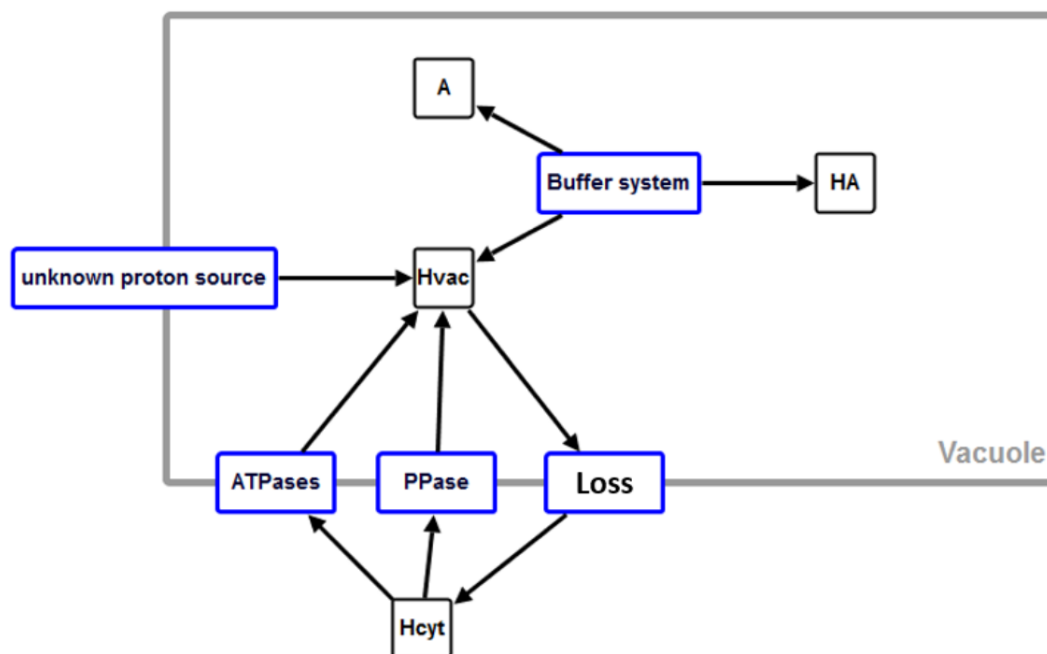
Figure 13: An overview over the direct proton import model. Reactions/enzymes are drawn in blue, species in back. An unknown proton source was included, using either a constant influx (from vesicles) or a Michaelis-Menten (unknown proton pump) kinetics. H = protons, A = deprotonized buffer component, HA = protonized buffer component.

4.3.2b Vesicular proton transport

Analysis of the model

As suggested by the dataset in figure 10, vesicular trafficking from the TGN/EE to the vacuole could directly be involved in the establishment of the rest acidification. To test whether protons themselves could be transported through AP-3 vesicles and acidify the vacuole significantly, instead of an additional proton pump, proton transport by the AP3 vesicles into the vacuole was modelled explicitly.

Similar to the calculations above, the parameters for the vesicular transport were determined by using the *vha-a2/3* dataset, with the flux of protons

through the vesicles necessary being around a fifth of those reaching the vacuole through the V-ATPases, totaling around 3E+7 protons per second being transported through vesicles. Assuming the intravesicular pH to be the same as the pH of their organelle of origin, the TGN/EE (5.6), and taking the mean diameter of clathrin-coated vesicles such as the ones designated by AP3 of 60 nm [136], an average of a single proton is transported per vesicle. That in turn means a total of 3E+7 AP3 vesicles would need to arrive at the tonoplast per second. A mean half life of clathrin coated vesicles such as AP-3 of around 10-30s [137] [138] could be found for other cell types. Since there are up to a few hundreds of golgi bodies per cell [139] and an average of 4 TGN/EE units observed per golgi body [140], it is assumed that a maximum of 1000 TGN/EE bodies exist at a given time per cell. Taking this information together, every single TGN/EE body would have to produce up to 1E5 vesicles per second. To picture the impossibility of this, one can see that without a large scale retrograde transport or recycling of membrane material, the tonoplast would in this case grow by 2fold each second, which can safely be ruled out. The idea that AP3 vesicles contain more protons than that requires the acceptance of either a local accumulation of protons in the TGN/EE at the site where AP3 vesicles form, or a proton pump located on the vesicular membranes, acidifying the vesicles on their way to the vacuole.

An exemplary parameter set for the unknown pump-hypothesis is shown in table 5. Buffer parameters remain unaltered from the core model. Km values of the pumps can be altered alongside their V values while keeping the model output and drawn conclusions unaffected. Here, Km values in the range of natural cytosolic proton concentrations in the system were taken.

Parameter name	Parameter description	Value
$V_{(loss)}$	mass action constant for proton loss, both directions	3.21E-7 $\mu M \mu m^{-2} min^{-1}$
$V_{(unknown\_pump)}$	maximal velocity of unknown pump	1.98E-7 $\mu M \mu m^{-2} min^{-1}$
$Km_{(unknown\_pump)}$	Km of unknown pump	0.013 μM
$V_{(ATPase)}$	maximal velocity of ATPase	6.45E-7 $\mu M \mu m^{-2} min^{-1}$
$Km_{(ATPase)}$	Km of ATPase	0.013 μM
$V_{(PPase)}$	maximal velocity of PPase	6.63E-9 $\mu M \mu m^{-2} min^{-1}$
$Km_{(PPase)}$	Km of PPase	0.0097 μM

Table 5: An exemplary set of fitted parameters for the unknown pump model. No big variations of parameter values were possible, as the concanamycin timecourse is determined only by the ratio of proton loss to PPase activity. Those in turn must have a fixed activity ratio to the ATPase, as determined by the wildtype. Changing the Km values of the pumps alongside their V values accordingly leaves the model output and conclusions as written in the text unaltered. Unusual parameter units arise from the scaling with the vacuolar surface area, as described in chapter 3.

Analyzing the TGN/EE's internal pH gradient

For an evaluation of the possibility of a regional accumulation of protons in the TGN/EE, one can look at figure 7B, where an exemplary TGN/EE body and its internal pH are shown. If the pH gradient observed is caused by a specific mechanism trapping protons at a given spot, this spot could then develop into a bud and become a highly acidified vesicle. Otherwise, the regional differences could stem from the locally restricted existance of antiporters. In this case, the pH gradient might simply be explained by proton diffusion through the TGN/EE. To assess the probability of this idea, a simple model of the TGN/EE is taken, in which I assume a spherical TGN/EE body with a diameter of 500nm. Further, V-ATPases are assumed to be uniformly distributed all over the membrane, with the proton loss being only found at a single spot of the membrane. The diffusion time t_{diff} can be approximated by

$$t_{\text{diff}} \approx \frac{x^2}{6D} \tag{11}$$

with x as the mean displacement of the particle and D its diffusion constant. This approximation can be obtained by calculating the probability density function of a particle from the diffusion equation and find the time dependend mean squared displacement of the particle from there.

The diffusion constant for protons is around $7{,}000\mu m^2$ [141]. As a uniform distribution of ATPases in the membrane is assumed, the entry point of protons into the TGN/EE has to be calculated and averaged over the whole TGN/EE, which can then be taken as the mean displacement x. To do so, one can imagine a line from the point of the proton loss to its antipodal point. At each point on this line, the infinitessimal surface area of the TGN/EE perpendicular to this can be calculated, by calculating the circumference of a circle that is formed through the intersection of a normal plane at this point with the spheric surface. This infinitesimal area is just the circumference of that circle, $2*\pi*r$, with r being the radius of the sphere at that point. To simplify the calculations, r can

66

be assumed to change sinusoidal over the length of the leak-antipodal-line:

$$r \approx 250nm * sin(\frac{\pi}{500nm} * x) \tag{12}$$

This can be plugged into eq. 11, and summing this up over the whole length of the TGN/EE and taking the average by dividing it by the total surface area, one arrives at a rough approximation of the time it takes a proton to travel from its point of entry to its point of exit:

$$t_{\text{diff}} \approx \frac{\int_0^{500} *\frac{x^2}{6D} * sin(\frac{\pi}{500nm} * x)dx}{A_{\text{tot}}} \tag{13}$$

which resolves to around 2.25E-6 s, meaning around 443,500 protons per second being imported to keep up with the diffusion under the assumption of immediate expulsion through the leak. Since this is unlikely, fewer protons are actually needed, but this value serves as a proxy to estimate the maximally needed number of protons to be inserted into the TGN/EE per second.

If the ATPase density of the TGN/EE is in a similar range as it is for the vacuole, one can assume to find between 1400 and 5000 ATPases in the membrane, so each of them must pump at around 90-300 protons per second, which is in accord with the typical ATPase pumping speed discussed above. Therefore, there is no evidence for a local accumulation of protons by other means than a specifically localized leak.
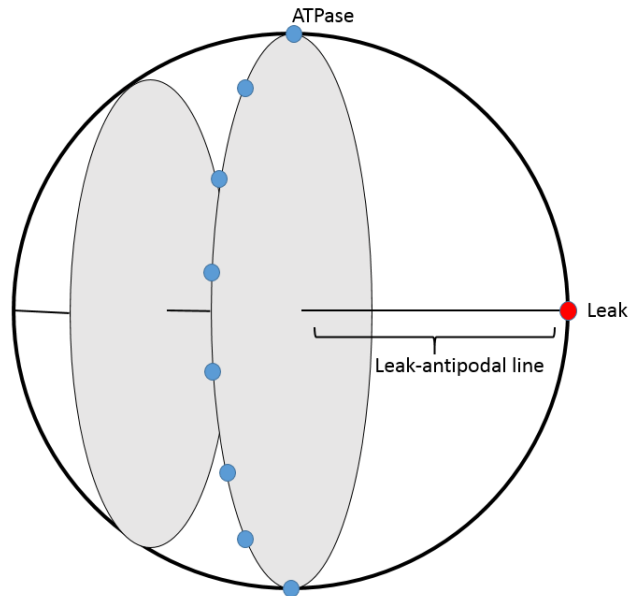
Figure 14: Scheme of the TGN/EE for calculating proton diffusion. A spherical TGN/EE is assumed, with a single point of proton outflux/leak (red) and a uniformly distributed influx through ATPases (blue). To average the diffusion time of protons from their points of entry to their point of exit, the TGN/EE was sliced orthogonally at infinite spots along an antipodal line through the leak (exemplarily: grey areas). The circumference of those slices correspont to an infinitesimal surface of the TGN/EE, on which a proportional number of ATPases sit.

4.3.3 Hypothesis 2: Release of protons by amino acids derived from protein degradation

Construction of the model

One of the vacuolar functions in plants is protein degradation. As could be shown, the vacuoles of plants lacking the β subunit of the AP3 complex on vesicles do not develop their lytic functions properly, wth proteins accumulating in the vacuoles, suggesting an important role for AP3 in protein degradation [142]. The isoelectric points for amino acids ranges from below 3 in aspartic acid to almost 11 in arginine, and the isoelectric point for amino acids without an extra acid or base group can be found in the range of 5 to 6. The

weighted average of the isoelectric point of amino acids can then be calculated by knowing the relative amino acid composition of proteins, which has been measured for *A. thaliana* leaves [143]. From this data and the knowledge of each amino acid's isoelectric point [144], one arrives at an average isoelectric point of around 6.0. This means that in the vacuole of cells without functional vacuolar V-ATPases (reaching a pH of 7.2, without TGN/EE contribution; concanamycin A experiment), a certain amount of amino acids in the vacuole are present in their deprotonated form and thereby effectively releasing a proton to their surrounding when produced. To test whether this is enough to provide for the acidification of the vacuole down to a pH of 6.5, the core model was enhanced by a module of protein degradation. For that, a simple steady import of proteins was added, in addition to mass action reactions describing the protonation and deprotonation of the NH2 and COOH groups. The pKa values were set to the average pKas of those α-carboxyl (2.18) and α-ammonium (9.32) groups. The transition between different protonation states occurs through fast acting mass action kinetics, the kinetic constants of which could be set up through knowledge of the pKa values and the given pH of the system using the Henderson-Hasselbalch equation:

$$pH = pKa * log(\frac{base}{acid}) \tag{14}$$

with base and acid refering to the concentrations of the deprotonated and protonated form of the amino acid, respectively [145] [146].

Furthermore, export reactions for the amino acids were formulated. Since there is not much detailed knowledge about the biological mechanisms of amino acid export, all protonation states of the amino acids are assumed to be exported utilizing the same kinetics in order to estimate the maximally possible acidification of vacuoles by protein degradation. To get an idea of the average number of amino acids per protein in *A. thaliana*, one can assume a lognormal distribution of protein lengths, and taking the parameters calculated in [147],

one can calculate the expected value E of protein length with

$$E = exp(\mu + \sigma^2/2) \tag{15}$$

with μ and σ being the parameters found in [147]. This resolves to around 402 amino acids per protein. Each imported protein is assumed to immediately degrade into this number of amino acids.
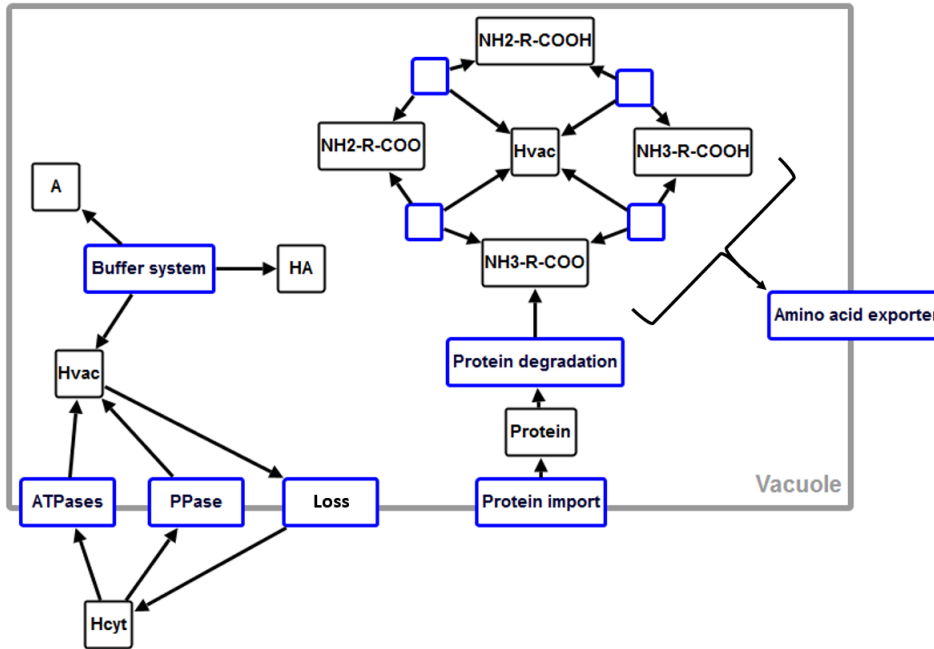
Figure 15: An overview over the protein degradation model. Reactions/enzymes are drawn in blue, species in back. In addition to the core model, a protein import and the degradation to amino acids was implemented. Each amino acid end group can be (de-)protonized, releasing/uptaking protons in the process. Each amino acid protonation state can be exported through the same exporter. H = protons, A = deprotonized buffer component, HA = protonized buffer component, NH2/3-R-COO/COOH = (de-)protonized amine and carboxy groups of amino acids.

Analysis of the model

Fitting the model to the datasets of the concanamycin A time course, the triple mutant and the wildtype (figures 8 and 9), one obtains a necessary im-

port flux of at least 1E-5 μmol proteins per minute, or a total of around 6E12 proteins, taking the slowest proton loss fit (see chapter 4.3.1). The average concentration of proteins in eukaryotes lies between 50 and 200mg/ml [148]. If this is true for *A. thaliana* root cells, that means an effective concentration of around 3mM, or a total number of proteins of between 4 and 5E9, excluding non-soluble proteins. Taken together, this would suggest a turnover of the whole plant proteome within just around 20 hours. Estimates of the average turnover rate of proteins however render this improbably, as around 3.5% of proteins are degraded per day [149]. It is important to note, that not all proteins are degraded in the vacuole, therefore lowering the actual number of proteins imported into the vacuole for degradation. Overall, it seems unlikely that protein degradation alone is sufficient to describe the observed rest acidification in the triple mutant. An overview over an exemplary parameter set can be found in table 6. The core model's parameters are found in the same range as before.

Parameter name	Parameter description	Value
$V_{(loss)}$	mass action constant for proton loss, both directions	3.44E-7 $\mu M \mu m^{-2} min^{-1}$
$V_{(ATPase)}$	maximal velocity of ATPase	7.82E-7 $\mu M \mu m^{-2} min^{-1}$
$Km_{(ATPase)}$	Km of ATPase	0.011 μM
$V_{(PPase)}$	maximal velocity of PPase	6.23E-9 $\mu M \mu m^{-2} min^{-1}$
$Km_{(PPase)}$	Km of PPase	0.0086 μM
$k1_{(export)}$	exemplary export rate constant for amino acids	1.58E-11 $l \mu m^{-2} min^{-1}$
$v_{(import)}$	"import" rate of amino acids (AminoH_)	2.367 $\mu M \mu m^{-2} min^{-1}$

Table 6: An exemplary set of fitted parameters for the protein degradation model. The parameters for the proton loss, the Ppase and the ATPase are found in the same range as for the core model. The export rate constant for amino acids was kept high, altering it could not decrease the amount of protein import needed to achieve a vacuolar acidification as observed in the experimental data. Unusual parameter units arise from the scaling with the vacuolar surface area, as described in chapter 3.

4.3.4 Hypothesis 3: Exchange of protons with vacuolar calcium ions

Motivation of the model

Most ions are transported into the vacuole through antiporters using the proton motive force across the tonoplast. In principle, a reversal of this transport is imaginable, transporting protons into the vacuole by releasing other ions. This process however is only feasible, if the ions to be transported by the antiporters have another way to be actively inserted into the vacuole, as otherwise a cross-membrane concentrational equilibrium would be reached quickly when there is no proton pump active. Only few compounds are known to be pumped into the

vacuole without the help of the proton motive force, among them is calcium, which can be pumped into the vacuole through a calcium pumping ATPase. As calcium is typically stored in both the ER and the vacuole in plants [150] [100], a transport of calcium through vesicles, possible through the TGN/EE, into the vacuole can be imagined, which has however to date not been proven. The calcium concentration gradient across the tonoplast is typically believed to be in the range of 1000 fold [151], providing a potentially powerful battery for proton pumping. And indeed, studies of CAX transporters in oat have provided ground for the assumtion of a potential reversal of the CAX1 and CAX2 calcium antiporters [152], for which a stoichiometry of 1 Ca^{2+} per 3 H^+ has been suggested [153].

To test the hypothesis, whether a calcium antiporter reversal could account for the rest acidification of the vacuole, the core model had to be altered mor significantly than for the other hypotheses.

Species and global quantities

Besides the cytosolic protons, the concentration of which is still fixed, and the vacuolar protons, the vacuolar 4-part buffer system was left unaltered from the core model. In addition, calcium ions were introduced both for the cytosol (Cacyt) and the vacuole (Cavac), the concentration of which was taken from literature [94] to be 200nM for Cacyt and 10mM for Cavac as initial values. Furthermore, a calcium buffer system was included for both the cytosol and the vacuole, since the free calcium concentration is typically 50-1000 fold smaller than the bound form of calcium [103]. Therefore, similar to the proton buffer system, a calcium buffer system for the cytosol and vacuole was modeled, with the cytosolic bound calcium 1000 fold than the free calcium, the ratio for which was adjusted to 50 for the vacuole, similar to values reported for the ER of several other cell types [102] [154], and the total buffer concentrations in the cytosol reaching 200μM and 10mM in the vacuole. Furthermore, the transmembrane voltage had to be included explicitly as a global quantity to test for

the possibility of reversal, as the antiporter works in a electrogenic manner, the reversal of which therefore being dependent on the membrane potential. The value of the membrane potential across the tonoplast is still under debate, however it is mostly reported to be around -35mV [110][111] [112]. As could be shown, the membrane voltage can be formulated as a simple linear function of the proton concentration difference across the membrane [113], which simplifies the model significantly as no anions or further cations have to be included. Hence, the membrane voltage was modeled phenomenologically using a linear term, in which the potential is -35mV in the wildtype situation and decreases linearly with the transmembrane pH difference. It reaches 0, when vacuolar and cytosolic pH are equal.

Reactions

The proton and calcium ATPases were formulated, as before, with voltage independent Michaelis-Menten kinetics, and the proton buffer kinetics were left unaltered. The calcium buffers were implemented using fast acting mass action kinetics for the cytosol and vacuole such that in the wildtype, the reported concentrations are reached. All other processes (proton loss, a calcium loss through a channel, calcium-proton antiporter) are modeled in a membrane potential-dependent way. A common formalism for membrane potential dependent kinetics is based on the Goldmann equation [155]. From this equation, one can deduce the flux J of an ion X with charge z as done for example in [127], leading to

$$J = Pz * \frac{F\Delta E}{RT} * \frac{[X]_{vac} - [X]_{cyt} * e^{-zF\Delta E/RT}}{e^{-zF\Delta E/RT} - 1} \tag{16}$$

with F, R, T being Faraday's constant, the universal gas constant and the temperature in Kelvin, respectively, P the membrane's permeability towards X, ΔE the potential difference and [X] the concentration of X.
However, the potential difference between vacuole and cytosol in this study

is assumed to be linearly dependent on the pH difference, which dissipates completely in the case of concanamycin A treatment without an active PPase. In that case, this equation is not applicable anymore. Therefore, the potential dependent processes are here formulated according to Nernst's equation, where the reaction velocity is proportional to the difference between the equilibrium potential of the involved species and the membrane potential:

$$\nu = g * (Vm - \frac{R*T}{F} * ln\frac{X_{\text{out}}}{X_{\text{in}}}) \tag{17}$$

ν being the reaction velocity, g the conductivity of the respective transporter, Vm the membrane potential, and X the respective molecular species.

Furthermore, an opening probability for the proton and calcium channels was modeled explicitly. For this, a two-state Boltzmann equation was used to model the distribution between open and closed channel states, similar to [156] and [157]:

$$C_{\text{o}} = \frac{1}{e^{x*\frac{zF}{R*T}*(Vm-Vh)}} \tag{18}$$

with C_{o} being the fraction of open channels, x the fractional difference of the energy barrier of the mebranes inner and outer surface, z the valence of the transported ion and Vh the voltage for half maximal activation. For a full derivation of this formula, consult appendix 2.3. Taken together, one arrives at a formulation for the calcium loss through the channel as:

$$J_{\text{Ca-channel}} = \frac{g}{1 + e^{x*\frac{F}{R*T}*(Vm-Vh)}} * (Vm - \frac{R*T}{F} * ln\frac{Ca_{\text{vac}}}{Ca_{\text{cyt}}}) \tag{19}$$

The equilibrium potential for the calcium-proton antiporter can be found by considering the above stated and the stoichiometry of 1 calcium ion per 3 protons, arriving at:

$$J_{\text{CAX}} = g * (Vm - \frac{R*T}{F} * ln\frac{H_{\text{vac}}^3 * Ca_{\text{cyt}}}{H_{\text{cyt}}^3 * Ca_{\text{vac}}}) \tag{20}$$

To test for the possibility that vesicles from the TGN/EE transport the antiporter constitutively to the vacuolar membrane, a simple additional process was included. Here, a species "vesicles" is multiplied with the expression of the kinetic rate law for the antiporter stated above. This "vesicles" species is initially set to a concentration of 1, meaning a fully functional antiporter. When, due to concanamycin A influence, the vesicular transport from TGN/EE to vacuole stops, the antiporter is assumed to slowly degrade and not be replenished, which is modeled by a simple degradation of the "vesicles" species. An overview over the newly formulated model can be found in figure 16.
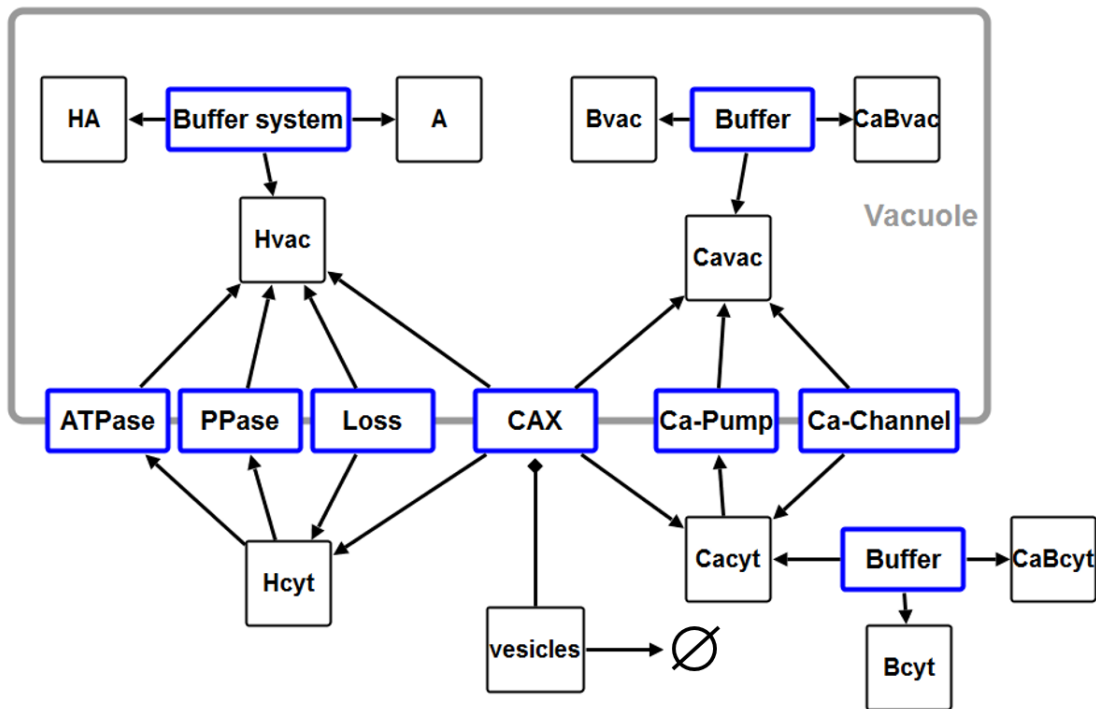
Figure 16: An overview over the calcium antiporter model. Reactions/enzymes are drawn in blue, species in back. The core model was modified to include calcium and its im-/export processes and a membrane potential, which influences the rates through Hloss and Ca-transporter. H = protons, Ca = calcium, A = deprotonized buffer component, HA = protonized buffer component, CAX = calcium-proton antiporter, B = Calcium buffer without calcium, CaB = Calcium buffer with calcium bound.

Fit and analysis of the model

The model's parameters were fitted to the vacuolar pH data of the wildtype/Col-0 (figure 8), the triple proton pump mutant (figure 8) and the concanamycin A time course data (figure 9). As before, the ATPase flux was restrained to only allow for realistic proton fluxes. For both the wildtype data and the triple proton pump mutant data, the "vesicle" process was set to 0, meaning no degradation of the "vesicle" species, the concentration of which remained at 1 and therefore the antiporter process remained fully active. In the triple proton pump mutant, both V-ATPase and PPase fluxes were set to 0, so the proton fluxes through the proton loss and the proposed proton import through the antiporter need to have a fixed ratio. For the time course data, the flux through the ATPase was set to 0 and the degradation rate of the "vesicles" process was left to be fitted. Any rate greater than 0 would eventually lead to the "vesicle" species to be depleted and eventually stop any flux through the antiporter, whereby only the PPase remains as an acidifying factor. Table 7 shows the parameter values for the best fit model. An overview over the best fit of the pH values can be found in figure 17, from where it becomes clear that the data is sufficiently well reproducable by the model.

Parameter name	Parameter description	Value
$g_{(loss)}$	conductivity of the proton loss process, adjusted for membrane surface and electrical current to represent particle flux	1.43E-18 $Sm^{-4}C^{-1}$
$V_{(ATPase)}$	maximal velocity of the proton pumping ATPase	2.52E-13 $\mu M min^{-1}$
$Km_{(ATPase)}$	Km of the proton pumping ATPase	0.01 μM
$V_{(PPase)}$	maximal velocity of the PPase	1.82E-14 $\mu M min^{-1}$
$Km_{(PPase)}$	Km of the PPase	0.01 μM
$g_{(CAX)}$	conductivity of the calcium-proton antiporter, adjusted for membrane surface and electrical current to represent particle flux	9.11E-12 $Sm^{-4}C^{-1}$
$V_{(Ca-Pump)}$	maximal velocity of the calcium pumping ATPase	5.20E-8 $\mu M min^{-1}$
$Km_{(Ca-Pump)}$	Km of the calcium pumping ATPase	0.001 M
$g_{(Ca-Channel)}$	conductivity of the calcium channel, adjusted for membrane surface and electrical current to represent particle flux	9.7e-10 $Sm^{-4}C^{-1}$
$x_{(Ca-Channel)}$	difference between fractional distances of the energy barrier between inside and outside the vacuole for the calcium channel	1.21
$Vh_{(Ca-Channel)}$	half maximal activation potential for the calcium channel	-0.02 V

Table 7: An exemplary set of fitted parameters for the calcium antiport model. in contrast to the models of the other hypotheses, the time course of the vacuolar pH under concanamycin treatment is not only determined by the proton loss and the PPase, but also by the calcium antiporter kinetics and, connected with this, the calcium pump and channel. Unusual parameter units arise from the scaling with the vacuolar surface area, as described in chapter 3.
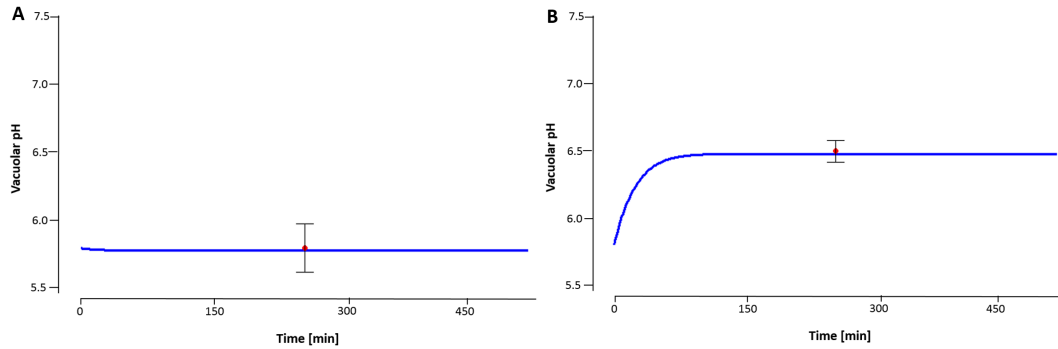
Figure 17: The fitted values of the vacuolar pH (blue curve) and the experimentally measured data (red point). Both the wildtype pH of 5.8 (A) and the triple mutant (B) can be fitted well.
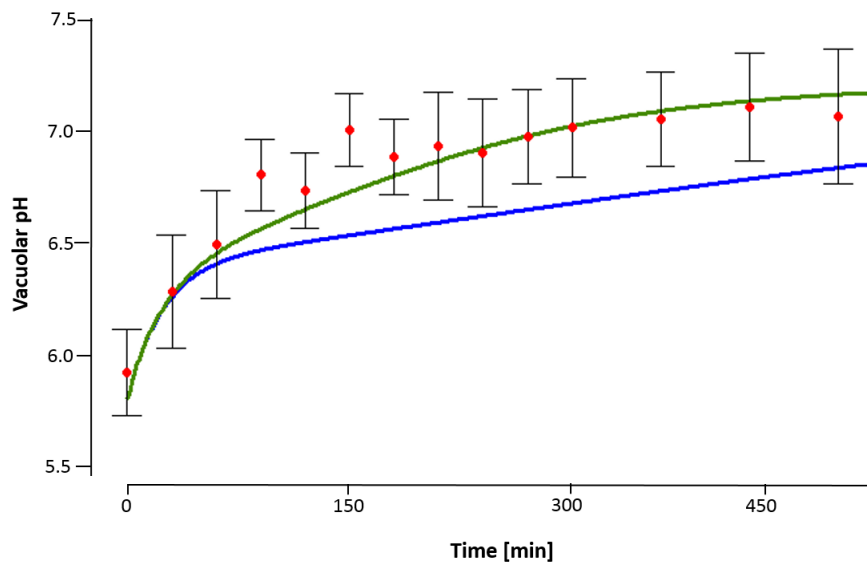
Figure 18: The fitted values of the vacuolar pH(blue and green curves) and the experimental data (red points) of the concanamycin A time course, in which only the PPase is active and the calcium-proton antiporter (CAX) degrades over time. A degradatio time of 87 minutes (green) describes the data better than a degradation time of 4 hours (blue).

The cytosolic and vacuolar calcium concentrations are not known for each of the experimental conditions, however it is important to check the predicted calcium concentrations under the simulated experimental conditions, as calcium acts as an important signalling molecule. In the triple mutant, where a reversal of calcium-proton antiport direction is proposed, cytosolic values of calcium should therefore not exceed wildtype values by too far, as typical values of around 800 nM are sufficient to trigger signalling responses. And indeed, predicted cytosolic calcium levels in the triple mutant decrease to about 80 nM, due to an increased flux through the calcium pump in these conditions which counteracts the outflux of calcium from the vacuole via the antiporter. Overall, the cytosolic calcium levels of 200 nM in the wildtype are rather slightly above the acceptable physiologic levels in the wildtype, as reported levels range from 50nM to 150nM [158].
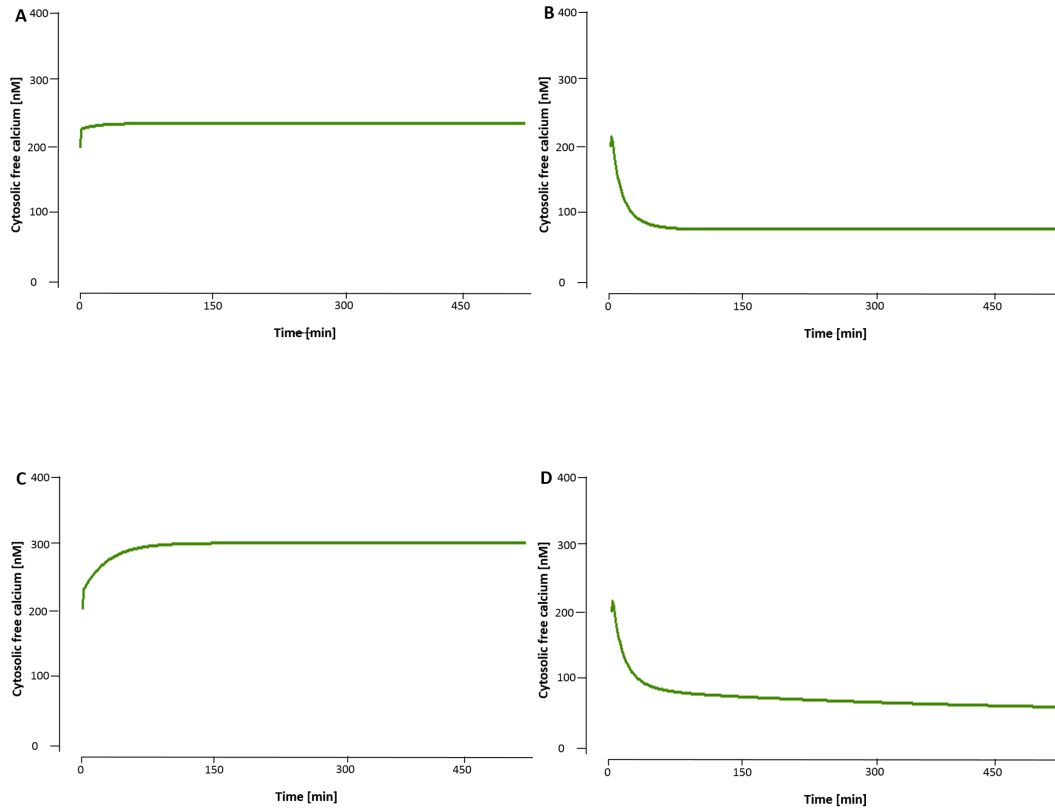
Figure 19: The cytosolic calcium concentration values predicted by the model with best fit parameters. In all cases, the calcium concentration lies within a physiologically acceptable range (A: wildtype, B: triple mutant, C: AP-1 KO, D: Concanamycin A time course).

It is interesting to note that the antiporter can switch its direction at a vacuolar pH of around 6.5, thereby leading to a slowdown of the loss process at that value, with the pH slowly approaching 7.2 as the antiporter degrades due to the "vesicles" process. This does not exactly reproduce the behavior observed experimentally, since in this case the slowdown seems to start at a pH of around 6.8, but given the standard deviation of the exeriment, the behavior produced by the model can be considered to be in the acceptable range. The magnitude of the eventual slowdown of the loss process is governed completely by the "vesicles" process. In the best fit, the degradation constant

of the "vesicles" species $k1_{"vesicles"}$ was found to be 0.008 min^{-1}. To calculate the half-life of the antiporter that this value represents, one can simply look at a mass-action degradation rate of a species "vesicles" (which serves as a proxy for the antiporter concentration) with kinetic constant 0.008 min^{-1}:

$$vesicles \rightarrow \varnothing \tag{21}$$

which leads to the differential equation

$$\frac{d[vesicles]}{dt} = -k1_{\text{vesicles}} * [vesicles](t) \tag{22}$$

which has the solution

$$[vesicles](t) = A_0 * e^{-k1_{\text{vesicles}}*t} \tag{23}$$

with A_0 being the initial concentration of "vesicles", which in this case is 1. With this, the half life $t_{1/2}$ is calculated:

$$0.5 = \frac{A_0}{2} = A_0 * e^{-k1_{\text{vesicles}}*t} = 1 * e^{-0.008min^{-1}*t} \tag{24}$$

leading to a half-life of about 87 min.

No information about the half-life of the calcium-proton antiporters (CAX antiporter family) has been published yet. In general however, plant proteins display a broad range of half-lifes from few hours to several months [159]. This means, the obtained half-life is rather too short to be sufficient to explain the data. Taking a half-life of around 4 h is more realistic, especially in the context of the root elongation zone, as an increase of vacuolar surface during this process can lead to an effective "dilution" of tonoplast proteins if there is no constant supply. This however would require a "vesicle" degradation rate constant of 0.003. This is plotted in figure 18 too, and this results in a slightly too slow increase of vacuolar pH.

To further assess the feasibility of this proposed hypothesis, the fitted model was used to simulate the knockout of AP-1 vesicles, that are the candidate for the delivery of the calcium-proton antiporter. To do this, the flux through the antiporter process was set to 0 with all other processes staying unaltered. And indeed, as shown in figure 20, the vacuolar pH decreases to around 5.65, close to the measured value in defective AP-1 strains (hap13; figure 10).
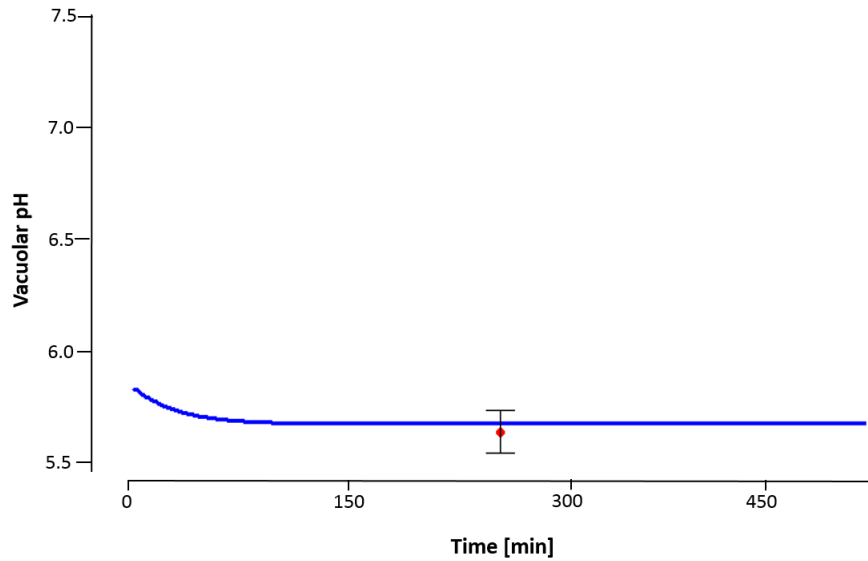
Figure 20: The predicted vacuolar pH (blue curve) and the experimental data (red point) for the AP-1 KO. The flux through the calcium-proton antiporter (CAX) was set to 0 to simulate it being transported through AP-1 vesicles.

Parameter space

In the case of this model, the possible parametrizations of the model vary more widely than in the previous cases. This is due to the contribution of the calcium module to both acidification in the triple mutant case and to the proton loss under wildtype conditions. The kinetic parameters for the proton pumping V-ATPase were still restricted in a range that leaves realistic amounts of protons pumped through them, as described in the core model. If one looks only at the parametrizations that lead to realistic calcium concentrations in cytosol and vacuole as well as are able to produce a model behavior similar to the dataset

from AP-1 KO strains (figure 10 *hap13*; assume calcium antiporter inactive), the parameter space is more heavily restrained. The parameters for the calcium channel are more widely variable, especially the parameteres $x_{(Ca-Channel)}$ and $Vh_{(Ca-Channel)}$, describing the difference of the fractional distance of inner and outer tonoplast energy barrier of the calcium channel transport and its half maximal activation potential, respectively. The reason for this becomes clear when looking at the rate law, as both parameters enter the rate law only as exponents to an opening probability scaling factor in the denominator for the conductivity g, which eventually determines the model's behavior. The model can describe the data reasonably well even without the additional scaling factor, which takes a value close to 0 for strongly negative values of $x_{(Ca-Channel)}$, which are unphysical, or values of $Vh_{(Ca-Channel)}$ far more positive than -0.035V, which are unphysiological. The scaling factor takes a value of 1 for $x_{(Ca-Channel)} = 0$ or $Vh_{(Ca-Channel)} = $ -0.035V, which means a half maximal activation of the channel. If the scaling factor becomes very high, which happens for high values of $x_{(Ca-Channel)}$ and values of $Vh_{(Ca-Channel)}$ far more negative than -0.035V, the calcium channel effectively stops any activity and the calcium antiporter must take the role as calcium outflux even in the wildtype case. This does not correspond to the above mentioned behavior of the system, for which reason the parameter values are restricted in those directions. The other calcium channel parameter, $g_{(Ca-Channel)}$ can vary to some degree, if the calcium pump parameters are adjusted accordingly, leading to a higher overall variablility than for the parameters of the proton transporting processes, which have been restricted by the proton pumping V-ATPase. The calcium pump needs to have a comparably high activity for the model to reproduce the behavior observed experimentally. This could be due to the fact that in reality, calcium is imported not only by the pump, but also by antiporters. Since only one antiporter has been implemented in this model, a directional reversal of this means that the only calcium import left is by the calcium pump, which subsequently needs to be strong enough to counteract the vacuolar calcium loss through both the calcium channel and antiporter. An overview over

the possible parameter ranges that create both realistic calcium levels and a realistic response to calcium antiporter inactivation is given in figure 21.
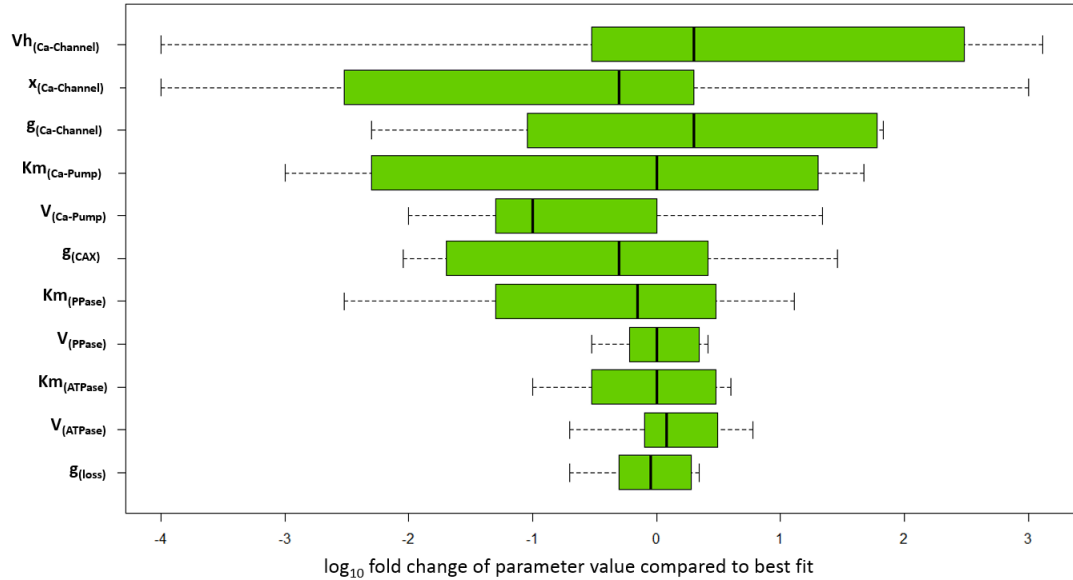
Figure 21: The possible fold changes of the parameter values compared to the best fit result, that still produce model parametrizations that describe the data well. The possible flux through the proton pumping ATPase has been restricted as described in the text, and limits for $x_{(Ca-Channel)}$ and $Vh_{(Ca-Channel)}$ have been set to about 0.0001 to 1000-fold their best fit values. The parameters were obtained from 50 fits using the genetic algorithm as described in the text.

The most pronounced impact on the model's behavior is given by the Vmax parameters for both the V-ATPase (for proton concentrations) and the Ca-Pump (for cytosolic calcium concentrations, negative sensitivity). This makes sense biologically, as those processes are the only ones using ATP-stored energy directly and thereby powering the system. As a counterweight to those processes, the Ca-channel and proton loss systems harbour some control over the respective ion's concentrations, too. Interestingly, the CAX antiporter system does not influence the wildtype proton and calcium concentrations as significantly as could be expected by its central role in the explanation of the vacuolar rest acidification in the triple mutant.

Sensitivities

An understanding of the impact of each process on the overall pH homeostasis can be gained by means of sensitivity analysis. The scaled sensitivities of the vacuolar proton concentration as well as the cytosolic calcium concentration in the wildtype can be seen in table 8. The most pronounced impact on the model's behavior is given by the Vmax parameters for both the V-ATPase (for proton concentrations) and the Ca-Pump (for cytosolic calcium concentrations, negative sensitivity). This makes sense biologically, as those processes are the only ones using ATP-stored energy directly and thereby powering the system. As a counterweight to those processes, the Ca-channel and proton loss systems harbour some control over the respective ion's concentrations, too. Interestingly, the CAX antiporter system does not influence the wildtype proton and calcium concentrations as significantly as could be expected by its central role in the explanation of the vacuolar rest acidification in the triple mutant.

	[Hvac]	[Cacyt]
k1(HBuffer1)	1.29E-12	1.23E-12
k2(HBuffer1)	-1.41E-12	-1.01E-12
k1(HBuffer2)	1.24E-10	1.00E-10
k2(HBuffer2)	-1.24E-10	-1.00E-10
k1(HBuffer3)	5.30E-09	4.30E-09
k2(HBuffer3)	-5.31E-09	-4.31E-09
k1(HBuffer4)	1.02E-07	8.30E-08
k2(HBuffer4)	-1.02E-07	-8.31E-08
V(ATPase)	2.602400	0.750456
Km(ATPase)	-2.87E-05	-2.20E-05
V(PPase)	0.212775	0.061358
Km(PPase)	-2.34E-06	-1.80E-06
g(Loss)	-0.002145	-0.001643
z(Loss)	0.757564	0.580313
k1(CaBuffercyt)	-0.000150	-0.000242
k2(CaBuffercyt)	0.000151	0.000242
k1(CaBuffervac)	-0.078908	-0.126873
k2(CaBuffervac)	0.078906	0.126863
V(Ca-Pump)	-0.087644	0.858941
Km(Ca-Pump)	0.087183	-0.849245
g(CAX)	-0.000110	-0.000101
z(CAX)	0.052975	0.042998
g(Ca-Channel)	-0.004601	0.489867
x(Ca-Channel)	-0.024614	0.241150
Vh(Ca-Channel)	0.029002	-0.284140

Table 8: The scaled sensitivities of both vacuolar proton concentration ([Hvac]) and cytosolic calcium concentration ([Cacyt]). Green signifies a strongly positive influence and red a strongly negative one. The pumps exhibit by far the greatest influence on the respective ionic concentrations.

4.4 Discussion

Recent experiments showed that the current understanding of the processes involved in vacuolar pH homeostasis in *Arabidopsis thaliana* root cells is not complete. In mutants lacking any proton pumping activity through the two vacuolar V-ATPases and the vacuolar proton pumping PPase, the vacuole still exhibits an approximately 10-fold acidification of its lumen compared to the cytoplasm, and only if the TGN/EE-resident V-ATPase is simultaneously inhibited using concanamycin A, does the vacuolar pH reach cytosolic levels. In this work, I introduced several hypotheses to explain this phenomenon and implemented them in models consisting of a set of ordinary differential equations describing the change of the concentrations of the molecular species involved over time.

A direct import of protons into the vacuole through an as of yet unknown proton pump seems unlikely, as this would require a proton pumping activity of around 20% of the known vacuolar V-ATPases. This requires either a large amount of proton pumps with a similar activity to the known V-ATPases or a new type of proton pump with even higher activity. In both cases, the respective proton pumps would be expected to have been detected already, though a transfer of the TGN/EE-resident V-ATPase in large amounts can safely be ruled out as they could not be detected using microscopically. Similarly, a direct import of protons via TGN/EE derived vesicles is equally unlikely, as this would require a physiologically not feasible amount of vesicles being transported from TGN/EE to vacuole or a specific, strong acidification of them, for which there is no evidence.

A release of protons by vacuolar protein degradation has the potential to acidify the vacuole, however not to the extend observed in the triple mutants, as the whole plant proteome at a given timepoint would have to be degraded within just 20 hours.

Finally, the reversal of a calcium-proton antiporter in the tonoplast is able to reproduce the experimental data. In this model, the high concentration of cal-

cium in the vacuole compared to the cytosol is only possible to be maintained with a high enough pH gradient across the tonoplast. In the triple mutant however, this gradient is weakened and by this allows for a reversal of the antiporter direction, so that calcium from the vacuole is released with protons from the cytosol being taken up into the vacuole, effectively lowering the vacuolar pH. This is possible, as calcium has another way of reaching the vacuolar lumen, namely through a calcium pumping ATPase in the tonoplast, which leads to a stable system even in the triple mutant. In this model, the cytosolic calcium concentrations do not reach unphysiologically high levels even when the antiport reverses, with cytosolic calcium concentrations reaching a maximum of around 230 nM. This is slightly higher than the values reported in literature for steady state (50 - 200 nM), but still far from signalling values (above 800 nM). A reason for the slightly too high cytosolic calcium concentrations in the model could be found in the calcium buffer system, for which exact parameter values for *A. thaliana* vacuoles have not been published. Importantly, as calcium is an important signalling molecule, one can expect a tight regulation of the processes involved in calcium homeostasis. Calcineurin has been shown to be an important regulator for calcium-proton antiporters in a variety of species, and the calcium pump ACA1 is activated by calmodulin [160]. Those feedbacks can well be relevant in the further development of the model and could prove to be essential for attaining lower and thereby more physiological values for cytosolic calcium levels.

The model has the ability to describe the present data well and was able to correctly predict the effect of defective AP-1 vesicle phenotypes when assuming the antiporter CAX to be transported by them and degraded quickly. However, the degradation rate necessary to achieve a good fit of the concanamycin A time course data is higher than physiologically expected. For the future model development, this could possibly be corrected if one assumes not (only) the antiporter to be transported, but also regulator molecules such as calmodulin or potentially calcium itself. The case of a direct vesicular transport of calcium through TGN/EE derived vesicles has the advantage over the direct transport

of protons as described above, that for one calcium ion, three protons can be imported, thereby requiring a lower calcium concentration in the vesicles. Furthermore, calcium-binding molecules are well known and would therefore provide a plausible mechanism for local accumulation in vesicles, contrary to protons.

Furthermore, in many systems, a close interaction of calcium signalling and cellular pH has been observed, with propositions of a tight coupling of both and the pH itself as a cellular signal, with the significant molecular players enabling this connection still unknown [100] [161]. On this line of thought, this model could provide one of those connections, as the concentration of protons and calcium on both sides of the vacuolar membrane communicate through the modeled antiporter system.

In terms of explanatory power, this study can not rule out any process analyzed here to contribute to the vacuolar pH-homeostasis. It is well possible that a combination of the mentioned processes or other, unknown mechanisms are eventually responsible for the observed experimental data. Especially in the case of the reversal of the direction of the calcium antiporter, one could imagine a range of other possible processes to be responsible for the experimentally observed phenomena. Instead of a steady transport of the antiporter itself from TGN/EE to vacuole, the calcium pump could be transported. That would mean, that only if the calcium pump stops being transported to the vacuole when vesicular flux stops due to concanamycin A treatment, the vacuolar calcium levels could drop enough to make a reversal of the antiporter impossible.

On the same line of thought, calcium itself could be transported through the vesicles. This could be possible, as the ER is, together with the vacuole itself, a main storage compartment for calcium in plants. It is easy to imagine the TGN/EE, as an intermediate compartment between ER and vacuole, to harbour significant levels of calcium, too. In contrast to the hypothesis of a direct proton transport from TGN/EE to vacuole, a direct calcium transport would have two advantages: first, there is a host of calcium binding proteins

90

in the cell, and therefore a specific mechanism of directed calcium transport and release in the vacuole is easier to imagine than for protons, given the only small pH difference between the two compartments. And second, calcium can be exchanged with protons through the antiporter with a stoichiometric ratio of 3 to 1, meaning less calcium would be required than proton in steady state to maintain the given pH gradient across the tonoplast.

A direct transport of the calcium channel can not be able to describe the data, as that would only lead to higher vacuolar calcium levels, meaning, as a tendency, rather more calcium efflux through the antiporter and by doing so, still acidifying the vacuole.

For future model developments, it will be interesting to analyze the role of ATP in more detail. As the tonoplast-resident V-ATPases are major ATP consumers in the cell, so a deletion of those consumers can increase the cellular ATP levels (according to unpublished data by Melanie Krebs, *vha-a1/a2* mutants contain around 50% higher ATP levels). A higher level of ATP in the *vha-a1/a2* mutants could raise the activity of the calcium pumping ATPase. That could in turn lead to a situation-specific shift in calcium pumping responsibility from the antiporters (in the wildtype) to the calcium pump (in the mutant). That would also allow for a weaker wildtype activity of the calcium pump pump in the model, with a higher antiport activity. Overall, it is possible that this could lead to a better reproduction of physiological calcium levels by the model, and as a result, the neccessary degradation rate of the antiporter could possibly be decreased in the model, leading to a more realistic value. Even more so, comparing the changes of ATP levels in the different experimental conditions might help to explain the discrepancy between the pH value when the reversal of the antiporter happens could be explained: In the triple mutant, the vacuolar rest acidification is found to be at around pH 6.5, while the marked slowdown of the proton loss during the concanamycin A timecourse occurs at a pH of around 6.8, indicating a reversal of the antiporter direction around that pH value. In contrast to the triple mutant case, the ATP levels in the concanamycin A treated cells can not be high from the very beginning, as the

V-ATPases were still working until the application of the drug. That means in turn, that the assumed higher calcium pump activity due to higher ATP levels would occur only when the cell had the time to create a high-enough ATP level. Therefore, vacuolar calcium levels could in this case initially be lower than in the triple mutant, leading to a higher vacuolar pH at which the antiport reversal occurs. This, of course, would need further experimental support, possibly with measurements of vacuolar calcium levels under the given conditions, to be acceptable as a valid mechanism.

Also, the exact value and dynamic behavior of the vacuolar membrane potential is certainly another important factor in this model. Measurements of its dynamics could help the model to be more accurately describing the charge fluxes across the tonoplast and possibly already resolve the remaining issues of the model as stated in the results section.

In conclusion, this work could demonstrate a potential explanation for the observed data by assuming a reversal of calcium antiporter direction. Further validation of the model, beyond the correct prediction of the effect of AP-1 vesicle inhibition, could be provided by the aforementioned expansion of the model on calcium signalling processes and the prediction of mutant effects on it as well as in its current state by measurements of both vacuolar and cytosolic calcium levels under the stated conditions. Overall, this model can serve as a poweful tool for exploring calcium-proton signalling interactions *in silico* and can thereby help in the understanding of a wide variety of dependent processes in plant cells.

Acknowledgement

References

[1] Kitano, H.: Computational systems biology. Nature **420**(6912), 206 (2002)

[2] Wolkenhauer, O.: Systems biology: The reincarnation of systems theory applied in biology? Briefings in bioinformatics **2**(3), 258–270 (2001)

[3] Ideker, T., Galitski, T., Hood, L.: A new approach to decoding life: systems biology. Annual review of genomics and human genetics **2**(1), 343–372 (2001)

[4] Emmert-Streib, F., Dehmer, M.: Networks for systems biology: conceptual connection of data and function. IET systems biology **5**(3), 185–207 (2011)

[5] Oberhardt, M.A., Palsson, B.Ø., Papin, J.A.: Applications of genome-scale metabolic reconstructions. Molecular systems biology **5**(1) (2009)

[6] Resat, H., Petzold, L., Pettigrew, M.F.: Kinetic modeling of biological systems. In: Computational Systems Biology, pp. 311–335. Springer, ??? (2009)

[7] Liebermeister, W., Klipp, E.: Bringing metabolic networks to life: Convenience rate law and thermodynamic constraints. Theoretical Biology and Medical Modelling **3**, 41 (2006). doi:**10.1186/1742-4682-3-41**

[8] Lillacci, G., Khammash, M.: Parameter estimation and model selection in computational biology. PLoS computational biology **6**(3), 1000696 (2010)

[9] Chis, O.-T., Banga, J.R., Balsa-Canto, E.: Structural identifiability of systems biology models: a critical comparison of methods. PloS one **6**(11), 27755 (2011)

[10] Kitano, H.: Systems biology: a brief overview. science **295**(5560), 1662–1664 (2002)

[11] Bruggeman, F.J., Westerhoff, H.V.: The nature of systems biology. TRENDS in Microbiology **15**(1), 45–50 (2007)

[12] Heazlewood, J.L.: The green proteome: challenges in plant proteomics. Frontiers in plant science **2**, 6 (2011)

[13] Van Norman, J.M., Benfey, P.N.: Arabidopsis thaliana as a model organism in systems biology. Wiley Interdisciplinary Reviews: Systems Biology and Medicine **1**(3), 372–379 (2009)

[14] Tsesmetzis, N., Couchman, M., Higgins, J., Smith, A., Doonan, J.H., Seifert, G.J., Schmidt, E.E., Vastrik, I., Birney, E., Wu, G., *et al.*: Arabidopsis reactome: a foundation knowledgebase for plant systems biology. The Plant cell **20**(6), 1426–1436 (2008)

[15] Laibach, F.: Arabidopsis thaliana (l.) heynh. als objekt für genetische und entwicklungsphysiologische untersuchungen. Bot. Archiv **44**, 439–455 (1943)

[16] Reinholz, E.: Auslösung von röntgen-mutationen bei arabidopsis thaliana l. heynh. und ihre bedeutung für die pflanzenzüchtung und evolutionstheorie: Nebst zusammenfassg. PhD thesis, Verlag nicht ermittelbar (1945)

[17] Rédei, G.P.: Arabidopsis as a genetic tool. Annual review of genetics **9**(1), 111–127 (1975)

[18] Steinitz-Sears, L.M.: Chromosome studies in arabidopsis thaliana. Genetics **48**(4), 483 (1963)

[19] Pruitt, R.E., Meyerowitz, E.M.: Characterization of the genome of arabidopsis thaliana. Journal of molecular biology **187**(2), 169–183 (1986)

[20] Initiative, A.G., *et al.*: Analysis of the genome sequence of the flowering plant arabidopsis thaliana. nature **408**(6814), 796 (2000)

[21] Collins, F.S., Morgan, M., Patrinos, A.: The human genome project: lessons from large-scale biology. Science **300**(5617), 286–290 (2003)

[22] Hübner, K., Sahle, S., Kummer, U.: Applications and trends in systems biology in biochemistry. The FEBS journal **278**(16), 2767–2857 (2011)

[23] Ashyraliyev, M., Fomekong-Nanfack, Y., Kaandorp, J.A., Blom, J.G.: Systems biology: parameter estimation for biochemical models. The FEBS journal **276**(4), 886–902 (2009)

[24] Angeli, D., Ferrell, J.E., Sontag, E.D.: Detection of multistability, bifurcations, and hysteresis in a large class of biological positive-feedback systems. Proceedings of the National Academy of Sciences **101**(7), 1822–1827 (2004)

[25] Fell, D.A.: Metabolic control analysis: a survey of its theoretical and experimental development. Biochemical Journal **286**(Pt 2), 313 (1992)

[26] Jablonsky, J., Bauwe, H., Wolkenhauer, O.: Modeling the calvin-benson cycle. BMC Systems Biology **5**(1), 185 (2011)

[27] Rios-Estepa, R., Lange, B.M.: Experimental and mathematical approaches to modeling plant metabolic networks. Phytochemistry **68**(16-18), 2351–2374 (2007)

[28] Matuszyńska, A., Heidari, S., Jahns, P., Ebenhoeh, O.: A mathematical model of non-photochemical quenching to study short-term light memory in plants. Biochimica et Biophysica Acta (BBA)-Bioenergetics **1857**(12), 1860–1869 (2016)

[29] Henkel, S., Nägele, T., Hörmiller, I., Sauter, T., Sawodny, O., Ederer, M., Heyer, A.G.: A systems biology approach to analyse leaf carbohydrate

metabolism in arabidopsis thaliana. EURASIP Journal on Bioinformatics and Systems Biology **2011**(1), 2 (2011)

[30] GIOVANELLI, J., MUDD, S.H., DATKO, A.H.: Sulfur amino acids in plants. In: Amino Acids and Derivatives, pp. 453–505. Elsevier, ??? (1980)

[31] Eaton, S.V.: Effects of sulfur deficiency on growth and metabolism of tomato. Botanical Gazette **112**(3), 300–307 (1951)

[32] Feldman-Salit, A., Veith, N., Wirtz, M., Hell, R., Kummer, U.: Distribution of control in the sulfur assimilation in arabidopsis thaliana depends on environmental conditions. New Phytologist (2019)

[33] Kobayashi, T., Nozoye, T., Nishizawa, N.K.: Iron transport and its regulation in plants. Free Radical Biology and Medicine **133**, 11–20 (2019)

[34] Koryachko, A., Matthiadis, A., Haque, S., Muhammad, D., Ducoste, J.J., Tuck, J.M., Long, T.A., Williams, C.M.: Dynamic modelling of the iron deficiency modulated transcriptome response in arabidopsis thaliana roots. in silico Plants **1**(1), 005 (2019)

[35] Nägele, T., Heyer, A.G.: Approximating subcellular organisation of carbohydrate metabolism during cold acclimation in different natural accessions of arabidopsis thaliana. New Phytologist **198**(3), 777–787 (2013)

[36] Hartmann, T.: Plant-derived secondary metabolites as defensive chemicals in herbivorous insects: a case study in chemical ecology. Planta **219**(1), 1–4 (2004)

[37] Wink, M.: Plant breeding: importance of plant secondary metabolites for protection against pathogens and herbivores. Theoretical and applied genetics **75**(2), 225–233 (1988)

[38] Verpoorte, R.: Exploration of nature's chemodiversity: the role of secondary metabolites as leads in drug development. Drug Discovery Today **3**(5), 232–238 (1998)

[39] Knoke, B., Textor, S., Gershenzon, J., Schuster, S.: Mathematical modelling of aliphatic glucosinolate chain length distribution in arabidopsis thaliana leaves. Phytochemistry reviews **8**(1), 39 (2009)

[40] Olsen, K.M., Slimestad, R., Lea, U.S., Brede, C., LØVDAL, T., Ruoff, P., Verheul, M., Lillo, C.: Temperature and nitrogen effects on regulators and products of the flavonoid pathway: experimental and kinetic model studies. Plant, Cell & Environment **32**(3), 286–299 (2009)

[41] Santner, A., Estelle, M.: Recent advances and emerging trends in plant hormone signalling. Nature **459**(7250), 1071 (2009)

[42] Aldridge, B.B., Burke, J.M., Lauffenburger, D.A., Sorger, P.K.: Physicochemical modelling of cell signalling pathways. Nature cell biology **8**(11), 1195 (2006)

[43] Aloni, R., Aloni, E., Langhans, M., Ullrich, C.: Role of cytokinin and auxin in shaping root architecture: regulating vascular differentiation, lateral root initiation, root apical dominance and root gravitropism. Annals of botany **97**(5), 883–893 (2006)

[44] Moubayidin, L., Di Mambro, R., Sabatini, S.: Cytokinin–auxin crosstalk. Trends in plant science **14**(10), 557–562 (2009)

[45] Muraro, D., Byrne, H., King, J., Voß, U., Kieber, J., Bennett, M.: The influence of cytokinin–auxin cross-regulation on cell-fate determination in arabidopsis thaliana root development. Journal of theoretical biology **283**(1), 152–167 (2011)

[46] Vernoux, T., Brunoud, G., Farcot, E., Morin, V., Van den Daele, H., Legrand, J., Oliva, M., Das, P., Larrieu, A., Wells, D., *et al.*: The auxin

signalling network translates dynamic input into robust patterning at the shoot apex. Molecular systems biology **7**(1), 508 (2011)

[47] Pokhilko, A., Mas, P., Millar, A.J.: Modelling the widespread effects of toc1 signalling on the plant circadian clock and its outputs. BMC systems biology **7**(1), 23 (2013)

[48] Yilmaz, L.S., Walhout, A.J.: Metabolic network modeling with model organisms. Current opinion in chemical biology **36**, 32–39 (2017)

[49] Benedict, M.N., Mundy, M.B., Henry, C.S., Chia, N., Price, N.D.: Likelihood-based gene annotations for gap filling and quality assessment in genome-scale metabolic models. PLoS computational biology **10**(10), 1003882 (2014)

[50] Orth, J.D., Thiele, I., Palsson, B.Ø.: What is flux balance analysis? Nature biotechnology **28**(3), 245 (2010)

[51] Poolman, M.G., Miguet, L., Sweetlove, L.J., Fell, D.A.: A genome-scale metabolic model of arabidopsis and some of its properties. Plant physiology **151**(3), 1570–1581 (2009)

[52] de Oliveira Dal'Molin, C.G., Quek, L.-E., Palfreyman, R.W., Brumbley, S.M., Nielsen, L.K.: Aragem, a genome-scale reconstruction of the primary metabolic network in arabidopsis. Plant physiology **152**(2), 579–589 (2010)

[53] Williams, T.C., Poolman, M.G., Howden, A.J., Schwarzlander, M., Fell, D.A., Ratcliffe, R.G., Sweetlove, L.J.: A genome-scale metabolic model accurately predicts fluxes in central carbon metabolism under stress conditions. Plant physiology **154**(1), 311–323 (2010)

[54] Cheung, C.M., Poolman, M.G., Fell, D.A., Ratcliffe, R.G., Sweetlove, L.J.: A diel flux balance model captures interactions between light and

dark metabolism during day-night cycles in c3 and crassulacean acid metabolism leaves. Plant Physiology **165**(2), 917–929 (2014)

[55] Shaw, R., Cheung, C.: A dynamic multi-tissue flux balance model captures carbon and nitrogen metabolism and optimal resource partitioning during arabidopsis growth. Frontiers in plant science **9**, 884 (2018)

[56] Gianchandani, E.P., Chavali, A.K., Papin, J.A.: The application of flux balance analysis in systems biology. Wiley Interdisciplinary Reviews: Systems Biology and Medicine **2**(3), 372–382 (2010)

[57] Mintz-Oron, S., Meir, S., Malitsky, S., Ruppin, E., Aharoni, A., Shlomi, T.: Reconstruction of arabidopsis metabolic network models accounting for subcellular compartmentalization and tissue-specificity. Proceedings of the National Academy of Sciences **109**(1), 339–344 (2012)

[58] Hübner, K., Sahle, S., Kummer, U.: Applications and trends in systems biology in biochemistry. The FEBS journal **278**(16), 2767–2857 (2011)

[59] Hucka, M., Finney, A., Sauro, H.M., Bolouri, H., Doyle, J.C., Kitano, H., Arkin, A.P., Bornstein, B.J., Bray, D., Cornish-Bowden, A., *et al.*: The systems biology markup language (sbml): a medium for representation and exchange of biochemical network models. Bioinformatics **19**(4), 524–531 (2003)

[60] Li, W., Cowley, A., Uludag, M., Gur, T., McWilliam, H., Squizzato, S., Park, Y.M., Buso, N., Lopez, R.: The embl-ebi bioinformatics web and programmatic tools framework. Nucleic acids research **43**(W1), 580–584 (2015)

[61] Fisher, W.G., Yang, P.-C., Medikonduri, R.K., Jafri, M.S.: Nfat and nfκb activation in t lymphocytes: a model of differential activation of gene expression. Annals of biomedical engineering **34**(11), 1712–1728 (2006)

[62] Zi, Z., Feng, Z., Chapnick, D.A., Dahl, M., Deng, D., Klipp, E., Moustakas, A., Liu, X.: Quantitative analysis of transient and sustained transforming growth factor-β signaling dynamics. Molecular systems biology **7**(1), 492 (2011). doi:10.1038/msb.2011.22

[63] Hoops, S., Sahle, S., Gauges, R., Lee, C., Pahle, J., Simus, N., Singhal, M., Xu, L., Mendes, P., Kummer, U.: Copasi—a complex pathway simulator. Bioinformatics **22**(24), 3067–3074 (2006)

[64] Zhang, C., Hicks, G.R., Raikhel, N.V.: Plant vacuole morphology and vacuolar trafficking. Frontiers in plant science **5**, 476 (2014)

[65] Gupta, S., Marcel, N., Sarin, A., Shivashankar, G.: Role of actin dependent nuclear deformation in regulating early gene expression. PLoS One **7**(12), 53031 (2012)

[66] Dey, P.: Cancer nucleus: morphology and beyond. Diagnostic cytopathology **38**(5), 382–390 (2010)

[67] Baker, R.E., Gaffney, E., Maini, P.: Partial differential equations for self-organization in cellular and developmental biology. Nonlinearity **21**(11), 251 (2008)

[68] Meyers, J., Craig, J., Odde, D.J.: Potential for control of signaling pathways via cell size and shape. Current biology **16**(17), 1685–1693 (2006)

[69] Matile, P.: Biochemistry and function of vacuoles. Annual Review of Plant Physiology **29**(1), 193–213 (1978)

[70] Marty, F.: Plant vacuoles. The Plant Cell **11**(4), 587–599 (1999)

[71] Rogers, J.C.: Compartmentation of plant cell proteins in separate lytic and protein storage vacuoles. Journal of plant physiology **152**(6), 653–658 (1998)

[72] Viotti, C., Bubeck, J., Stierhof, Y.-D., Krebs, M., Langhans, M., van den Berg, W., van Dongen, W., Richter, S., Geldner, N., Takano, J., *et al.*: Endocytic and secretory traffic in arabidopsis merge in the trans-golgi network/early endosome, an independent and highly dynamic organelle. The Plant Cell **22**(4), 1344–1357 (2010)

[73] Herman, E., Schmidt, M.: Endoplasmic reticulum to vacuole trafficking of endoplasmic reticulum bodies provides an alternate pathway for protein transfer to the vacuole. Plant Physiology **136**(3), 3440–3446 (2004)

[74] Stamnes, M.A., Rothman, J.E.: The binding of ap-1 clathrin adaptor particles to golgi membranes requires adp-ribosylation factor, a small gtp-binding protein. Cell **73**(5), 999–1005 (1993)

[75] Loerke, D., Mettlen, M., Yarar, D., Jaqaman, K., Jaqaman, H., Danuser, G., Schmid, S.L.: Cargo and dynamin regulate clathrin-coated pit maturation. PLoS biology **7**(3), 1000057 (2009)

[76] Surpin, M., Raikhel, N.: Traffic jams affect plant development and signal transduction. Nature Reviews Molecular Cell Biology **5**(2), 100 (2004)

[77] Bassham, D.C., Raikhel, N.V.: Unique features of the plant vacuolar sorting machinery. Current opinion in cell biology **12**(4), 491–495 (2000)

[78] Martinoia, E., Maeshima, M., Neuhaus, H.E.: Vacuolar transporters and their essential role in plant metabolism. Journal of experimental botany **58**(1), 83–102 (2006)

[79] Martinoia, E., Massonneau, A., Frangne, N.: Transport processes of solutes across the vacuolar membrane of higher plants. Plant and Cell Physiology **41**(11), 1175–1186 (2000)

[80] Nelson, N., Perzov, N., Cohen, A., Hagai, K., Padler, V., Nelson, H.: The cellular biology of proton-motive force generation by v-atpases. Journal of Experimental Biology **203**(1), 89–95 (2000)

[81] Kriegel, A., Andrés, Z., Medzihradszky, A., Krüger, F., Scholl, S., Delang, S., Patir-Nebioglu, M.G., Gute, G., Yang, H., Murphy, A.S., *et al.*: Job sharing in the endomembrane system: vacuolar acidification requires the combined activity of v-atpase and v-ppase. The Plant Cell **27**(12), 3383–3396 (2015)

[82] Schumacher, K.: ph in the plant endomembrane system—an import and export business. Current opinion in plant biology **22**, 71–76 (2014)

[83] Reid, R.J., Smith, F.A.: The Cytoplasmic pH Stat. New York: Marcel Dekker, ??? (2002)

[84] Raven, J.A.: ph regulation in plants. Science Progress (1933-), 495–509 (1985)

[85] Madshus, I.H.: Regulation of intracellular ph in eukaryotic cells. Biochemical journal **250**(1), 1 (1988)

[86] Mostafavi, H., Thiyagarajan, S., Stratton, B.S., Karatekin, E., Warner, J.M., Rothman, J.E., O'Shaughnessy, B.: Entropic forces drive self-organization and membrane fusion by snare proteins. Proceedings of the National Academy of Sciences **114**(21), 5455–5460 (2017)

[87] Sharma, P.: Entropic force between membranes reexamined. Proceedings of the National Academy of Sciences **110**(6), 1976–1977 (2013)

[88] Luo, Y., Scholl, S., Doering, A., Zhang, Y., Irani, N.G., Di Rubbo, S., Neumetzler, L., Krishnamoorthy, P., Van Houtte, I., Mylle, E., *et al.*: V-atpase activity in the tgn/ee is required for exocytosis and recycling in arabidopsis. Nature plants **1**(7), 15094 (2015)

[89] Sakano, K.: Revision of biochemical ph-stat: involvement of alternative pathway metabolisms. Plant and Cell Physiology **39**(5), 467–473 (1998)

[90] Davies, D.: The fine control of cytosolic ph. Physiologia Plantarum **67**(4), 702–706 (1986)

[91] Rienmüller, F., Dreyer, I., Schönknecht, G., Schulz, A., Schumacher, K., Nagy, R., Martinoia, E., Marten, I., Hedrich, R.: Luminal and cytosolic ph feedback on proton pump activity and atp affinity of v-type atpase from arabidopsis. Journal of Biological Chemistry **287**(12), 8986–8993 (2012)

[92] Hunte, C., Screpanti, E., Venturi, M., Rimon, A., Padan, E., Michel, H.: Structure of a na+/h+ antiporter and insights into mechanism of action and regulation by ph. Nature **435**(7046), 1197 (2005)

[93] Barragán, V., Leidi, E.O., Andrés, Z., Rubio, L., De Luca, A., Fernández, J.A., Cubero, B., Pardo, J.M.: Ion exchangers nhx1 and nhx2 mediate active potassium uptake into vacuoles to regulate cell turgor and stomatal function in arabidopsis. The Plant Cell **24**(3), 1127–1142 (2012)

[94] Walker, D.J., Leigh, R.A., Miller, A.J.: Potassium homeostasis in vacuolate plant cells. Proceedings of the National Academy of Sciences **93**(19), 10510–10514 (1996)

[95] Gierth, M., Mäser, P.: Potassium transporters in plants–involvement in k+ acquisition, redistribution and homeostasis. FEBS letters **581**(12), 2348–2356 (2007)

[96] Bejger, M., Imiolczyk, B., Clavel, D., Gilski, M., Pajak, A., Marsolais, F., Jaskolski, M.: Na+/k+ exchange switches the catalytic apparatus of potassium-dependent plant l-asparaginase. Acta Crystallographica Section D: Biological Crystallography **70**(7), 1854–1872 (2014)

[97] Fuglsang, A.T., Paez-Valencia, J., Gaxiola, R.: Plant proton pumps: regulatory circuits involving h+-atpase and h+-ppase. In: Transporters and Pumps in Plant Signaling, pp. 39–64. Springer, ??? (2011)

[98] Yang, T., Poovaiah, B.: Hydrogen peroxide homeostasis: activation of plant catalase by calcium/calmodulin. Proceedings of the National Academy of Sciences **99**(6), 4097–4102 (2002)

104

[99] Roberts, D.M., Harmon, A.C.: Calcium-modulated proteins: targets of intracellular calcium signals in higher plants. Annual review of plant biology **43**(1), 375–414 (1992)

[100] Kader, M.A., Lindberg, S.: Cytosolic calcium and ph signaling in plants under salinity stress. Plant signaling & behavior **5**(3), 233–238 (2010)

[101] Knight, H.: Calcium signaling during abiotic stress in plants. In: International Review of Cytology vol. 195, pp. 269–324. Elsevier, ??? (1999)

[102] Mogami, H., Gardner, J., Gerasimenko, O.V., Camello, P., Petersen, O.H., Tepikin, A.V.: Calcium binding capacity of the cytosol and endoplasmic reticulum of mouse pancreatic acinar cells. The Journal of physiology **518**(2), 463–467 (1999)

[103] Brière, C., Xiong, T.C., Mazars, C., Ranjeva, R.: Autonomous regulation of free ca2+ concentrations in isolated plant cell nuclei: a mathematical analysis. Cell calcium **39**(4), 293–303 (2006)

[104] Vierstra, R.D.: Protein degradation in plants. Annual review of plant biology **44**(1), 385–410 (1993)

[105] Riens, B., Lohaus, G., Heineke, D., Heldt, H.W.: Amino acid and sucrose content determined in the cytosolic, chloroplastic, and vacuolar compartments and in the phloem sap of spinach leaves. Plant Physiology **97**(1), 227–233 (1991)

[106] Campbell, W.H.: Nitrate reductase and its role in nitrate assimilation in plants. Physiologia Plantarum **74**(1), 214–219 (1988)

[107] Wang, Y.-Y., Hsu, P.-K., Tsay, Y.-F.: Uptake, allocation and signaling of nitrate. Trends in plant science **17**(8), 458–467 (2012)

[108] Miller, A.J., Smith, S.J.: Cytosolic nitrate ion homeostasis: could it have a role in sensing nitrogen status? Annals of Botany **101**(4), 485–489 (2007)

[109] Tyerman, S.: Anion channels in plants. Annual review of plant biology **43**(1), 351–373 (1992)

[110] Wang, Y., Dindas, J., Rienmüller, F., Krebs, M., Waadt, R., Schumacher, K., Wu, W.-H., Hedrich, R., Roelfsema, M.R.G.: Cytosolic ca2+ signals enhance the vacuolar ion conductivity of bulging arabidopsis root hair cells. Molecular plant **8**(11), 1665–1674 (2015)

[111] Davis, R.F.: Electrical properties of the plasmalemma and tonoplast in valonia ventricosa. Plant physiology **67**(4), 825–831 (1981)

[112] Davies, J.: The bioenergetics of vacuolar h+ pumps. In: Advances in Botanical Research vol. 25, pp. 339–363. Elsevier, ??? (1997)

[113] Schuster, S., Ouhabi, R., Rigoulet, M., Mazat, J.-P.: Modelling the interrelation between the transmembrane potential and ph difference across membranes with electrogenic proton transport upon build-up of the proton-motive force. Bioelectrochemistry and bioenergetics **45**(2), 181–192 (1998)

[114] Petzold, L., Hindmarsh, A.: Lsoda (livermore solver of ordinary differential equations). Computing and Mathematics Research Division, Lawrence Livermore National Laboratory, Livermore, CA **24** (1997)

[115] Goldberg, D.E., Holland, J.H.: Genetic algorithms and machine learning. Machine learning **3**(2), 95–99 (1988)

[116] Eberhart, R., Kennedy, J.: A new optimizer using particle swarm theory. In: MHS'95. Proceedings of the Sixth International Symposium on Micro Machine and Human Science, pp. 39–43 (1995). Ieee

[117] Moser, I.: Hooke-jeeves revisited. In: 2009 IEEE Congress on Evolutionary Computation, pp. 2670–2676 (2009). IEEE

106

[118] Team, R.C.: R: A language and environment for statistical computing (version 3.4. 2)[computer software]. Vienna, Austria: R Foundation for Statistical Computing (2017)

[119] Wickam, H.: Tidyverse: Easily Install and Load the 'Tidyverse'. (2017). R package version 1.2.1. https://CRAN.R-project.org/package=tidyverse

[120] Arnold, J.B.: Ggthemes: Extra Themes, Scales and Geoms for 'ggplot2'. (2019). R package version 4.2.0. https://CRAN.R-project.org/package=ggthemes

[121] Junker, B.H., Klukas, C., Schreiber, F.: Vanted: a system for advanced data analysis and visualization in the context of biological networks. BMC bioinformatics **7**(1), 109 (2006)

[122] Krüger, F.: Vacuole biogenesis in arabidopsis thaliana. PhD thesis (2017)

[123] Scholl, S.: ph in the trans-golgi network/early endosome of arabidopsis thaliana: Suppliers and consumers. PhD thesis (2018)

[124] Gjetting, S.K., Ytting, C.K., Schulz, A., Fuglsang, A.T.: Live imaging of intra-and extracellular ph in plants using phusion, a novel genetically encoded biosensor. Journal of experimental botany **63**(8), 3207–3218 (2012)

[125] Liebermeister, W., Klipp, E.: Bringing metabolic networks to life: convenience rate law and thermodynamic constraints. Theoretical Biology and Medical Modelling **3**(1), 41 (2006)

[126] Alberty, R.A.: The relationship between michaelis constants, maximum velocities and the equilibrium constant for an enzyme-catalyzed reaction. Journal of the American Chemical Society **75**(8), 1928–1932 (1953)

[127] Andersen, A.Z., Carvalho, A.L., Neves, A.R., Santos, H., Kummer, U., Olsen, L.F.: The metabolic ph response in lactococcus lactis: an integra-

tive experimental and modelling approach. Computational biology and chemistry **33**(1), 71–83 (2009)

[128] Goldberg, R.N., Kishore, N., Lennen, R.M.: Thermodynamic quantities for the ionization reactions of buffers. Journal of physical and chemical reference data **31**(2), 231–370 (2002)

[129] Martinoia, E., Rentsch, D.: Malate compartmentation-responses to a complex metabolism. Annual review of plant biology **45**(1), 447–467 (1994)

[130] Lauer, M.J., Blevins, D.G., Sierzputowska-Gracz, H.: 31p-nuclear magnetic resonance determination of phosphate compartmentation in leaves of reproductive soybeans (glycine max l.) as affected by phosphate nutrition. Plant Physiology **89**(4), 1331–1336 (1989)

[131] MATSUURA-ENDO, C., MAESHIMA, M., YOSHIDA, S.: Subunit composition of vacuolar membrane h+-atpase from mung bean. European journal of biochemistry **187**(3), 745–751 (1990)

[132] Sze, H., Ward, J.M., Lai, S.: Vacuolar h+-translocating atpases from plants: structure, function, and isoforms. Journal of bioenergetics and biomembranes **24**(4), 371–381 (1992)

[133] Ratajczak, R.: Structure, function and regulation of the plant vacuolar h+-translocating atpase. Biochimica et Biophysica Acta (BBA)-Biomembranes **1465**(1-2), 17–36 (2000)

[134] Lüttge, U., Ratajczak, R.: The physiology, biochemistry and molecular biology of the plant vacuolar atpase. In: Advances in Botanical Research vol. 25, pp. 253–296. Elsevier, ??? (1997)

[135] Krebs, M., Beyhl, D., Görlich, E., Al-Rasheid, K.A., Marten, I., Stierhof, Y.-D., Hedrich, R., Schumacher, K.: Arabidopsis v-atpase activity at the tonoplast is required for efficient nutrient storage but not for sodium

accumulation. Proceedings of the National Academy of Sciences **107**(7), 3251–3256 (2010)

[136] Dhonukshe, P., Aniento, F., Hwang, I., Robinson, D.G., Mravec, J., Stierhof, Y.-D., Friml, J.: Clathrin-mediated constitutive endocytosis of pin auxin efflux carriers in arabidopsis. Current Biology **17**(6), 520–527 (2007)

[137] Royle, S.J.: The cellular functions of clathrin. Cellular and Molecular Life Sciences CMLS **63**(16), 1823–1832 (2006)

[138] Wu, X., Zhao, X., Baylor, L., Kaushal, S., Eisenberg, E., Greene, L.E.: Clathrin exchange during clathrin-mediated endocytosis. J Cell Biol **155**(2), 291–300 (2001)

[139] Staehelin, L.A., Moore, I.: The plant golgi apparatus: structure, functional organization and trafficking mechanisms. Annual review of plant biology **46**(1), 261–288 (1995)

[140] Yang, X., Liao, C.-Y., Tang, J., Bassham, D.C.: Overexpression of trans-golgi network t-snare s rescues vacuolar trafficking and tgn morphology defects in a putative tethering factor mutant. The Plant Journal (2019)

[141] Agmon, N.: The grotthuss mechanism. Chemical Physics Letters **244**(5-6), 456–462 (1995)

[142] Feraru, E., Paciorek, T., Feraru, M.I., Zwiewka, M., De Groodt, R., De Rycke, R., Kleine-Vehn, J., Friml, J.: The ap-3 β adaptin mediates the biogenesis and function of lytic vacuoles in arabidopsis. The Plant Cell **22**(8), 2812–2824 (2010)

[143] Hildebrandt, T.M., Nesi, A.N., Araújo, W.L., Braun, H.-P.: Amino acid catabolism in plants. Molecular plant **8**(11), 1563–1579 (2015)

[144] Liu, H., Zhang, R., Yao, X., Liu, M., Hu, Z., Fan, B.T.: Prediction of the isoelectric point of an amino acid based on ga-pls and svms. Journal of chemical information and computer sciences **44**(1), 161–167 (2004)

[145] Hasselbalch, K.A.: Die Berechnung der Wasserstoffzahl des Blutes aus der Freien und Gebundenen Kohlensäure Desselben, und die Sauerstoff-bindung des Blutes Als Funktion der Wasserstoffzahl. Julius Springer, ??? (1916)

[146] Henderson, L.J.: Concerning the relationship between the strength of acids and their capacity to preserve neutrality. American Journal of Physiology-Legacy Content **21**(2), 173–179 (1908)

[147] Tiessen, A., Pérez-Rodríguez, P., Delaye-Arredondo, L.J.: Mathematical modeling and comparison of protein size distribution in different plant, animal, fungal and microbial species reveals a negative correlation between protein size and protein number, thus providing insight into the evolution of proteomes. BMC research notes **5**(1), 85 (2012)

[148] Finka, A., Goloubinoff, P.: Proteomic data from human cell cultures refine mechanisms of chaperone-mediated protein homeostasis. Cell Stress and Chaperones **18**(5), 591–605 (2013)

[149] Ishihara, H., Obata, T., Sulpice, R., Fernie, A.R., Stitt, M.: Quantifying protein synthesis and degradation in arabidopsis by dynamic 13co2 labeling and analysis of enrichment in individual amino acids in their free pools and in protein. Plant Physiology **168**(1), 74–93 (2015)

[150] Patel, S., Docampo, R.: Acidic calcium stores open for business: expanding the potential for intracellular ca2+ signaling. Trends in cell biology **20**(5), 277–286 (2010)

[151] Taiz, L.: The plant vacuole. Journal of Experimental Biology **172**(1), 113–122 (1992)

[152] Schumaker, K.S., Sze, H.: Calcium transport into the vacuole of oat roots. characterization of h+/ca2+ exchange activity. Journal of Biological Chemistry **261**(26), 12172–12178 (1986)

[153] Pittman, J.K., Bonza, M.C., De Michelis, M.I.: Ca 2+ pumps and ca 2+ antiporters in plant development. In: Transporters and Pumps in Plant Signaling, pp. 133–161. Springer, ??? (2011)

[154] Zhou, Z., Neher, E.: Mobile and immobile calcium buffers in bovine adrenal chromaffin cells. The Journal of physiology **469**(1), 245–273 (1993)

[155] Goldman, D.E.: Potential, impedance, and rectification in membranes. The Journal of general physiology **27**(1), 37–60 (1943)

[156] Yifrach, O., MacKinnon, R.: Energetics of pore opening in a voltage-gated k+ channel. Cell **111**(2), 231–239 (2002)

[157] Kahm, M., Navarrete, C., Llopis-Torregrosa, V., Herrera, R., Barreto, L., Yenush, L., Ariño, J., Ramos, J., Kschischo, M.: Potassium starvation in yeast: mechanisms of homeostasis revealed by mathematical modeling. PLoS computational biology **8**(6), 1002548 (2012)

[158] Schroeder, J.I., Thuleau, P.: Ca2+ channels in higher plant cells. The Plant Cell **3**(6), 555 (1991)

[159] Li, L., Nelson, C.J., Trösch, J., Castleden, I., Huang, S., Millar, A.H.: Protein degradation rate in arabidopsis thaliana leaf growth and development. The Plant Cell **29**(2), 207–228 (2017)

[160] Shigaki, T., Hirschi, K.: Diverse functions and molecular properties emerging for cax cation/h+ exchangers in plants. Plant Biology **8**(04), 419–429 (2006)

[161] González, A., Pariente, J., Salido, G., Camello, P.: Intracellular ph and calcium signalling in rat pancreatic acinar cells. Pflügers Archiv **434**(5), 609–614 (1997)

Appendix A:
Area scaling in kinetic models of biological systems

A1 Model structures

A1.1 Toy model

Volume-scaled transport

$(X_{cyt} \leftrightarrow X_{vac})$

$$-\frac{X_{cyt}}{dt} = \frac{X_{vac}}{dt} = k * (V_{cyt} * X_{cyt} - V_{vac} * X_{vac}) \tag{25}$$

Area-scaled transport

$(X_{cyt} \leftrightarrow X_{vac})$

$$-\frac{X_{cyt}}{dt} = \frac{X_{vac}}{dt} = A_{vac} * k * (X_{cyt} - X_{vac}) \tag{26}$$

A1.2 NFAT model, altered reactions

Active Calcineurin transport

$(Act\_C_{cyt} \leftrightarrow Act\_C_{nuc})$

$$A_{nuc} * (k5 * Act\_C_{cyt} - k6 * Act\_C_{nuc}) \tag{27}$$

Inactive Calcineurin transport
$(Inact\_C_{cyt} \leftrightarrow Inact\_C_{nuc})$

$$A_{nuc} * (k5 * Inact\_C_{cyt} - k6 * Inact\_C_{nuc}) \tag{28}$$

Calcium transport
$(Ca_{cyt} \leftrightarrow Ca_{nuc})$

$$A_{nuc} * (k21 * Ca_{cyt} - k22 * Ca_{nuc}) \tag{29}$$

NFAT transport
$(NFAT_{cyt} \leftrightarrow NFAT_{nuc})$

$$A_{nuc} * (k17 * NFAT_{cyt} - k18 * NFAT_{nuc}) \tag{30}$$

Phosphorylated NFAT transport
$(NFAT\_Pi_{cyt} \leftrightarrow NFAT\_Pi_{nuc})$

$$A_{nuc} * (k3 * NFAT\_Pi_{cyt} - k4 * NFAT\_Pi_{nuc}) \tag{31}$$

NFAT Calcineurin complex transport

$(NFAT\_Act\_C_{cyt} \leftrightarrow NFAT\_Act\_C_{nuc})$

$$A_{nuc} * (k9 * NFAT\_Act\_C_{cyt} - k10 * NFAT\_Act\_C_{nuc}) \qquad (32)$$

Phosphorylated NFAT Calcineurin complex transport
$(NFAT\_Pi\_Act\_C_{cyt} \leftrightarrow NFAT\_Pi\_Act\_C_{nuc})$

$$A_{nuc} * (k7 * NFAT\_Pi\_Act\_C_{cyt} - k8 * NFAT\_Pi\_Act\_C_{nuc}) \qquad (33)$$

A1.3 TGFβ model, altered reactions

R1_Smad2_import

$(Smad2\_c- > Smad2\_n)$

$$A_{nuc} * k_{imp}\_Smad2c * Smad2c \tag{34}$$

R2_Smad2_export
$(Smad2\_n- > Smad2\_c)$

$$A_{nuc} * k_{exp}\_Smad2n * Smad2n \tag{35}$$

R3_Smad4_import
$(Smad4\_c- > Smad4\_n)$

$$A_{nuc} * k_{imp}\_Smad4c * Smad4c \tag{36}$$

R4_Smad4_export
$(Smad4\_n- > Smad4\_c)$

$$A_{nuc} * k_{exp}\_Smad4c * Smad4c \tag{37}$$

R24_Smads_Complex_import
$(Smads\_Complex\_c- > Smads\_Complex\_n)$

$$A_{nuc} * k_{imp}\_Smads\_Complex\_c * Smads\_Complex\_c \tag{38}$$

A2 Model parameters

A2.1 Toy model

Table A1:

Model structure	Parameter	Value
Volume-scaled, normal vacuole	k	$0.1s^{-1}$
	V_{cyt}	$2{,}000\mu m^3$
	V_{vac}	$18{,}000\mu m^3$
Area-scaled, normal vacuole	k	3.01234E-5$\mu m^2 * s^{-1}$
	V_{cyt}	$2{,}000\mu m^3$
	V_{vac}	$18{,}000\mu m^3$
	A_{vac}	$3{,}322\mu m^2$
Volume-scaled, reticulated vacuole	k	$0.1s^{-1}$
	V_{cyt}	$2{,}000\mu m^3$
	V_{vac}	$9{,}000\mu m^3$
Area-scaled, reticulated vacuole	k	3.01234E-5$\mu m^2 * s^{-1}$
	V_{cyt}	$2{,}000\mu m^3$
	V_{vac}	$9{,}000\mu m^3$
	A_{vac}	$6{,}644\mu m^2$

A2.2 NFAT signalling model

Table A2:

Model structure	Parameter	Value
Volume-scaled	k3	$0.005s^{-1}$
	k4	$0.5s^{-1}$
	k5	$0.0019s^{-1}$
	k6	$0.00092s^{-1}$
	k7	$0.005s^{-1}$
	k8	$0.5s^{-1}$
	k9	$0.5s^{-1}$
	k10	$0.005s^{-1}$
	k17	$0.0015s^{-1}$
	k18	$0.00096s^{-1}$
	k21	$0.21s^{-1}$
	k22	$0.5s^{-1}$
	V_{cyt}	2.69E-13L
	V_{vac}	1.13E-13L
Area-scaled	k3	1.19E-7
	k4	$5E\text{-}6\mu m * s^{-1}$
	k5	$4.552E\text{-}8\mu m * s^{-1}$
	k6	$9.2E\text{-}9\mu m * s^{-1}$
	k7	$1.19E\text{-}7\mu m * s^{-1}$
	k8	$5E\text{-}6\mu m * s^{-1}$
	k9	$1.19E\text{-}7\mu m * s^{-1}$
	k10	$5E\text{-}8\mu m * s^{-1}$
	k17	$3.57E\text{-}8\mu m * s^{-1}$
	k18	$9.6E\text{-}9\mu m * s^{-1}$
	k21	$5E\text{-}6\mu m * s^{-1}$
	k22	$5E\text{-}6\mu m * s^{-1}$
	V_{cyt}	2.69E-13L
	V_{vac}	1.13E-13L
	$A_{vac,min}$	$11.3\mu m^2$
	$A_{vac,max}$	$1130\mu m^2$

A2.3 TGFβ signalling model

Table A3:

Model structure	Parameter	Value
Volume-scaled	$K_{imp\_}Smad2_c$	$0.16s^{-1}$
	$K_{exp\_}Smad2_n$	$1s^{-1}$
	$K_{imp\_}Smad4_c$	$0.08s^{-1}$
	$K_{exp\_}Smad4_n$	$0.52s^{-1}$
	$K_{imp\_}Smads\_complex_c$	$0.16s^{-1}$
	$V_{cyt,min}$	1.15E-13L
	$V_{nuc,min}$	3.49E-14L
	$V_{cyt,max}$	1.725E-13L
	$V_{nuc,max}$	5.235E-13L
Area-scaled	$K_{imp\_}Smad2_c$	7E-3$dm * s^{-1}$
	$K_{exp\_}Smad2_n$	1.4583E-2$dm * s^{-1}$
	$K_{imp\_}Smad4_c$	3.5E-3$dm * s^{-1}$
	$K_{exp\_}Smad4_n$	7.2917E-3$dm * s^{-1}$
	$K_{imp\_}Smads\_complex_c$	7E-3$dm * s^{-1}$
	$V_{cyt,min}$	1.15E-13L
	$V_{nuc,min}$	3.49E-14L
	$A_{nuc,min}$	$2.4\mu m^2$
	$V_{cyt,max}$	1.725E-13L
	$V_{nuc,max}$	5.235E-13L
	$A_{nuc,max}$	$3.6\mu m^2$

A3 Scaled model sensitivities

A3.1 NFAT signalling model

Table A4:

Reaction	Parameter	scaled sensitivity of active nuclear NFAT
Calcineurin dep NFAT dephosphorylation	k1	2.18039E-7
Calcineurin dep NFAT dephosphorylation	k2	-0.00123037
Phosphorylated NFAT transport	k3	6.26247E-5
Phosphorylated NFAT transport	k4	-0.000269936
Calcineurin transport	k5	0.00311093
Calcineurin transport	k6	-0.00323382
Phosphorylated NFAT Calcineurin complex transport	k7	1.41609E-5
Phosphorylated NFAT Calcineurin complex transport	k8	-0.0013551
NFAT Calcineurin complex transport	k9	0.0131951
NFAT Calcineurin complex transport	k10	-0.010444
Phosphorylated NFAT Calcineurin complex disassembly	k11	0.00229174
Phosphorylated NFAT Calcineurin complex disassembly	k12	-0.000367357
NFAT Calcineurin complex phosphorylation	k13	0.00678753
NFAT Calcineurin complex phosphorylation	k14	-0.00802142
NFAT Calcineurin complex formation	k15	-0.0180615
NFAT Calcineurin complex formation	k16	0.0179093
NFAT transport	k17	7.49155E-5
NFAT transport	k18	-0.000505822
Calcineurin activation	k19	0.0103789
Calcineurin activation	k20	-0.0103879
Calcium transport	k21	0.0170185
Calcium transport	k22	-0.01706

A3.2 TGFβ signalling model

Table A5:

Reaction	Parameter	scaled sensitivity of nuclear SMAD complex
R1 Smad2 import	$K_{imp\_}Smad2_c$	-0.0666527
R2 Smad2 export	$K_{exp\_}Smad2_n$	0.0916061
R3 Smad4 import	$K_{imp\_}Smad4_c$	-0.0666877
R4 Smad4 export	$K_{exp\_}Smad4_n$	0.0819686
R5 T1R production	v_{T1R}	0.024528
R6/R12/R18 T1R/T2R/LRC Cave formation	ki_{Cave}	-0.340296
R7/R13/R19 T1R/T2R/LRC Cave recycling	kr_{Cave}	0.0842739
R8/R14/R20 T1R/T2R/LRC EE formation	ki_{EE}	0.302112
R9/R15/R21 T1R/T2R/LRC EE recycling	kr_{EE}	-0.130795
R10 T1R EE degradation	$kdeg_{T1R,EE}$	-0.00708498
R11 T2R production	v_{T2R}	0.129776
R16 T2R EE degradation	$kdeg_{T2R,EE}$	-0.0224511
R17 LRC formation	k_{LRC}	0.0242155
R22 LRC EE degradation	Kcd	-0.0550185
R23 Smads Complex formation	$k\_Smads\_complex_c$	0.486002
R24 Smads Complex import	$k_{imp\_}Smads\_complex_c$	0.198014
R25 Smads Complex Dissociation	$k_{diss\_}Smads\_complex_n$	-0.722791
R26 LRC Cave degradation	$Klid$	-0.00316132

Appendix B:
Vacuolar pH-homeostasis

B1 Model structures
B1.1 Core model (simple proton loss)

$$\frac{\mathrm{d}([\text{Hvac}] \cdot A_{\text{Vacuole}} \cdot)}{\mathrm{d}t} \quad = \quad + V_{\text{Vacuole}} \left(\text{factor}_{(\text{"V}-\text{ATPase"})} \cdot \frac{V_{(\text{"V}-\text{ATPase"})} \cdot [\text{Hcyt}]}{\text{Km}_{(\text{"V}-\text{ATPase"})} + [\text{Hcyt}]} \right)$$

$$- A_{\text{Vacuole}} \cdot \left(V_{(\text{Loss})} \cdot ([\text{Hvac}] - [\text{Hcyt}]) \right)$$

$$+ V_{\text{Vacuole}} \cdot \left(\left(\text{k1}_{(\text{Buffer1})} \cdot [\text{HA}] - \text{k2}_{(\text{Buffer1})} \cdot [\text{Hvac}] \cdot [\text{A}] \right) \right)$$

$$+ V_{\text{Vacuole}} \cdot \left(\left(\text{k1}_{(\text{Buffer2})} \cdot [\text{HB}] - \text{k2}_{(\text{Buffer2})} \cdot [\text{Hvac}] \cdot [\text{B}] \right) \right)$$

$$+ V_{\text{Vacuole}} \cdot \left(\left(\text{k1}_{(\text{Buffer3})} \cdot [\text{HC}] - \text{k2}_{(\text{Buffer3})} \cdot [\text{Hvac}] \cdot [\text{C}] \right) \right)$$

$$+ V_{\text{Vacuole}} \cdot \left(\left(\text{k1}_{(\text{Buffer4})} \cdot [\text{HD}] - \text{k2}_{(\text{Buffer4})} \cdot [\text{Hvac}] \cdot [\text{D}] \right) \right)$$

$$+ A_{\text{Vacuole}} \cdot \left(\text{factor}_{(\text{"V}-\text{PPase"})} \cdot \frac{V_{(\text{"V}-\text{PPase"})} \cdot [\text{Hcyt}]}{\text{Km}_{(\text{"V}-\text{PPase"})} + [\text{Hcyt}]} \right)$$

$$\frac{\mathrm{d}([\text{HA}] \cdot V_{\text{Vacuole}})}{\mathrm{d}t} \quad = \quad - V_{\text{Vacuole}} \cdot \left(\left(\text{k1}_{(\text{Buffer1})} \cdot [\text{HA}] - \text{k2}_{(\text{Buffer1})} \cdot [\text{Hvac}] \cdot [\text{A}] \right) \right)$$

$$\frac{\mathrm{d}([\text{A}] \cdot V_{\text{Vacuole}})}{\mathrm{d}t} \quad = \quad + V_{\text{Vacuole}} \cdot \left(\left(\text{k1}_{(\text{Buffer1})} \cdot [\text{HA}] - \text{k2}_{(\text{Buffer1})} \cdot [\text{Hvac}] \cdot [\text{A}] \right) \right)$$

$$\frac{\mathrm{d}([\mathrm{B}] \cdot V_{\mathrm{Vacuole}})}{\mathrm{d}t} \quad = \quad + V_{\mathrm{Vacuole}} \cdot \left(\left(\mathrm{k1}_{(\mathrm{Buffer2})} \cdot [\mathrm{HB}] - \mathrm{k2}_{(\mathrm{Buffer2})} \cdot [\mathrm{Hvac}] \cdot [\mathrm{B}] \right) \right)$$

$$\frac{\mathrm{d}([\mathrm{HB}] \cdot V_{\mathrm{Vacuole}})}{\mathrm{d}t} \quad = \quad - V_{\mathrm{Vacuole}} \cdot \left(\left(\mathrm{k1}_{(\mathrm{Buffer2})} \cdot [\mathrm{HB}] - \mathrm{k2}_{(\mathrm{Buffer2})} \cdot [\mathrm{Hvac}] \cdot [\mathrm{B}] \right) \right)$$

$$\frac{\mathrm{d}([\mathrm{C}] \cdot V_{\mathrm{Vacuole}})}{\mathrm{d}t} \quad = \quad + V_{\mathrm{Vacuole}} \cdot \left(\left(\mathrm{k1}_{(\mathrm{Buffer3})} \cdot [\mathrm{HC}] - \mathrm{k2}_{(\mathrm{Buffer3})} \cdot [\mathrm{Hvac}] \cdot [\mathrm{C}] \right) \right)$$

$$\frac{\mathrm{d}([\mathrm{HC}] \cdot V_{\mathrm{Vacuole}})}{\mathrm{d}t} \quad = \quad - V_{\mathrm{Vacuole}} \cdot \left(\left(\mathrm{k1}_{(\mathrm{Buffer3})} \cdot [\mathrm{HC}] - \mathrm{k2}_{(\mathrm{Buffer3})} \cdot [\mathrm{Hvac}] \cdot [\mathrm{C}] \right) \right)$$

$$\frac{\mathrm{d}([\mathrm{D}] \cdot V_{\mathrm{Vacuole}})}{\mathrm{d}t} \quad = \quad + V_{\mathrm{Vacuole}} \cdot \left(\left(\mathrm{k1}_{(\mathrm{Buffer4})} \cdot [\mathrm{HD}] - \mathrm{k2}_{(\mathrm{Buffer4})} \cdot [\mathrm{Hvac}] \cdot [\mathrm{D}] \right) \right)$$

$$\frac{\mathrm{d}([\mathrm{HD}] \cdot V_{\mathrm{Vacuole}})}{\mathrm{d}t} \quad = \quad - V_{\mathrm{Vacuole}} \cdot \left(\left(\mathrm{k1}_{(\mathrm{Buffer4})} \cdot [\mathrm{HD}] - \mathrm{k2}_{(\mathrm{Buffer4})} \cdot [\mathrm{Hvac}] \cdot [\mathrm{D}] \right) \right)$$

$$\mathrm{pHcyt} \quad = \quad - \left(\log_{10} \left(1e-6 \cdot [\mathrm{Hcyt}] \right) \right)$$

$$\mathrm{pHvac} \quad = \quad - \left(\log_{10} \left(1e-6 \cdot [\mathrm{Hvac}] \right) \right)$$

B1.2 Direct transport model

$$\frac{\mathrm{d}([\mathrm{Hvac}] \cdot V_{\mathrm{Vacuole}})}{\mathrm{d}t} = \quad + A_{\mathrm{Vacuole}} \cdot \left(\mathrm{factor}_{(\text{"V-ATPase"})} \cdot \frac{V_{(\text{"V-ATPase"})} \cdot [\mathrm{Hcyt}]}{\mathrm{Km}_{(\text{"V-ATPase"})} + [\mathrm{Hcyt}]} \right)$$

$$- A_{\mathrm{Vacuole}} \cdot \left(V_{(\mathrm{Loss})} \cdot ([\mathrm{Hvac}] - [\mathrm{Hcyt}]) \right)$$

$$+ V_{\mathrm{Vacuole}} \cdot \left(\left(\mathrm{k1}_{(\mathrm{Buffer1})} \cdot [\mathrm{HA}] - \mathrm{k2}_{(\mathrm{Buffer1})} \cdot [\mathrm{Hvac}] \cdot [\mathrm{A}] \right) \right)$$

$$+ V_{\mathrm{Vacuole}} \cdot \left(\left(\mathrm{k1}_{(\mathrm{Buffer2})} \cdot [\mathrm{HB}] - \mathrm{k2}_{(\mathrm{Buffer2})} \cdot [\mathrm{Hvac}] \cdot [\mathrm{B}] \right) \right)$$

$$+ V_{\mathrm{Vacuole}} \cdot \left(\left(\mathrm{k1}_{(\mathrm{Buffer3})} \cdot [\mathrm{HC}] - \mathrm{k2}_{(\mathrm{Buffer3})} \cdot [\mathrm{Hvac}] \cdot [\mathrm{C}] \right) \right)$$

$$+ V_{\mathrm{Vacuole}} \cdot \left(\left(\mathrm{k1}_{(\mathrm{Buffer4})} \cdot [\mathrm{HD}] - \mathrm{k2}_{(\mathrm{Buffer4})} \cdot [\mathrm{Hvac}] \cdot [\mathrm{D}] \right) \right)$$

$$+ A_{\mathrm{Vacuole}} \cdot \left(\mathrm{factor}_{(\text{"V-PPase"})} \cdot \frac{V_{(\text{"V-PPase"})} \cdot [\mathrm{Hcyt}]}{\mathrm{Km}_{(\text{"V-PPase"})} + [\mathrm{Hcyt}]} \right)$$

$$+ A_{\mathrm{Vacuole}} \cdot \left(\mathrm{factor}_{(\text{"unknown transport"})} \cdot \frac{V_{(\text{"unknown transport"})} \cdot [\mathrm{Hcyt}]}{\mathrm{Km}_{(\text{"unknown transport"})} + [\mathrm{Hcyt}]} \right)$$

$$\frac{\mathrm{d}([\mathrm{HA}] \cdot V_{\mathrm{Vacuole}})}{\mathrm{d}t} = \quad - V_{\mathrm{Vacuole}} \cdot \left(\left(\mathrm{k1}_{(\mathrm{Buffer1})} \cdot [\mathrm{HA}] - \mathrm{k2}_{(\mathrm{Buffer1})} \cdot [\mathrm{Hvac}] \cdot [\mathrm{A}] \right) \right)$$

$$\frac{\mathrm{d}([\mathrm{A}] \cdot V_{\mathrm{Vacuole}})}{\mathrm{d}t} = \quad + V_{\mathrm{Vacuole}} \cdot \left(\left(\mathrm{k1}_{(\mathrm{Buffer1})} \cdot [\mathrm{HA}] - \mathrm{k2}_{(\mathrm{Buffer1})} \cdot [\mathrm{Hvac}] \cdot [\mathrm{A}] \right) \right)$$

$$\frac{\mathrm{d}([\mathrm{B}] \cdot V_{\mathrm{Vacuole}})}{\mathrm{d}t} \quad = \quad + V_{\mathrm{Vacuole}} \cdot \left(\left(\mathrm{k1}_{(\mathrm{Buffer2})} \cdot [\mathrm{HB}] - \mathrm{k2}_{(\mathrm{Buffer2})} \cdot [\mathrm{Hvac}] \cdot [\mathrm{B}] \right) \right)$$

$$\frac{\mathrm{d}([\mathrm{HB}] \cdot V_{\mathrm{Vacuole}})}{\mathrm{d}t} \quad = \quad - V_{\mathrm{Vacuole}} \cdot \left(\left(\mathrm{k1}_{(\mathrm{Buffer2})} \cdot [\mathrm{HB}] - \mathrm{k2}_{(\mathrm{Buffer2})} \cdot [\mathrm{Hvac}] \cdot [\mathrm{B}] \right) \right)$$

$$\frac{\mathrm{d}([\mathrm{C}] \cdot V_{\mathrm{Vacuole}})}{\mathrm{d}t} \quad = \quad + V_{\mathrm{Vacuole}} \cdot \left(\left(\mathrm{k1}_{(\mathrm{Buffer3})} \cdot [\mathrm{HC}] - \mathrm{k2}_{(\mathrm{Buffer3})} \cdot [\mathrm{Hvac}] \cdot [\mathrm{C}] \right) \right)$$

$$\frac{\mathrm{d}([\mathrm{HC}] \cdot V_{\mathrm{Vacuole}})}{\mathrm{d}t} \quad = \quad - V_{\mathrm{Vacuole}} \cdot \left(\left(\mathrm{k1}_{(\mathrm{Buffer3})} \cdot [\mathrm{HC}] - \mathrm{k2}_{(\mathrm{Buffer3})} \cdot [\mathrm{Hvac}] \cdot [\mathrm{C}] \right) \right)$$

$$\frac{\mathrm{d}([\mathrm{D}] \cdot V_{\mathrm{Vacuole}})}{\mathrm{d}t} \quad = \quad + V_{\mathrm{Vacuole}} \cdot \left(\left(\mathrm{k1}_{(\mathrm{Buffer4})} \cdot [\mathrm{HD}] - \mathrm{k2}_{(\mathrm{Buffer4})} \cdot [\mathrm{Hvac}] \cdot [\mathrm{D}] \right) \right)$$

$$\frac{\mathrm{d}([\mathrm{HD}] \cdot V_{\mathrm{Vacuole}})}{\mathrm{d}t} \quad = \quad - V_{\mathrm{Vacuole}} \cdot \left(\left(\mathrm{k1}_{(\mathrm{Buffer4})} \cdot [\mathrm{HD}] - \mathrm{k2}_{(\mathrm{Buffer4})} \cdot [\mathrm{Hvac}] \cdot [\mathrm{D}] \right) \right)$$

$$\mathrm{pHcyt} \quad = \quad - \left(\log_{10} \left(1e - 6 \cdot [\mathrm{Hcyt}] \right) \right)$$

$$\mathrm{pHvac} \quad = \quad - \left(\log_{10} \left(1e - 6 \cdot [\mathrm{Hvac}] \right) \right)$$

B1.3 Protein degradation model

$$\frac{\mathrm{d}([\text{Hvac}] \cdot V_{\text{Vacuole}})}{\mathrm{d}t} \quad = \quad + A_{\text{Vacuole}} \cdot \left(\text{factor}_{(\text{"V}-\text{ATPase"})} \cdot \frac{V_{(\text{"V}-\text{ATPase"})} \cdot [\text{Hcyt}]}{\text{Km}_{(\text{"V}-\text{ATPase"})} + [\text{Hcyt}]} \right)$$

$$- A_{\text{Vacuole}} \cdot \left(V_{(\text{Loss})} \cdot ([\text{Hvac}] - [\text{Hcyt}]) \right)$$

$$+ V_{\text{Vacuole}} \cdot \left(\left(\text{k1}_{(\text{T2})} \cdot [\text{AminoHH}] - \text{k2}_{(\text{T2})} \cdot [\text{Amino\_H}] \cdot [\text{Hvac}] \right) \right)$$

$$+ V_{\text{Vacuole}} \cdot \left(\left(\text{k1}_{(\text{T3})} \cdot [\text{AminoHH}] - \text{k2}_{(\text{T3})} \cdot [\text{AminoH\_}] \cdot [\text{Hvac}] \right) \right)$$

$$+ V_{\text{Vacuole}} \cdot \left(\left(\text{k1}_{(\text{T4})} \cdot [\text{AminoH\_}] - \text{k2}_{(\text{T4})} \cdot [\text{Amino\_\_}] \cdot [\text{Hvac}] \right) \right)$$

$$+ A_{\text{Vacuole}} \cdot \left(\text{factor}_{(\text{"V}-\text{PPase"})} \cdot \frac{V_{(\text{"V}-\text{PPase"})} \cdot [\text{Hcyt}]}{\text{Km}_{(\text{"V}-\text{PPase"})} + [\text{Hcyt}]} \right)$$

$$+ V_{\text{Vacuole}} \cdot \left(\left(\text{k1}_{(\text{Buffer1})} \cdot [\text{HA}] - \text{k2}_{(\text{Buffer1})} \cdot [\text{Hvac}] \cdot [\text{A}] \right) \right)$$

$$+ V_{\text{Vacuole}} \cdot \left(\left(\text{k1}_{(\text{Buffer2})} \cdot [\text{HB}] - \text{k2}_{(\text{Buffer2})} \cdot [\text{Hvac}] \cdot [\text{B}] \right) \right)$$

$$+ V_{\text{Vacuole}} \cdot \left(\left(\text{k1}_{(\text{Buffer3})} \cdot [\text{HC}] - \text{k2}_{(\text{Buffer3})} \cdot [\text{Hvac}] \cdot [\text{C}] \right) \right)$$

$$+ V_{\text{Vacuole}} \cdot \left(\left(\text{k1}_{(\text{Buffer4})} \cdot [\text{HD}] - \text{k2}_{(\text{Buffer4})} \cdot [\text{Hvac}] \cdot [\text{D}] \right) \right)$$

$$+ V_{\text{Vacuole}} \cdot \left(\left(\text{k1}_{(\text{T1})} \cdot [\text{Amino\_H}] - \text{k2}_{(\text{T1})} \cdot [\text{Amino\_\_}] \cdot [\text{Hvac}] \right) \right)$$

$$\frac{\mathrm{d}([\mathrm{HA}] \cdot V_{\mathrm{Vacuole}})}{\mathrm{d}t} \quad = \quad -V_{\mathrm{Vacuole}} \cdot \left(\left(\mathrm{k1}_{(\mathrm{Buffer1})} \cdot [\mathrm{HA}] - \mathrm{k2}_{(\mathrm{Buffer1})} \cdot [\mathrm{Hvac}] \cdot [\mathrm{A}] \right) \right)$$

$$\frac{\mathrm{d}([\mathrm{A}] \cdot V_{\mathrm{Vacuole}})}{\mathrm{d}t} \quad = \quad +V_{\mathrm{Vacuole}} \cdot \left(\left(\mathrm{k1}_{(\mathrm{Buffer1})} \cdot [\mathrm{HA}] - \mathrm{k2}_{(\mathrm{Buffer1})} \cdot [\mathrm{Hvac}] \cdot [\mathrm{A}] \right) \right)$$

$$\frac{\mathrm{d}([\mathrm{B}] \cdot V_{\mathrm{Vacuole}})}{\mathrm{d}t} \quad = \quad +V_{\mathrm{Vacuole}} \cdot \left(\left(\mathrm{k1}_{(\mathrm{Buffer2})} \cdot [\mathrm{HB}] - \mathrm{k2}_{(\mathrm{Buffer2})} \cdot [\mathrm{Hvac}] \cdot [\mathrm{B}] \right) \right)$$

$$\frac{\mathrm{d}([\mathrm{HB}] \cdot V_{\mathrm{Vacuole}})}{\mathrm{d}t} \quad = \quad -V_{\mathrm{Vacuole}} \cdot \left(\left(\mathrm{k1}_{(\mathrm{Buffer2})} \cdot [\mathrm{HB}] - \mathrm{k2}_{(\mathrm{Buffer2})} \cdot [\mathrm{Hvac}] \cdot [\mathrm{B}] \right) \right)$$

$$\frac{\mathrm{d}([\mathrm{C}] \cdot V_{\mathrm{Vacuole}})}{\mathrm{d}t} \quad = \quad +V_{\mathrm{Vacuole}} \cdot \left(\left(\mathrm{k1}_{(\mathrm{Buffer3})} \cdot [\mathrm{HC}] - \mathrm{k2}_{(\mathrm{Buffer3})} \cdot [\mathrm{Hvac}] \cdot [\mathrm{C}] \right) \right)$$

$$\frac{\mathrm{d}([\mathrm{HC}] \cdot V_{\mathrm{Vacuole}})}{\mathrm{d}t} \quad = \quad -V_{\mathrm{Vacuole}} \cdot \left(\left(\mathrm{k1}_{(\mathrm{Buffer3})} \cdot [\mathrm{HC}] - \mathrm{k2}_{(\mathrm{Buffer3})} \cdot [\mathrm{Hvac}] \cdot [\mathrm{C}] \right) \right)$$

$$\frac{\mathrm{d}([\mathrm{D}] \cdot V_{\mathrm{Vacuole}})}{\mathrm{d}t} \quad = \quad +V_{\mathrm{Vacuole}} \cdot \left(\left(\mathrm{k1}_{(\mathrm{Buffer4})} \cdot [\mathrm{HD}] - \mathrm{k2}_{(\mathrm{Buffer4})} \cdot [\mathrm{Hvac}] \cdot [\mathrm{D}] \right) \right)$$

$$\frac{\mathrm{d}([\mathrm{HD}] \cdot V_{\mathrm{Vacuole}})}{\mathrm{d}t} \quad = \quad -V_{\mathrm{Vacuole}} \cdot \left(\left(\mathrm{k1}_{(\mathrm{Buffer4})} \cdot [\mathrm{HD}] - \mathrm{k2}_{(\mathrm{Buffer4})} \cdot [\mathrm{Hvac}] \cdot [\mathrm{D}] \right) \right)$$

$$\frac{\mathrm{d}([\mathrm{Amino\_\_}] \cdot V_{\mathrm{Vacuole}})}{\mathrm{d}t} \quad = \quad +V_{\mathrm{Vacuole}} \cdot \left(\left(\mathrm{k1}_{(\mathrm{T4})} \cdot [\mathrm{AminoH\_}] - \mathrm{k2}_{(\mathrm{T4})} \cdot [\mathrm{Amino\_\_}] \cdot [\mathrm{Hvac}] \right) \right)$$

$$-A_{\mathrm{Vacuole}} \cdot \left(\mathrm{k1}_{(\mathrm{Export2})} \cdot [\mathrm{Amino\_\_}] \right)$$

$$+V_{\mathrm{Vacuole}} \cdot \left(\left(\mathrm{k1}_{(\mathrm{T1})} \cdot [\mathrm{Amino\_H}] - \mathrm{k2}_{(\mathrm{T1})} \cdot [\mathrm{Amino\_\_}] \cdot [\mathrm{Hvac}] \right) \right)$$

$$\frac{\mathrm{d}([\text{Amino\_H}] \cdot V_{\text{Vacuole}})}{\mathrm{d}t} = + V_{\text{Vacuole}} \cdot \left(\text{k1}_{(\text{T2})} \cdot [\text{AminoHH}] - \text{k2}_{(\text{T2})} \cdot [\text{Amino\_H}] \cdot [\text{Hvac}] \right)$$

$$- A_{\text{Vacuole}} \cdot \left(\text{k1}_{(\text{Export1})} \cdot [\text{Amino\_H}] \right)$$

$$- V_{\text{Vacuole}} \cdot \left(\text{k1}_{(\text{T1})} \cdot [\text{Amino\_H}] - \text{k2}_{(\text{T1})} \cdot [\text{Amino\_\_}] \cdot [\text{Hvac}] \right)$$

$$\frac{\mathrm{d}([\text{AminoH\_}] \cdot V_{\text{Cytoplasm}})}{\mathrm{d}t} = + V_{\text{Vacuole}} \cdot \left(\left(\text{k1}_{(\text{T3})} \cdot [\text{AminoHH}] - \text{k2}_{(\text{T3})} \cdot [\text{AminoH\_}] \cdot [\text{Hvac}] \right) \right)$$

$$- V_{\text{Vacuole}} \cdot \left(\left(\text{k1}_{(\text{T4})} \cdot [\text{AminoH\_}] - \text{k2}_{(\text{T4})} \cdot [\text{Amino\_\_}] \cdot [\text{Hvac}] \right) \right)$$

$$- A_{\text{Vacuole}} \cdot \left(\text{k1}_{(\text{Export3})} \cdot [\text{AminoH\_}] \right)$$

$$+ A_{\text{Vacuole}} \cdot \left(v_{(\text{Import})} \right)$$

$$\frac{\mathrm{d}([\text{AminoHH}] \cdot V_{\text{Cytoplasm}})}{\mathrm{d}t} = - V_{\text{Vacuole}} \cdot \left(\left(\text{k1}_{(\text{T2})} \cdot [\text{AminoHH}] - \text{k2}_{(\text{T2})} \cdot [\text{Amino\_H}] \cdot [\text{Hvac}] \right) \right)$$

$$- V_{\text{Vacuole}} \cdot \left(\left(\text{k1}_{(\text{T3})} \cdot [\text{AminoHH}] - \text{k2}_{(\text{T3})} \cdot [\text{AminoH\_}] \cdot [\text{Hvac}] \right) \right)$$

$$- A_{\text{Vacuole}} \cdot \left(\text{k1}_{(\text{Export4})} \cdot [\text{AminoHH}] \right)$$

$$\text{pHcyt} = - \left(\log_{10} \left(1e - 6 \cdot [\text{Hcyt}] \right) \right)$$

$$\text{pHvac} = - \left(\log_{10} \left(1e - 6 \cdot [\text{Hvac}] \right) \right)$$

B1.4 Calcium antiport model

$$\frac{\mathrm{d}([\text{Hvac}] \cdot V_{\text{Vacuole}})}{\mathrm{d}t} =$$

$$A_{\text{Vacuole}} \cdot \left(\frac{\text{factor}_{("\text{V}-\text{ATPase}")} \cdot \text{Vmax}_{("\text{V}-\text{ATPase}")} \cdot [\text{Hcyt}]}{\text{Km}_{("\text{V}-\text{ATPase}")} + [\text{Hcyt}]} \right)$$

$$- A_{\text{Vacuole}} \cdot \left(- \text{factor}_{(\text{Loss})} \cdot g_{(\text{Loss})} \cdot \left(\text{Vm} - \frac{R \cdot T}{z_{(\text{Loss})} \cdot F} \cdot \ln\left(\frac{[\text{Hvac}]}{[\text{Hcyt}]} \right) \right) \right)$$
$$+ V_{\text{Vacuole}} \cdot \left(\left(\text{k1}_{(\text{HBuffer1})} \cdot [\text{HA}] - \text{k2}_{(\text{HBuffer1})} \cdot [\text{Hvac}] \cdot [\text{A}] \right) \right)$$
$$+ V_{\text{Vacuole}} \cdot \left(\left(\text{k1}_{(\text{HBuffer2})} \cdot [\text{HB}] - \text{k2}_{(\text{HBuffer2})} \cdot [\text{Hvac}] \cdot [\text{B}] \right) \right)$$
$$+ V_{\text{Vacuole}} \cdot \left(\left(\text{k1}_{(\text{HBuffer3})} \cdot [\text{HC}] - \text{k2}_{(\text{HBuffer3})} \cdot [\text{Hvac}] \cdot [\text{C}] \right) \right)$$
$$+ V_{\text{Vacuole}} \cdot \left(\left(\text{k1}_{(\text{HBuffer4})} \cdot [\text{HD}] - \text{k2}_{(\text{HBuffer4})} \cdot [\text{Hvac}] \cdot [\text{D}] \right) \right)$$
$$- A_{\text{Vacuole}} \cdot 3 \cdot \left(- [\text{vesicles}] \cdot \text{factor}_{(\text{CAX})} \cdot g_{(\text{CAX})} \cdot \left(\text{Vm} - \frac{R \cdot T}{z_{(\text{CAX})} \cdot F} \cdot \ln\left(\frac{[\text{Hvac}]^3 \cdot [\text{Cacyt}]}{[\text{Hcyt}]^3 \cdot [\text{Cavac}]} \right) \right) \right)$$
$$+ A_{\text{Vacuole}} \cdot \left(\frac{\text{factor}_{("\text{V}-\text{PPase}")} \cdot \text{Vmax}_{("\text{V}-\text{PPase}")} \cdot [\text{Hcyt}]}{\text{Km}_{("\text{V}-\text{PPase}")} + [\text{Hcyt}]} \right)$$

$$\frac{\mathrm{d}([\text{HA}] \cdot V_{\text{Vacuole}})}{\mathrm{d}t} =$$

$$- V_{\text{Vacuole}} \cdot \left(\left(\text{k1}_{(\text{HBuffer1})} \cdot [\text{HA}] - \text{k2}_{(\text{HBuffer1})} \cdot [\text{Hvac}] \cdot [\text{A}] \right) \right)$$

$$\frac{\mathrm{d}([\text{A}] \cdot V_{\text{Vacuole}})}{\mathrm{d}t} =$$

$$+ V_{\text{Vacuole}} \cdot \left(\left(\text{k1}_{(\text{HBuffer1})} \cdot [\text{HA}] - \text{k2}_{(\text{HBuffer1})} \cdot [\text{Hvac}] \cdot [\text{A}] \right) \right)$$

$$\frac{\mathrm{d}([\mathrm{B}] \cdot V_{\mathrm{Vacuole}})}{\mathrm{d}t} =$$

$$+ V_{\mathrm{Vacuole}} \cdot \left(\left(\mathrm{k1}_{(\mathrm{HBuffer2})} \cdot [\mathrm{HB}] - \mathrm{k2}_{(\mathrm{HBuffer2})} \cdot [\mathrm{Hvac}] \cdot [\mathrm{B}] \right) \right)$$

$$\frac{\mathrm{d}([\mathrm{HB}] \cdot V_{\mathrm{Vacuole}})}{\mathrm{d}t} =$$

$$- V_{\mathrm{Vacuole}} \cdot \left(\left(\mathrm{k1}_{(\mathrm{HBuffer2})} \cdot [\mathrm{HB}] - \mathrm{k2}_{(\mathrm{HBuffer2})} \cdot [\mathrm{Hvac}] \cdot [\mathrm{B}] \right) \right)$$

$$\frac{\mathrm{d}([\mathrm{C}] \cdot V_{\mathrm{Vacuole}})}{\mathrm{d}t} =$$

$$+ V_{\mathrm{Vacuole}} \cdot \left(\left(\mathrm{k1}_{(\mathrm{HBuffer3})} \cdot [\mathrm{HC}] - \mathrm{k2}_{(\mathrm{HBuffer3})} \cdot [\mathrm{Hvac}] \cdot [\mathrm{C}] \right) \right)$$

$$\frac{\mathrm{d}([\mathrm{HC}] \cdot V_{\mathrm{Vacuole}})}{\mathrm{d}t} =$$

$$- V_{\mathrm{Vacuole}} \cdot \left(\left(\mathrm{k1}_{(\mathrm{HBuffer3})} \cdot [\mathrm{HC}] - \mathrm{k2}_{(\mathrm{HBuffer3})} \cdot [\mathrm{Hvac}] \cdot [\mathrm{C}] \right) \right)$$

$$\frac{\mathrm{d}([\mathrm{D}] \cdot V_{\mathrm{Vacuole}})}{\mathrm{d}t} =$$

$$+ V_{\mathrm{Vacuole}} \cdot \left(\left(\mathrm{k1}_{(\mathrm{HBuffer4})} \cdot [\mathrm{HD}] - \mathrm{k2}_{(\mathrm{HBuffer4})} \cdot [\mathrm{Hvac}] \cdot [\mathrm{D}] \right) \right)$$

$$\frac{\mathrm{d}([\mathrm{HD}] \cdot V_{\mathrm{Vacuole}})}{\mathrm{d}t} =$$

$$- V_{\mathrm{Vacuole}} \cdot \left(\left(\mathrm{k1}_{(\mathrm{HBuffer4})} \cdot [\mathrm{HD}] - \mathrm{k2}_{(\mathrm{HBuffer4})} \cdot [\mathrm{Hvac}] \cdot [\mathrm{D}] \right) \right)$$

$$\frac{\mathrm{d}([\text{Cacyt}] \cdot V_{\text{Cytoplasm}})}{\mathrm{d}t} =$$

$$-V_{\text{Cytoplasm}} \cdot \mathrm{k1}_{(\text{CaBufferingcyt})} \cdot [\text{Cacyt}] \cdot [\text{CalciumBuffercyt}]$$
$$-\mathrm{k2}_{(\text{CaBufferingcyt})} \cdot [\text{"Ca} - \text{CalciumBuffercyt"}]$$
$$- A_{\text{Vacuole}} \cdot \left(\frac{V_{(\text{"Ca}-\text{Pump"})} \cdot [\text{Cacyt}]}{\mathrm{Km}_{(\text{"Ca}-\text{Pump"})} + [\text{Cacyt}]} \right)$$
$$- A_{\text{Vacuole}} \cdot \left(- [\text{vesicles}] \cdot \text{factor}_{(\text{CAX})} \cdot g_{(\text{CAX})} \cdot \left(\mathrm{Vm} - \frac{R \cdot T}{z_{(\text{CAX})} \cdot F} \cdot \ln\left(\frac{[\text{Hvac}]^3 \cdot [\text{Cacyt}]}{[\text{Hcyt}]^3 \cdot [\text{Cavac}]} \right) \right) \right)$$
$$+ \left(- A_{\text{Vacuole}} \cdot \text{factor}_{(\text{"Ca}-\text{Channel"})} \cdot \frac{g_{(\text{"Ca}-\text{Channel"})}}{1 + e^{\frac{x_{(\text{"Ca}-\text{Channel"})} \cdot z_{(\text{"Ca}-\text{Channel"})} \cdot F}{R \cdot T} \cdot \left(\mathrm{Vm} - \mathrm{Vh}_{(\text{"Ca}-\text{Channel"})} \right)}} \right.$$
$$\left. \cdot A_{\text{Vacuole}} \cdot \left(\mathrm{Vm} - \frac{R \cdot T}{z_{(\text{"Ca}-\text{Channel"})} \cdot F} \cdot \ln\left(\frac{[\text{Cavac}]}{[\text{Cacyt}]} \right) \right) \right)$$

$$\frac{\mathrm{d}([\text{Cavac}] \cdot V_{\text{Vacuole}})}{\mathrm{d}t} =$$

$$-V_{\text{Vacuole}} \cdot \left(\mathrm{k1}_{(\text{CaBufferingvac})} \cdot [\text{Cavac}] \cdot [\text{CalciumBuffervac}] \right.$$
$$-\mathrm{k2}_{(\text{CaBufferingvac})} \cdot [\text{"Ca} - \text{CalciumBuffervac"}])$$
$$+ A_{\text{Vacuole}} \cdot \left(\frac{V_{(\text{"Ca}-\text{Pump"})} \cdot [\text{Cacyt}]}{\mathrm{Km}_{(\text{"Ca}-\text{Pump"})} + [\text{Cacyt}]} \right)$$
$$+ A_{\text{Vacuole}} \cdot \left(- [\text{vesicles}] \cdot \text{factor}_{(\text{CAX})} \cdot g_{(\text{CAX})} \cdot \left(\mathrm{Vm} - \frac{R \cdot T}{z_{(\text{CAX})} \cdot F} \cdot \ln\left(\frac{[\text{Hvac}]^3 \cdot [\text{Cacyt}]}{[\text{Hcyt}]^3 \cdot [\text{Cavac}]} \right) \right) \right)$$
$$- A_{\text{Vacuole}} \cdot \left(- \text{factor}_{(\text{"Ca}-\text{Channel"})} \cdot \frac{g_{(\text{"Ca}-\text{Channel"})}}{1 + e^{\frac{x_{(\text{"Ca}-\text{Channel"})} \cdot z_{(\text{"Ca}-\text{Channel"})} \cdot F}{R \cdot T} \cdot (\mathrm{Vm} - \mathrm{Vh}_{(\text{"Ca}-\text{Channel"})})}} \right.$$
$$\left. \cdot (\mathrm{Vm} - \frac{R \cdot T}{z_{(\text{"Ca}-\text{Channel"})} \cdot F} \cdot \ln\left(\frac{[\text{Cavac}]}{[\text{Cacyt}]} \right))) \right.$$

$$\frac{\mathrm{d}([\text{vesicles}] \cdot V_{\text{Cytoplasm}})}{\mathrm{d}t} =$$

$$- V_{\text{Cytoplasm}} \cdot \left(\mathrm{k1}_{(\text{"vesicles} ->")} \cdot [\text{vesicles}] \right)$$

$$\frac{\mathrm{d}([\text{CalciumBuffercyt}] \cdot V_{\text{Cytoplasm}})}{\mathrm{d}t} =$$

$$- V_{\text{Cytoplasm}} \cdot ((\text{k1}_{(\text{CaBufferingcyt})} \cdot [\text{Cacyt}] \cdot [\text{CalciumBuffercyt}]$$
$$- \text{k2}_{(\text{CaBufferingcyt})} \cdot [\text{"Ca} - \text{CalciumBuffercyt"}]))$$

$$\frac{\mathrm{d}([\text{CalciumBuffervac}] \cdot V_{\text{Vacuole}})}{\mathrm{d}t} =$$

$$- V_{\text{Vacuole}} \cdot ((\text{k1}_{(\text{CaBufferingvac})} \cdot [\text{Cavac}] \cdot [\text{CalciumBuffervac}]$$
$$- \text{k2}_{(\text{CaBufferingvac})} \cdot [\text{"Ca} - \text{CalciumBuffervac"}]))$$

$$\frac{\mathrm{d}([\text{"Ca} - \text{CalciumBuffercyt"}] \cdot V_{\text{Cytoplasm}})}{\mathrm{d}t} =$$

$$+ V_{\text{Cytoplasm}} \cdot ((\text{k1}_{(\text{CaBufferingcyt})} \cdot [\text{Cacyt}] \cdot [\text{CalciumBuffercyt}]$$
$$- \text{k2}_{(\text{CaBufferingcyt})} \cdot [\text{"Ca} - \text{CalciumBuffercyt"}]))$$

$$\frac{\mathrm{d}([\text{"Ca} - \text{CalciumBuffervac"}] \cdot V_{\text{Vacuole}})}{\mathrm{d}t} =$$

$$+ V_{\text{Vacuole}} \cdot ((\text{k1}_{(\text{CaBufferingvac})} \cdot [\text{Cavac}] \cdot [\text{CalciumBuffervac}]$$
$$- \text{k2}_{(\text{CaBufferingvac})} \cdot [\text{"Ca} - \text{CalciumBuffervac"}]))$$

$$\text{pHcyt} = - \left(\log_{10}([\text{Hcyt}]) \right)$$

$$\text{pHvac} = - \left(\log_{10}([\text{Hvac}]) \right)$$

$$\text{Vm} = \frac{-0.035 \cdot ([\text{Hvac}] - [\text{Hcyt}])}{1.585e-6 - 6.3e-8}$$

B2 Membrane potential dependend processes

B2.1 Channel opening probability

The two-state Boltzmann equation

$$C_{\mathrm{o}} = \frac{1}{e^{x*\frac{zF}{R*T}*(Vm-Vh)}}$$

describes the fraction of C_{o} of open channels. This can be understood by looking at the transition between open (O) and closed (C) state of a channel:

$$O \longleftrightarrow C$$

with which we can formulate

$$\frac{dO}{dt} = k_1 * O - k_{-1} * C$$

which solves in steady state to

$$O = \frac{k_{-1}}{k_{-1} + k_1}$$

Voltage dependency can be taken into the kinetic constant as done in [157]:

$$k_1 = k_1{}^0 * e^{\Delta G*\frac{1}{RT}+zF*x_1*Vm}$$

and

$$k_{-1} = k_{-1}{}^0 * e^{\Delta G*\frac{1}{RT}+zF*x_{-1}*Vm}$$

with x_1, x_{-1} being the fractional distance of the reaction energy barrier from inside and outside the membrane.

By combining the above equations and replacing x_1 - x_{-1} with x, one arrives at the above stated two-state Boltzmann equation.